UNIVERSITY OF CALIFORNIA SAN DIEGO

# Soft Robots for Operation on Unknown Surfaces in Extreme Environments

A dissertation submitted in partial satisfaction of the
requirements for the degree
Doctor of Philosophy

in

Engineering Sciences (Mechanical Engineering)

by

Paul E. Glick

Committee in charge:

Professor Michael T. Tolley, Chair
Professor Maurício de Oliveira
Professor Nick Gravish
Professor Kenneth J. Loh
Professor Tania Morimoto

2021

Copyright
Paul E. Glick, 2021
All rights reserved.

The dissertation of Paul E. Glick is approved, and it is acceptable in quality and form for publication on microfilm and electronically.

University of California San Diego

2021

EPIGRAPH

*All models are wrong, but some are useful.*

—George E. P. Box

*Ruff ruff ruff, ruff-ruff woof.*

—Spot T.

TABLE OF CONTENTS

Dissertation Approval Page . . . iii

Epigraph . . . iv

Table of Contents . . . v

List of Figures . . . vii

List of Tables . . . ix

Acknowledgements . . . x

Vita . . . xii

Abstract of the Dissertation . . . xiii

Chapter 1 Introduction . . . 1
1.1 Motivation . . . 1
1.2 Outline of the Thesis . . . 4

Chapter 2 Adhesives for Underactuated Linkages . . . 6
2.1 A soft robotic gripper with gecko inspired adhesive . . . 6
2.1.1 Background . . . 8
2.1.2 Design and Manufacturing . . . 10
2.1.3 Results . . . 16
2.2 Robust capture of unknown objects with a highly under-actuated gripper 24
2.2.1 Design Principles . . . 27
2.2.2 Mechanical Design . . . 32
2.2.3 Results . . . 35
2.2.4 Discussion . . . 41
2.3 Acknowledgements . . . 43

Chapter 3 Growth as a Method to Navigate Unexplored Passageways . . . 45
3.1 Eversion and retraction of a soft robot towards the exploration of coral reefs . . . 45
3.1.1 Design and Fabrication of the Underwater Eversion Robot . 48
3.1.2 Modeling the Eversion Robot . . . 53
3.1.3 Results . . . 57
3.2 Branching Vine Robots for Unmapped Environments . . . 60
3.2.1 Materials and Methods . . . 65
3.2.2 Optimization and Hardware Results . . . 72
3.2.3 Supporting Details . . . 77

3.3 Acknowledgements . . . . . 81

Chapter 4 Varying the Complexity of Object Interactions in Soft Gripping . . . . . 87
4.1 Long-Duration Surface Anchoring With a Hybrid Electrostatic and Gecko-Inspired Adhesive . . . . . 87
4.1.1 Design of the Electrostatic Anchor . . . . . 90
4.1.2 Manufacturing . . . . . 96
4.1.3 Electrostatic Anchor Results . . . . . 98
4.2 High Strength Inflatable Pouch Anchors . . . . . 102
4.2.1 Design Principles . . . . . 105
4.2.2 Fabrication . . . . . 108
4.2.3 Pouch Anchor Performance . . . . . 110
4.3 A low-power, jamming, magnetorheological valve using electropermanent magnets for distributed control in soft robots . . . . . 116
4.3.1 Design of a Magnetorheological Valve . . . . . 119
4.3.2 Demonstration in a Soft Robot . . . . . 123
4.4 Acknowledgements . . . . . 124

Chapter 5 Conclusions . . . . . 126

Bibliography . . . . . 128

LIST OF FIGURES


Figure 1.1: Robotic surrogates enhance exploration of extreme environments . . . . . 2
Figure 1.2: NASA's proposed missions to Europa demonstrate the challenge of sending robots to extreme environments especially when information is limited . . 3

Figure 2.1: Gecko elastomer actuator grippers can achieve versatile grasps on complex shapes . . . . . 7
Figure 2.2: Active fingers allow for grasps on objects that do not typically support gecko-inspired adhesives . . . . . 10
Figure 2.3: Model of a fluidic elastomer actuator as a series of discrete joints . . . . . 13
Figure 2.4: Multi-step manufacturing process of pneumatic soft gripper with gecko-inspired adhesive . . . . . 15
Figure 2.5: Experimental setup to validate the torque generated by a single elastomer actuator joint . . . . . 16
Figure 2.6: Torque generated by an elastomer joint . . . . . 18
Figure 2.7: Cylindrical FTIR sensor used to measure contact area . . . . . 19
Figure 2.8: Images captured on FTIR sensor showing torque behavior of the optimized gripper . . . . . 20
Figure 2.9: Gecko elastomer actuator grippers provide a stronger grasp across a wide range of cylinders . . . . . 21
Figure 2.10: Evaluation of chamber pressure for gecko/non-gecko elastomer actuator grip strength . . . . . 22
Figure 2.11: Three actuators create a wrapped grasp, engaging the gecko-inspired adhesives and supporting an 11.3 kg (25 lb) mass at 40 kPa of pressure . . . . . 23
Figure 2.12: Elastomer actuator grippers with gecko-inspired adhesives are capable of a wide range of stable grasps . . . . . 24
Figure 2.13: Highly under-actuated mechanisms exhibit several unique properties that are well suited to grasping large and irregular objects . . . . . 25
Figure 2.14: A free body diagram of each joint . . . . . 28
Figure 2.15: A CAD rendering of a highly under-actuated gripper with two opposing linkages. . . . . 32
Figure 2.16: Linkage mechanism . . . . . 33
Figure 2.17: Plot of pulley sizes and modeled torque at different grip tensions . . . . . 35
Figure 2.18: Tension required to actuate each link in the gripper on a flat surface . . . . 36
Figure 2.19: Gripper modeling and behavior on a flat surface . . . . . 38
Figure 2.20: Force distribution into the surface of different objects . . . . . 39
Figure 2.21: Maximum grasp strength on different surfaces . . . . . 40
Figure 2.22: Demonstrations of unique capabilities . . . . . 42

Figure 3.1: The natural crevices and passageways of the diverse coral reef structure . . 46
Figure 3.2: The robot can evert through varied passageways . . . . . 48
Figure 3.3: Exploded 3D model of the robot system . . . . . 49

Figure 3.4: Payload mechanism for the eversion robot . . . . . 51
Figure 3.5: The pressure differentials between each chamber . . . . . 53
Figure 3.6: Free body diagram of the eversion robot . . . . . 55
Figure 3.7: Experimental setup for measuring maximum loads of the everted soft body 58
Figure 3.8: Radial loading of the everted soft body . . . . . 59
Figure 3.9: Demonstration of eversion underwater . . . . . 60
Figure 3.10: Branching vine robots for navigating unexplored spaces . . . . . 64
Figure 3.11: Optimization process through simulation . . . . . 67
Figure 3.12: Evaluating the impact of diversity in the training data . . . . . 82
Figure 3.13: Comparison of the reachability of the space . . . . . 83
Figure 3.14: Demonstration of fabrication and deployment of an optimized design . . . 84
Figure 3.15: Optimization and hardware validation of anchoring . . . . . 85
Figure 3.16: Comparison of the results with the two different optimization approaches . 85
Figure 3.17: TPU testing . . . . . 86
Figure 3.18: Repeatability of anchoring . . . . . 86

Figure 4.1: Two sizes of electrostatic anchors . . . . . 88
Figure 4.2: Free body diagram of the anchor . . . . . 91
Figure 4.3: Switching circuit that enables power saving . . . . . 94
Figure 4.4: The circuit diagram for the switching circuit . . . . . 96
Figure 4.5: Primary phases of the fabrication process . . . . . 97
Figure 4.6: Impact of the center of mass on the anchor . . . . . 100
Figure 4.7: Impact of switching on adhesive force . . . . . 102
Figure 4.8: An inflatable anchor that is light weight and easily positioned . . . . . 103
Figure 4.9: Schematic of the pouch anchor . . . . . 106
Figure 4.10: Fabrication process for an inflatable pouch anchor . . . . . 108
Figure 4.11: Fabrication of the microspine arrays . . . . . 109
Figure 4.12: Non-dimensional experimental model for area in contact between the anchor and surface $A_C$ as a function of channel width . . . . . 110
Figure 4.13: Maximum load capacity of the anchor as a function of internal pressure . . 111
Figure 4.14: The width of a channel determines the area in contact and therefore the normal force the anchor exerts outwards . . . . . 112
Figure 4.15: Maximum force held by anchor as a function of channel angle . . . . . 112
Figure 4.16: Anchoring force on different materials . . . . . 113
Figure 4.17: Field demonstrations for the pouch anchor . . . . . 115
Figure 4.18: A small, low-power, magnetorheological valve . . . . . 117
Figure 4.19: Constriction behavior for the valve . . . . . 120
Figure 4.20: The behavior of an electropermanent magnet . . . . . 122
Figure 4.21: A demonstration using MRF to drive a 2 segment, 4 actuator soft robotic appendage . . . . . 124

LIST OF TABLES

Table 2.1: Comparison of recent high-load fluidic elastomer actuators . . . . . 22

Table 4.1: Adhesion in the normal direction with no shear load applied to the electrostatic anchor . . . . . 99

Table 4.2: Power savings due to switching circuit . . . . . 101

ACKNOWLEDGEMENTS

First and foremost, I'd like to thank my family, friends, and colleagues who have supported me throughout this journey. I have been so fortunate to be surrounded by loving, fun, intelligent, and creative humans (and dogs) who have helped me become who I am today. Mom, Dad, & Em, your unwavering love gave me the confidence to pursue my dreams. Gabbie & Spottie, you each joined this team part way through graduate school. I'm eternally grateful that this path led me to each of you and to many good things. Thanks to all of my friends, so many of my favorite memories come from this last decade of silliness. I especially appreciate the multi-purpose room, widely regarded as 2nd best recreation center in North Clairemont. Also Michael, seeing you graduate from a questionable for-profit university and still find a great job taught me that anything is possible with hard work.

To my labmates from UCSD and JPL, you have been helpful, fun, and inspring. Ms. Groppe & Mr. Raneses, with the pairing of physics and power-tools you showed me how creative engineering can be. Thank you Prof. Bitmead, Jeff, & Dr. Volpe for supporting me early on and helping me find internships. Thank you to Prof. Lyons and Davidson, your support of the science policy fellowship has helped me think more broadly and creatively. Jess, sailing aboard the Nautilus has been one of the highlights of my PhD, thank you for introducing me to the world of ocean exploration. Thank you Josh, Gregg, Bob, and Nicole for your support, training, and for giving me the opportunity to sail with you all. Tania, Mauricio, Nick, and Ken, thank you all so much for your guidance and help. Don, Aaron, Mike - thank you for your incredible mentorship. Working with you has been a privilege and has changed the way I approach research & engineering.

I gratefully acknowledge NASA & The NSTRF (now NSTGRO) program who made this research possible. Furthermore, thank you to the UCSD FISP program and the GPS Science Policy Fellowship for your support.

Chapter 2, in part, is a reprint of the material as it appears in IEEE Robotics and Automa-

tion Letters 2018. Glick, Paul E.; Suresh, Srinivasan A.; Ruffatto III, Donald; Cutkosky, Mark; Tolley, Michael T.; Parness, Aaron. The dissertation author was the primary investigator and author of this paper.

Chapter 2, in part, is a reprint of the material abbreviated from IEEE International Conference on Robotics and Automation 2020. Glick, Paul E.; Van Crey, Nikko; Tolley, Michael T.; Ruffatto III, Donald. The dissertation author was the co-primary investigator and author of this paper.

Chapter 3, in part, is a reprint of the material as it appears in IEEE International Conference on Soft Robotics 2019. Luong, Jamie; Glick, Paul E.; Ong, Aaron; deVries, Maya S.; Sandin, Stuart; Hawkes, Elliot W.; Tolley, Michael T. The dissertation author was the co-primary investigator and author of this paper.

Chapter 3, in part, is currently being prepared for submission for publication of the material. Glick, Paul E.; Adibnazari, Iman; Drotman, Dylan; Ruffatto III, Donald; Tolley, Michael T. The dissertation author was the primary investigator and author of this paper.

Chapter 4, in part, is a reprint of material abbreviated from IEEE Robotics and Automation Letters 2020. Glick, Paul E.; Drotman, Dylan; Ruffatto III, Donald; Tolley, Michael T. The dissertation author was the primary investigator and author of this paper.

Chapter 4, in part, is a reprint of material abbreviated from IEEE Robotics and Automation Letters 2018. Ruffatto III, Donald; Glick, Paul E.; Tolley, Michael T.; Parness, Aaron. The dissertation author contributed to this paper.

Chapter 4, in part, is a reprint of material abbreviated from Smart Materials and Structures 2020. Leps, Thomas; Glick, Paul E.; Ruffatto III, Donald; Parness, Aaron; Tolley, Michael T.; Hartzell, Christine. The dissertation author was the co-primary investigator and author of this paper.

## VITA

| | |
|---|---|
| 2010-2014 | B. S. in Engineering Sciences (Mechanical Engineering) *cum laude*, University of California San Diego |
| 2015-2016 | Graduate Teaching Assistant, University of California San Diego |
| 2016-2021 | Graduate Research Fellow, University of California San Diego |
| 2018 | M. S. in Engineering Sciences (Mechanical Engineering), University of California San Diego |
| 2021 | Ph. D. in Engineering Sciences (Mechanical Engineering), University of California San Diego |

## PUBLICATIONS


T. Leps, P.E. Glick, D. Ruffatto III, A Parness, M.T. Tolley, C Hartzell, "A low-power, jamming, magnetorheological valve using elecropermanent magnets suitable for distributed control in soft robots", *Smart Materials and Structures*, 29 (10), 2020.

A.F. Minori, Q. He, P.E. Glick, I. Adibnazari, A. Stopol, S. Cai, M.T. Tolley, "Reversible actuation for self-folding modular machines using liquid crystal elastomer", *Smart Materials and Structures*, 29 (10) , 2020.

P.E. Glick, N. Van Crey, M.T. Tolley, D. Ruffatto III, "Robust capture of unkown objects with a highly under-actuated gripper", *IEEE Int'l Conf. on Robotics and Automation*, pp. 3996-4002, 2020.

P.E. Glick, D. Drotman, D. Ruffatto III, M.T. Tolley, "High strength inflatable pouch anchors", *IEEE Robotics and Automation Letters*, 5 (3), 2020.

J. Luong, P.E. Glick, A. Ong, M.S. deVries, S. Sandin, E.W. Hawkes, M.T. Tolley, "Eversion and retraction of a soft robot towards the exploration of coral reefs", *IEEE Int'l Conf. on Soft Robotics*, pp. 801-807, 2019.

D. Ruffatto, P.E. Glick, M.T. Tolley, A. Parness "Long-duration surface anchoring with a hybrid electrostatic and gecko-inspired adhesive", *IEEE Robotics and Automation Letters*, 3 (4), 2018.

P.E. Glick, S.A. Suresh, D. Ruffatto, M. Cutkosky, M.T. Tolley, A. Parness, "A soft robotic gripper with gecko-inspired adhesive", *IEEE Robotics and Automation Letters*, 3 (2), 2018.

E.W. Schaler, D. Ruffatto III, P.E. Glick, V. White, A. Parness, "An electrostatic gripper for flexible objects", *IEEE/RSJ Int'l Conf. on Intelligent Robots and Systems*, pp. 1172-1179, 2017.

J.M. Friesen, P.E. Glick, M. Fanton, P. Manovi, A. Xydes, T. Bewley, V. Sunspiral, "The second generation prototype of a duct climbing tensegrity robot, DuCTTv2", *IEEE Int'l Conf. on Robotics and Automation*, pp. 2123-2128, 2016.

ABSTRACT OF THE DISSERTATION

**Soft Robots for Operation on Unknown Surfaces in Extreme Environments**

by

Paul E. Glick

Doctor of Philosophy in Engineering Sciences (Mechanical Engineering)

University of California San Diego, 2021

Professor Michael T. Tolley, Chair

The field of soft robotics, through the use of intrinsic compliance and embodied intelligence, promises to extend robotic applications beyond factory floors and industrial automation. However, this added compliance can result in a loss in strength or mechanical performance. This thesis investigates using the compliance and adaptability of soft robots for extreme environments, without a reduction in strength. Extreme environments in particular reward embodied intelligence since protecting the sensors, actuators, batteries, and computers required for traditional control is challenging. This topic is addressed through two main tasks: the use of under-actuated grippers employing controllable adhesives and growing vine robots that leverage their surrounding environment for reinforcement. The grippers employ adhesives to distribute shear forces along the

length of arbitrarily-shaped objects, relying on the soft under-actuated linkage to ensure good surface contact. Similarly, the growing vine robots can harness the surrounding environments to conform to preexisting pathways and help support payloads. Ultimately this work shows a pathway to simplifying robotic control without sacrificing performance by creating designs that work with rather than against these unpredictable and challenging environments.

# Chapter 1

# Introduction

## 1.1 Motivation

The act of exploration is integral to human nature. Similarly, technological progress is integral to pushing exploration into new frontiers. As the transition from compasses to global positioning satellites shows, the process of exploration both drives and adopts technological innovation. These tools of exploration have now crossed a crucial threshold: no longer are the tools of exploration passive and simply intended to help the human explorer, now the tools are the explorers. Robot agents may now serve as explorers, either directly teleoperated by humans or with enough autonomy to operate with minimal supervision. Indeed, the limits on exploration are now more often broken in research labs than on mountain peaks. This change has important implications, since exploration traditionally involved risk to the humans involved. Through the use of robotics, researchers may now safely access regions of scientific interest that are even more remote or dangerous than ever before.

Though these robotic surrogates do not need to sleep, eat, or return home the way human explorers must, these robots must still function in their respective environments long enough to accomplish their intended task. In environments with extreme pressure, radiation, temperature,

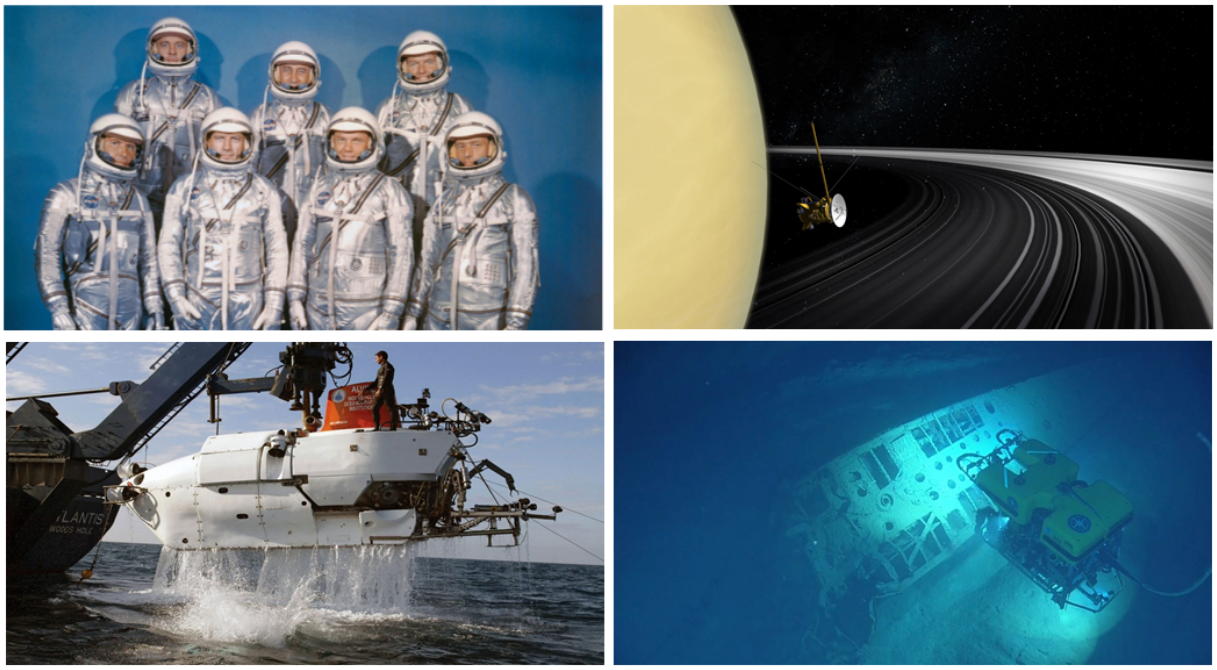


**Figure 1.1**: Robotic surrogates enhance exploration of extreme environments. The Mercury 7 astronauts, the first American explorers to enter space (Top Left, *NASA*). Artists rendering of NASA's Cassini robotic spacecraft on a one-way mission to the outer reaches of the solar system (Top Right, *NASA*). Recovery of the human-piloted deep submergence vehicle (DSV) Alvin (Bottom Left, *Woods Hole Oceanographic Institution*). The ROV Hercules piloted from the E/V Nautilus can reach similar depths, take samples, and spend more time on the seafloor compared to human-operated DSV's (Bottom Right, *Ocean Exploration Trust*).

or chemical properties, this can be a challenge. In particular, each sensor, actuator, computer, communication device, and power source must be adequately shielded from the harsh conditions. With increasingly complex operational objectives for these robots, providing enough dexterity and intelligence in an environmentally shielded robotic system becomes challenging. This challenge is compounded when uncertainty about the environment or task is high. This uncertainty effects robot design since the robots must be able to accommodate a wider range of situations and loads. Furthermore, the robots must contain sufficient sensing and intelligence to adapt to the particular situation.

An example of the importance of this uncertainty in extreme environments may be seen through NASA's proposed missions to the moon Europa. Europa is a high priority destination

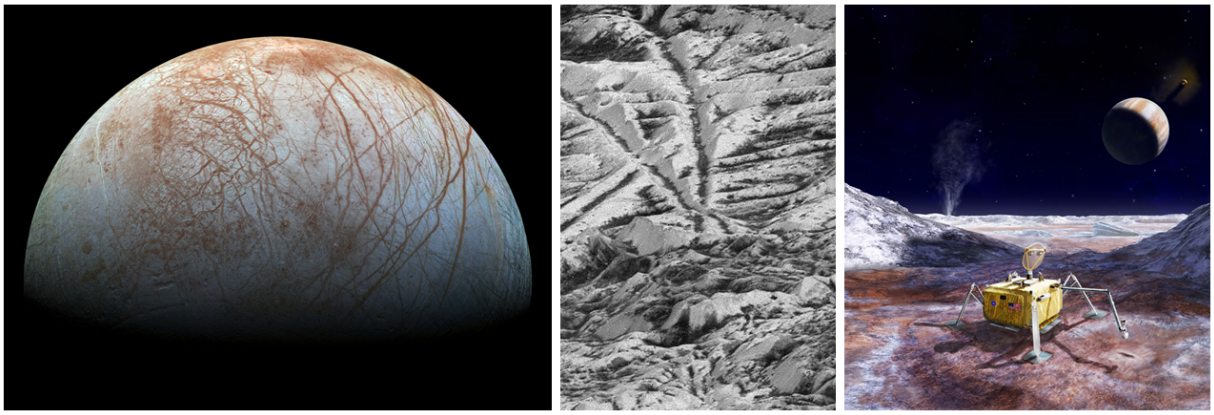


**Figure 1.2**: NASA's proposed missions to Europa demonstrate the challenge of sending robots to extreme environments especially when information is limited. Europa, a moon orbiting Jupiter, a target for exploration due to the chance it may harbor extraterrestrial life (Left). The highest resolution pictures of Europa to-date, with each pixel representing 19 feet (Center). Artistic rendering of the proposed robotic lander which must be designed to adapt to a range of surface features (Right). *NASA*

as a location in the solar system that may harbor extraterrestrial life. However, it is an extreme environment with a surface temperature below -160 deg C and is far enough from Earth that any communication takes at least 30 minutes each way. Additionally, there is limited knowledge about the surface features of the icy crust of the moon, with the best pictures containing 19 foot per pixel resolution. To address this high uncertainty and extreme environment, a robotic lander is being outfitted with large legs to help adapt to surface features. Additionally, locomotion on the moon isn't being considered. Finally, the Europa Clipper mission will precede the proposed lander to help reduce uncertainty and select a landing site. The uncertainty of this extreme environment has impacted mission design, informed robotic system design, added significant financial cost, and limited the scope of the science objectives. In general, uncertainty in an environment can be addressed in robotic systems through adding redundant controlled degrees of freedom (DOF) or through use of structural compliance.

Adding controlled DOF to a robotic system can greatly increase its ability to adapt to a variety of situations and tasks; however, this approach is undesirable for extreme environments. Each additional controlled DOF in a robotic system aids adaptability but at the cost of an additional

actuator. However, in reality, each actuator also consumes power and is most effective with further sensing and computation to ensure it is being used effectively. Indeed, human hands which show high versatility can be modelled as having over 20 DOF. However, packing even close to 20 actuators into a small form factor without sacrificing strength is still a challenge for roboticists. This challenge becomes unfeasible for exploration in extreme environments where each actuator must be sealed from the environment, powered through limited on-board energy, and intelligently adapt to unexpected situations with limited supervision.

In contrast, passive compliance allows the robot to adapt where necessary without further computation or sensing. This passive compliance can act as a form of embodied intelligence and enables complex behavior through mechanical design. This approach has been widely used in the field of soft robotics and has been applied to a wide range of systems including grippers, locomotion systems, medical devices, and biomimetic robots. However, relying on mechanical compliance introduces a potential problem. Mechanical stiffness enables precise, fast, and high-force movement in robotics. Indeed, commercially available robotic arms used in factory floors which have no need for adaptability are capable of moving 120 kg payloads with sub-millimeter accuracy. Adaptability and mechanical strength are inversely linked through stiffness, as seen in Hooke's Law: $F = K \cdot \Delta X$. The stiffer the system, the higher force (strength) required for less deflection (adaptability).

## 1.2 Outline of the Thesis

In this thesis, I present robotic designs that can adapt to their environment in open-loop without sacrificing mechanical strength. This approach to design enables robotic missions to uncertain and extreme environments. This work falls under two main topics, gripping unknown objects and locomotion by growth, covered in Chapters 2 and 3 respectively. Though the methods used in each chapter differ, each design leverages application-specific features to reinforce the

robot. Chapter 2 discusses adhesion in under-actuated grippers, which leverage the geometry of target objects to increase overall grip strength. Chapter 3 considers highly compliant growing robots for unknown environments but considers how the environment itself can reinforce the robot and guide locomotion in open-loop. In Chapter 4, I present design approaches for different levels of complexity in grasping. In the simple case, nearly passive anchors can support large forces while still adapting to surface features. If greater complexity is allowed, magnetorheological fluid can be used as the working fluid in a soft robot with electo-permanent magnetic valves for a scalable high-DOF system.

# Chapter 2

# Adhesives for Underactuated Linkages

## 2.1 A soft robotic gripper with gecko inspired adhesive

The fluidic elastomer actuator has been a promising technology in the fast growing field of soft robotics [1] [2]. Consisting of a hollow elastomer membrane and driven through fluid pressure, these actuators have been used in both mobility systems [3–5] and in grippers [6–8]. Fluidic elastomer actuators have become more capable as researchers embed pressure, resistive [9], capacitive [10], magnetic [11], and optoelectronic [12] sensors, and apply them to medical rehabilitation [13], industrial sorting [14], and oceanographic exploration [6, 15] applications.

Elastomer actuators have proven particularly useful as grippers [14]. Due to their compliance, soft grippers can passively deform to match the shape of various target objects [2]. Both the hollow pressurized structure and soft materials associated with elastomer actuators create a tendency for the actuator to deform and evenly distribute loads, which typically limits the maximum applied force of an actuator to a safe range. This property makes many elastomer actuators suitable for interaction with humans [13] and fragile objects [6]. These actuators are appropriate for use in harsh environments due to their use of resilient elastomeric materials [3, 6]. Advances in efficient geometries [16], self-healing materials [17], and multi-material composite

structures [1, 15] have enhanced the capabilities of these grippers.




**Figure 2.1**: Gecko elastomer actuator grippers can achieve versatile grasps on complex shapes. The gripper passively deformed and reached this stable grasp to react a 20 degree twist applied to the base of the mug. (Mass of mug 397.7 grams).

Despite the promise of elastomer actuators and recent advances, challenges persist. The regulation of pressure through motion of fluid can introduce delays from 50 ms up to a few seconds [3, 16]. Soft materials complicate state estimation as material deformations are challenging to model [18]. Additionally, elastomer actuators cannot transmit as much force and torque as grippers with rigid links. Current actuators increase fluid pressure to increase stiffness and support larger loads, an energy intensive approach that has led to modest performance improvements [6, 19]. These challenges contribute to a lack of control authority.

The inherent compliance of an elastomer actuator is, of course, largely responsible for many of their desirable properties. However, the grip strength of an elastomer actuator relying upon a frictional contact is bounded by the stiffness of the actuator, friction coefficient, and the ability of the actuator to generate a normal force. Low grasp forces reduce the ability of elastomer actuator grippers to support high accelerations, jerks, or vibrations [18]. Furthermore, grasps of

large objects are challenging, restricting elastomer actuator grippers primarily to objects smaller than themselves [20].

To address many of these challenges, we introduce an elastomer actuator with a surface layer of gecko-inspired adhesives: the Gecko Elastomer Actuator. Gecko-inspired adhesives are a class of materials with micro-structured surfaces that generate adhesion using *van der Waals* forces [21]. Gecko-inspired adhesives can be used not only for adhesion, but also to dramatically enhance friction properties [22]. The adhesives are controllable and can engage or disengage at low forces [23, 24]. Because the adhesives are sensitive to the direction of applied load and to the real area of contact, the gripper must account for several new design principles, discussed below. The resulting gecko elastomer actuator grippers enable: 1) high strength grasps at low actuator pressures, 2) grasps of objects too large to enclose, 3) increased control authority, 4) faster actuation (through lower operating pressures), and 5) additional grasp options.

### 2.1.1 Background

There are two primary topologies of fluid driven elastomer grippers: digitated grippers and pouch grippers. Soft digitated grippers primarily use bending fluidic elastomer actuators, but can also employ cable drives, dielectric actuators, liquid crystal elastomer, or shape memory alloys [1, 2]. Variable stiffness grippers utilize particle jamming or magnetorheological fluid to rigidize, or simply grip by creating a suction contact [1, 25]. Variable stiffness grippers show high versatility and strength, but only on objects from specific classes of shapes. They typically require a large compressive preload and do not allow in-hand manipulation or dexterity. Soft digitated grippers utilize low stiffness to conform to objects and grasp with load-controlled friction [26]. These grippers are limited by their applied normal force or bending stiffness; these properties are typically coupled and depend on the internal fluid pressure. Recent works [6, 19] use pressures in excess of 300 kPa, enabling grasp of heavier loads. However, use of higher pressures comes with increased energy loss in fluid transmission, risk of rupture, and reduced surface conformation.

The introduction of gecko-inspired adhesives eliminates the need for large normal forces or increased bending stiffness and thus decouples the grip strength from internal pressure for fluid elastomer actuators. This innovation allows a gecko elastomer actuator (Fig. 2.11) to lift 11.3 kg at only 40 kPa of pressure.

Gecko-inspired adhesives are inspired by micro- and nano-structures found on the animals' toes [21]. These engineered structures are directional—when loaded in a preferred shear direction, they exhibit strong adhesion, but allow low-force release when loaded in other directions or when no shear load is applied [23]. Gecko-inspired adhesives can have long life, maintaining adhesion in the lab up to at least 30 000 cycles [27]. Performance is temporarily reduced in dusty conditions, but the adhesives are easily cleaned by contact with a tacky surface.

Synthetic materials that mimic some gecko adhesive properties fall into three classes: nanostructures, isotropic stalks, and directional stalks, with no material yet matching all of the amazing properties of the animal's toe pad. Both nanostructures, typically made of dense carbon nanotube bundles [28, 29], and vertical stalks of soft polymer with mushroom shaped tips [30, 31] provide strong adhesion, but require high forces to engage and release. Directional micro-scale stalks with mushroom shaped tips [32, 33] are controllable, but require the proper application of loads to realize adhesion. Directional wedge-shaped gecko adhesives [34] were chosen for this work due to their strong friction and adhesion properties, reusability, material compatibility with the elastomer actuators, and the ability to easily release an object as well as provide a strong grip.

Several soft grippers have utilized adhesives. Flexible electrostatic adhesive fingers have been used to manipulate soft goods [35]. Song et al. demonstrated an elastomer membrane coated in gecko-like hairs that showed normal load distribution across three-dimensional surfaces using a vacuum behind the membrane [36]. Due to the stretchable membrane and required preload, the gripper is best suited for loads of only a few newtons. Rigid-tile gecko-adhesive grippers are capable of supporting high forces on flat surfaces, with applications in industrial automation and in-space operations including capture of orbital debris [34], micro-gravity mobility [37], and



**Figure 2.2**: Active fingers allow for grasps on objects that do not typically support gecko-inspired adhesives.In many cases, the gecko elastomer actuator gripper does not depend on adhesion, but is enhanced by it. On dusty, irregular, or porous objects where adhesive performance is low, gecko elastomer actuator grippers still utilize force closure. (Mass of rock 150.1 g)

temporary anchoring [38]. However, these grippers lose adhesion on curvatures with a diameter less than a few meters. Dedicated curved surface grippers exploit adhesion-controlled friction to enable grasping at very low surface pressures [20, 34]. These curved surface grippers engage the entire adhesive area creating very strong grasps but are only suitable for smooth objects within a range of curvatures that depend on the size of the gripper. The gripper also relies on outriggers to engage the adhesive, which precludes wrapped grasps, limits the ability to grasp irregular objects, and increases the chance of damage in unstructured environments.

### 2.1.2 Design and Manufacturing

#### Design Principles

Three design principles enable effective utilization of gecko-inspired adhesives on a fluidic elastomer actuator:

1. The area of contact between the actuator and target surface should be maximized to engage as many adhesive features as possible [21].

2. The distribution of stress across the adhesives should be as uniform as possible to enable load sharing [27].

3. A shear load at the contact area must be generated to engage the gecko-inspired adhesive [38].

In cases where these principles are not met, the benefits of the adhesive are sacrificed, but the gripper recovers the properties of a typical elastomer actuator gripper (Fig. 2.2). Each microscopic wedge on the adhesive film produces a relatively small amount of adhesion and friction on its own; it is through load sharing that large forces are supported. This property drives the first and second principles enumerated above. To engage many of the wedges, a large area of the actuator must be in contact, and furthermore, if wedges are not loaded evenly, some will become overloaded and detach while others are not contributing.

To fulfill the second principle, a flexible but inextensible strain-limiting layer is used. In previous work, these layers were used as a structural asymmetry to convert expansion of the chambers of elastomer actuators into bending [1, 7, 15]. In the gecko elastomer actuator, the strain-limiting layer also ensures that all adhesive wedges in contact are loaded evenly in shear and that the actuator cannot stretch. Rigidly securing the strain-limiting layer at the base of the gripper creates an inextensible load path for the high force loads enabled by the adhesives.

The third principle can be satisfied either actively, by applying a shear load to symmetrically opposed pads of adhesive [34, 37, 38], or passively, by using the geometry inherent to the object being grasped [20, 34]. This latter approach only applies to objects with curvature; to grasp flat surfaces, an active shear preload must be applied. Effective adhesion to a flat surface requires the use of materials with high bending stiffness to distribute the adhesive loads. Since elastomer actuators typically have low bending stiffness, their performance on flat surfaces will be low.

To grasp these surfaces effectively, gecko elastomer actuators require an actuation-independent stiffening mechanism, such as a jamming component or phase transition element [25].

### Modeling the Torque of an Elastomer Joint

A computationally tractable modeling approach, approximating fluidic elastomer actuators as a series of joints, enables the design of elastomer actuators to address the first and second design principles. With narrowly spaced and thin walled elastomer pressure chambers, we can design to a specific torque profile. With more joints, each experiences a smaller bend angle. Thinner membranes are more difficult to manufacture but take less pressure to deflect and are less dependent on boundary conditions, allowing fast actuation with minimal energy input [16]. Our actuator required 15.7 millijoules of energy to deform 270 degrees.

Elastomer actuators provide an active mechanism for controlling the surface area in contact. Positive pressure bends the actuators towards an object. Applying a vacuum bends the actuator away and disengages the gripper. Increasing actuator pressure also stiffens the actuator, useful for applying torques. However, the profile of torque $\tau$ at point $s$ along an actuator of length $L$ must not exceed the Hirose distribution [39].

$$\tau(s) = \tau_0 \left(1 - \frac{s}{L}\right)^2 \tag{2.1}$$

Any monotonically decreasing torque profile that is upper bounded by Eq. 2.1 and lower bounded by $\tau(L) = 0$, will maintain surface contact, but with a non-uniform normal pressure. A torque profile greater than Eq. 2.1 will have outer joints that overpower inner joints and concentrate contact area into small regions. We present a model of elastomer joint torque that enables design of a specific torque profile.

We assume that strain only occurs at the thin-membrane face, that the entire membrane face is in contact, and that the effect of the joint angle on the moment arm is negligible. With these assumptions, the internal pressure and chamber geometry directly relate to joint torque. $A_f$

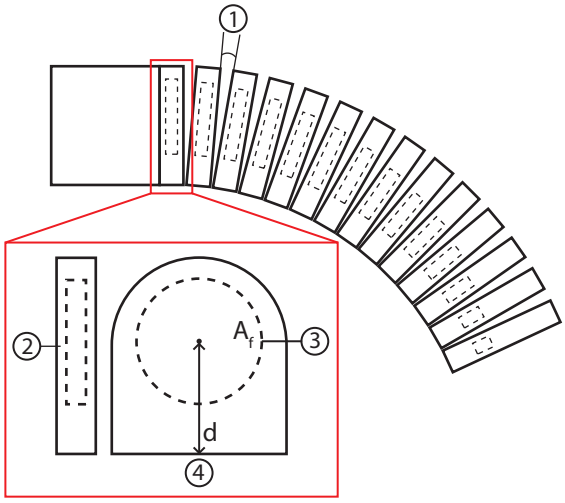



**Figure 2.3**: Model of a fluidic elastomer actuator as a series of discrete joints. Indicated are the joint angle (1); the thin membrane that undergoes the most deformation, side profile (2) and the area of the thin membrane (3) denoted by $A_f$; and the distance from the neutral axis of the actuator to the centroid of the thin membrane (4) denoted by $d$.

is the area of the face in contact, $P$ is the internal chamber pressure, $d$ is the distance from the neutral axis to the centroid of $A_f$ (Fig. 2.3):

$$\tau_{\text{joint}} = P \cdot A_f \cdot d \tag{2.2}$$

This torque model allows the design of an elastomer actuator to meet a specific torque profile. Given the profile in Eq. 2.1, if the hollow chamber geometry is comprised of semicircular faces with radius $r$ resting at the neutral axis, we can calculate the required the radius as a function of position along the finger $s$. For ease of manufacture, we do not change the outer dimensions of the actuator.

$$A_f(s) = \frac{\pi}{2} \cdot r(s)^2 \quad \text{and} \quad d(s) = \frac{4}{3\pi} \cdot r(s)$$

and torques

$$\tau_{\text{joint}}(s) = \frac{2P}{3} \cdot r(s)^3 \quad \text{and} \quad \tau_0 = \frac{\pi P}{2} \cdot r_0(s)^3$$

Setting the distribution $\tau_{\text{joint}}(s)$ equal to Eq. 2.1, the distribution of $r$ along the actuator length $s$ is

$$r(s) = r_0 \left(1 - \frac{s}{L}\right)^{\frac{2}{3}} \tag{2.3}$$

This model can be adapted for different chamber geometries and torque profiles. Given the inherent inaccuracies in the assumptions, this model serves primarily as a tool for designing a torque profile rather than for estimation and control. Our results contains model validation data, and demonstrates successful pressurization of an elastomer actuator without loss of contact area.

**Materials and Manufacturing**

This manufacturing process ensures that the adhesives form a smooth flat face, the bending stiffness of the actuator is low, and the stresses are transferred to the rigid base. The manufacturing process begins with casting a set of hollow elastomer chambers (Fig. 2.4-8) following a technique modified from [7, 15, 16]. To improve the fidelity of the designed torque profile, we use a high number of internal chambers to minimize the joint angles along the actuator. Each internal chamber is only 2 mm wide, with 0.56 mm thick strips of polycarbonate used during casting to create thin gaps between chambers. The thin membranes have wall thickness 0.9 mm while all other elastomer walls are at least 2.5 mm thick. These design values were near the limits of the manufacturing process and were chosen to best respect the assumptions of the model. This choice ensures most of the deflection while actuating is in the thin membranes, supporting assumptions from the model and allowing for a fast, low energy actuator. The resulting actuator bends 270 degrees at 17 kPa with an input of 15.7 mj of energy and takes less than 0.4 seconds.

To provide rigid mounting points for the strain-limiting layer (Fig. 2.4-4), a 3-D printed anchor (Fig. 2.4-6) (FormLabs) and silicone pneumatic tubing (Fig. 2.4-7) are cast directly with the chambers. With unsealed elastomer chambers (DragonSkin 20), we begin with (Fig. 2.4-A) creating gecko-inspired wedges (Fig. 2.4-2) by casting MoldStar-30 on a wax daughter mold

(Fig. 2.4-1) and allowing partial cure (20 minutes at 50 degrees C). We then build up the structural layers (Fig. 2.4-B), comprised of three layers of DragonSkin-20 spun at 800 rpm for 1 minute. The layer interfacing the wedge layer (Fig. 2.4-3) is cast before the wedges have fully cured to increase the bonding strength of dissimilar silicones. The strain-limiting layer contains a polyester mesh and a final interface layer (Fig. 2.4-5) is cast above to seal any air channels trapped in the strain-limiting layer and to ensure a flat surface. To conclude the process (Fig. 2.4-C), the elastomer chambers are bonded to the interface layer by pressing the chambers onto a thicker layer of uncured DragonSkin (400 rpm for 2 minutes).

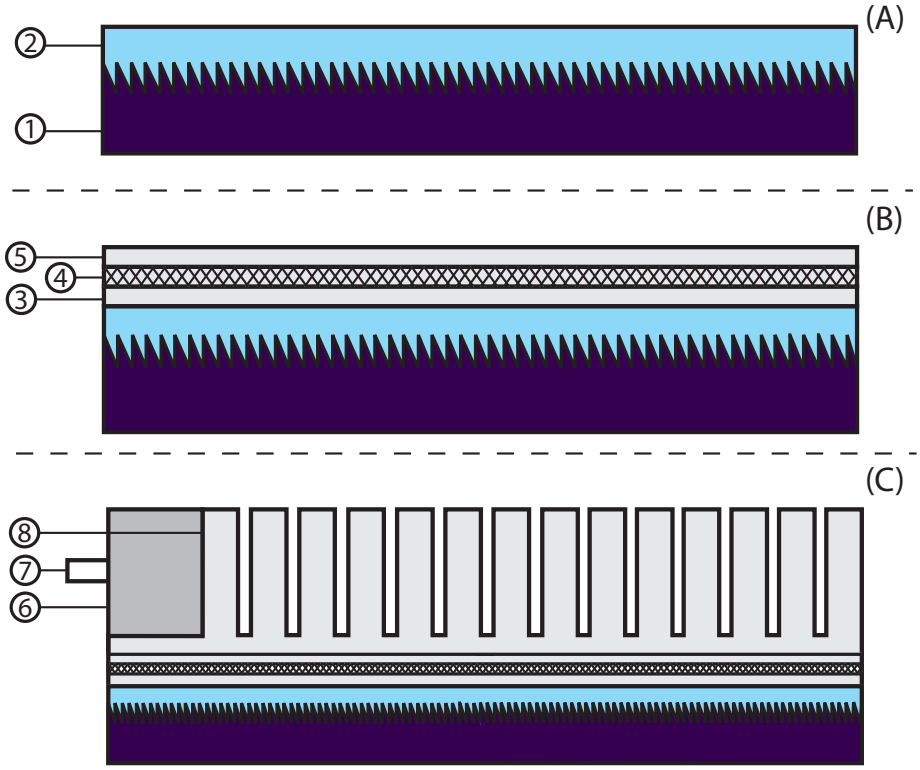



**Figure 2.4**: Multi-step manufacturing process of pneumatic soft gripper with gecko-inspired adhesive. A thin film of gecko adhesive features is cast from a mold (A). Structural layers are built up on the adhesives, incorporating a strain-limiting layer to support loads (B). The resulting membrane is bonded to the chamber geometry and plumbing (C). The process can be generalized to suit a broad range of adhesive daughter molds & the variety of approaches used to cast elastomer actuator chambers.

The gecko elastomer actuator has only a few components and the total cost of raw materials

is only $7.25 at quantity 1 ($1.50 silicones, $1.50 pneumatic tubing and fittings, $2.75 3-D printed components, $1 strain-limiting layer, $0.50 wax for adhesive mold). The complexity of adding gecko-inspired adhesives to elastomer actuators varies depending on the adhesive mold. Not all molds are reusable, and design or fabrication of a mold from scratch can be an intensive process. Since we employ reusable molds and cast from a master developed in prior work [21, 33], adding the adhesive layer does not add significant cost or complexity to the manufacturing process ($<$\$2, $<$1 hour).

### 2.1.3 Results

#### Model Evaluation

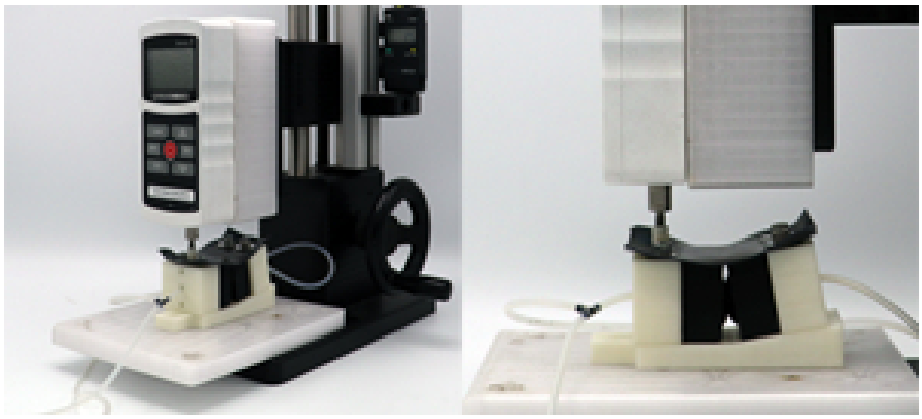


**Figure 2.5**: Experimental setup to validate the torque generated by a single elastomer actuator joint. The joint is fixed to the desired angle by the combination of the forge gauge and a 3D printed support; the joint is then pressurized as force readings are taken with the gauge.

Tests performed at various chamber pressures and joint angles validate model predictions of the joint torque generated by elastomer actuators. Rigid brackets on each end of the joint provided an inextensible fixture and fixed moment arm for force measurement. The bottom bracket enforced the angle of the joint. Torque was calculated from force measurements recorded using a force gauge (Mark-10 M5-10). Fig. 2.5 shows the experimental setup.

When the joint angle is at zero degrees, the model accurately predicted the output torque

with two notable exceptions; nonlinearity not captured by the model and the measured torque eventually exceeded the predicted torque (see in Fig. 2.6). This nonlinearity can be explained by the thin-membrane not translating evenly but instead stretching from a bounding edge. Consider the real area in contact between two adjacent faces, denoted by $A_c$. At $P = 0$, $A_c = 0$ but with increased pressure and strain, $A_c$ approaches $A_f$. At a large enough pressure, the membrane bulges outwards and will begin to yield $A_c > A_f$. A higher joint angle then serves to exacerbate the nonlinearity. With a larger joint angle, the initial gap between faces is larger, requring additional pressure and strain to reach $A_c \neq 0$. This explains the larger overprediction of the model at lower pressures at higher joint angles in Fig. 2.6. Furthermore, given the semi-circle geometry of the faces, $d$ varies not only with $r$ but also with $P$, resulting in reduced model accuracy at low pressures. While the accuracy of this modeling approach depends on actuator design, position, and pressure, several factors mitigate modeling error when used for design of a torque profile: 1) the chamber pressure is uniform within an actuator, 2) the discrepancy between modeled and measured torque is minimized as $P$ increases, and 3) the use of many joints reduces the angle in each joint for a given actuator posture. For these reasons, we believe that this model allows for sufficiently accurate design of a specific torque profile. We evaluate the behavior of complete actuators to support this claim.

We used Frustrated Total Internal Reflection (FTIR) to validate actuator behavior with a torque profile described by Eq. 2.1. FTIR measures the real area of contact between two surfaces [20]. We built a cylindrical FTIR sensor with white LEDs illuminating the edge of a polycarbonate surface. We compared an actuator with torque profile according to Eq. 2.1 with an actuator described by a uniform profile $\tau(s) = C$. Varying the pressure in an actuator while in contact with the FTIR surface highlights the effect of the torque profile of an actuator. As seen in Fig. 2.8, the addition of pressure to the uniform torque profile actuator had the effect of decreasing contact area. Distal joints overpowered more proximal joints, lifting large portions of the finger off of the surface. The actuator with the torque profile defined in Eq. 2.1 maintained

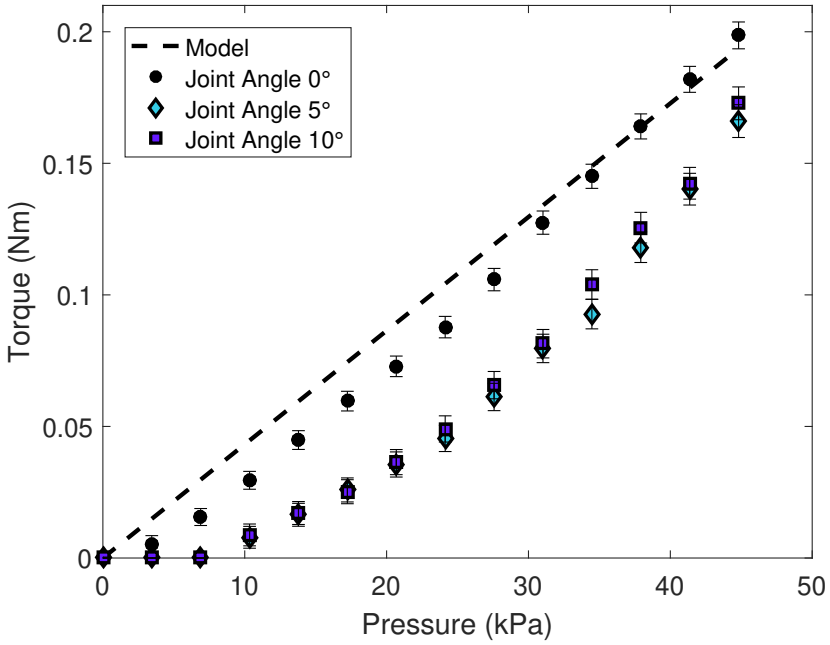



**Figure 2.6**: Torque generated by an elastomer joint at varying angles compared to the model prediction in Eq. 2.2.

high contact area across a wide range of pressures. This actuator experienced a small area loss due to internal pneumatic chambers bulging against the surface, but this loss is small.

### Large Object Grasp

Gecko-inspired adhesives enable the gripper to grasp objects too wide to be enclosed. Fig. 2.9 compares the grasp capability offered by otherwise identical elastomer actuators with and without gecko adhesive when grasping large objects. The actuators have a width of 2 cm and length of 6 cm. Using 27 kPa of pressure, we measured grasp force on a set of polycarbonate cylinders (diameters 57 to 203 mm) using a force gauge (Mark-10). The two smallest targets allowed the grippers to wrap beyond the widest point of the cylinder. Data for the non-adhesive gripper shows a significant difference in pullout force for this case, when a wrap grasp is possible. The gecko elastomer actuator gripper provided 35.66 N more force on the 57 mm cylinder (a 348% increase) and 8.58 N more force on the 203 mm cylinder ( a 2095% increase) compared to

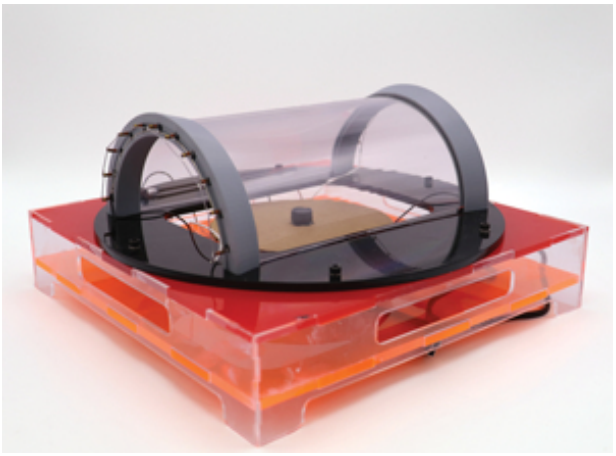


**Figure 2.7**: Cylindrical FTIR sensor used to measure contact area. Rings of LEDs illuminate the ends of the cylinder. A wide angle camera located on the axis of the cylinder captures the results. Images are captured with minimal ambient light, and subtraction of a dark frame in post processing calibrates the sensor.

the non-adhesive gripper.

This improved performance aligns with prior models of gecko-inspired adhesive grippers [20]. The adhesive grippers exploit adhesion-controlled friction rather than load-controlled friction [26]. Both grippers apply force to the object through frictional forces. In the case of the non-gecko gripper, this friction depends on the normal load applied by the actuators. For the gecko adhesive gripper, the friction is adhesion-controlled, meaning the friction force is dependent on the total contact area, not normal force. This allows the gecko elastomer actuator gripper to support large grasp forces—with low fluid pressures—by regulating contact area.

A benefit of the gecko elastomer actuator is stronger grasp at lower actuation pressures. Fig. 2.10 compares the grip strength of the grippers using gecko elastomer actuators and non-gecko actuators on both large and small cylinders across a range of fluid pressures. On the 203 mm cylinder, the effect of pressure is small for both actuators, but the gecko elastomer actuator gripper supported an additional 6.5 N at all pressures. On the small radius cylinders using force-closure grasps, the gecko actuators significantly outperformed the non-gecko actuator. At low pressures the gecko elastomer actuator gripper yielded a rapid increase in grip strength as

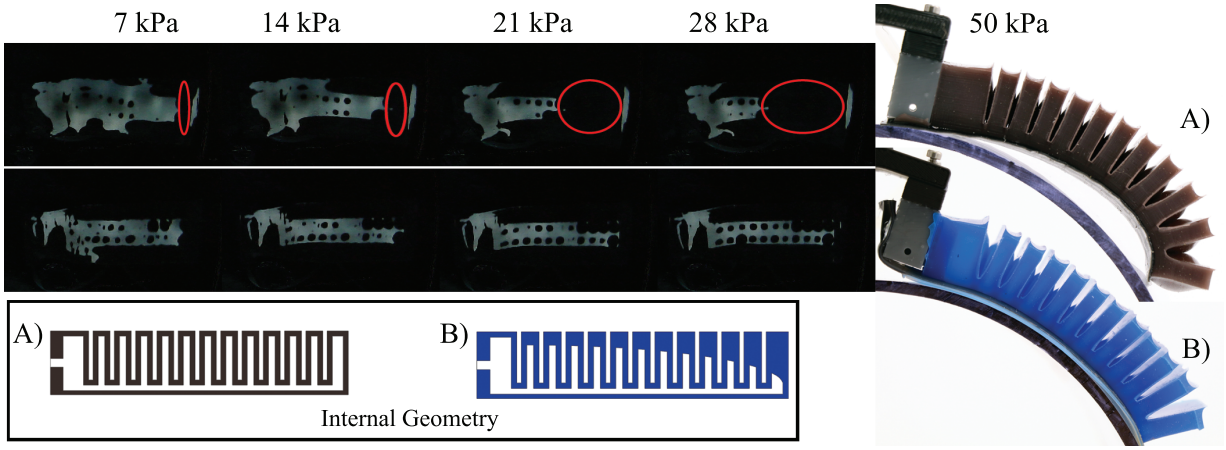



**Figure 2.8**: Images captured on FTIR sensor showing torque behavior of the optimized gripper. Bright areas indicate contact between the actuator and surface. Actuator A: uniform torque profile $\tau(s) = C$. Actuator B: Torque profile follows Eq. 2.1. Actuator A lost significant contact area (highlighted in red) due to most of the actuator flexing away from the surface. Actuator B can maintain a high degree of contact area during pressurization.

the additional pressure created more real area of contact and adhesive engagement. This reaches a maximum when all of the adhesive area is engaged. Once this maximum is reached, additional pressure will still stiffen the actuator but does not force the actuator off the surface.

### High Strength Grip

To show the performance improvement of using gecko elastomer actuators in wrapped grasps, we designed a high-load gripper. This gripper (Fig. 2.11) uses three actuators for increased contact area and stability, wider elastomer actuators for increased surface area (3.6 cm by 8 cm), and high stiffness nylon/carbon-fiber composite brackets. The gripper can operate at higher pressure to maximize the contribution of both adhesion-controlled friction and bending stiffness from the elastomer actuators. The elastomer actuators create force closure and the gecko-inspired adhesives prevent shear sliding, significantly enhancing pull out strength. The high-strength gripper supports over 111 N (25 lbf) at a chamber pressure of 40 kPa (Fig. 2.11).

This demonstration was conducted on a KUKA LBR iiwa robotic arm. The gripper can lift over 111 N, measured by the mass of the payload. This grip was secure, repeatable, and

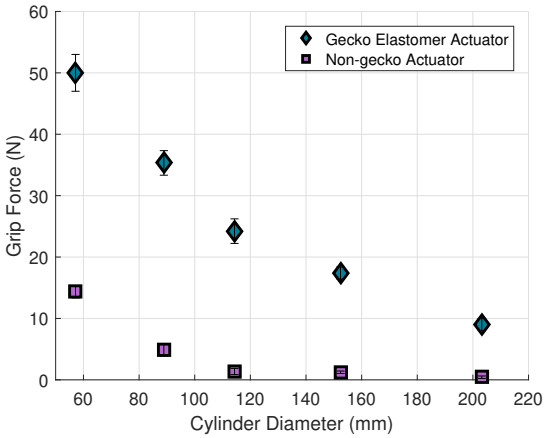



**Figure 2.9**: Gecko elastomer actuator grippers provide a stronger grasp across a wide range of cylinders.

robust to the dynamic effects associated with accelerations in the payload. The teleoperated robotic arm picked the payload up from rest, lifted and translated the payload, released the payload in a controlled manner, and did not need a planned trajectory or precise payload position. This procedure was repeated several times, with variations in the payload position and gripper orientation to demonstrate robustness to misalignment. The gripper does not exhibit any visible plastic deformation or loss of performance after testing (over 25 trials).

### Control Authority

Gecko elastomer actuators provide improved control authority for manipulation tasks. The ability to achieve higher ultimate grip strengths on many objects allows manipulation of heavier objects as well as more rapid accelerations of objects during tasks. This is especially useful for pick and place operations, where speed is critical. Additionally, because lower pressures can be used for gecko elastomer actuators, actuation is faster and more efficient. The gecko elastomer actuator maintains the low energy input and fast actuation seen in actuators optimized for these properties while using adhesion-enhanced friction for higher strength grips. Most soft grippers must undergo significant pressurization to become stiff enough to lift large loads. The

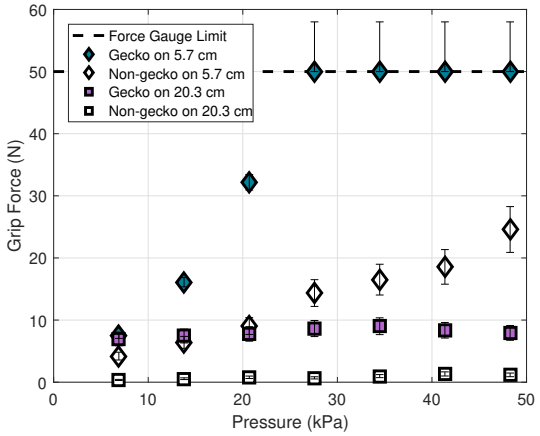



**Figure 2.10**: Evaluation of chamber pressure for gecko/non-gecko elastomer actuator grip strength.

gecko-adhesives remove this requirement and allow for the actuator to remain much softer, while supporting similarly large loads (Table 1). For reference, Mosadegh et al. presented a gripper that actuated 270 degrees in 200 ms at 117 kPa of internal pressure with 115.9 mj of energy input [16]. The pair of gecko elastomer actuator fingers require 31.4 mj of energy input to actuate the same distance, taking 400 ms at 50 kPa.

**Table 2.1**: Comparison of recent high-load fluidic elastomer actuators.

| Gripper | Pressure (kPa) | Lift Force (N) |
|---|---|---|
| Yap, 2016 [19] | 300 | 25 |
| Galloway 2016, [6] | 310 | 52.9 |
| Gecko 2 Finger: Fig. 2.1 | 28 | 50 |
| Gecko 3 Finger: Fig. 2.11 | 40 | 111 |

Gecko elastomer actuators also provide fundamentally new capabilities where adhesion makes previously unstable grasps possible (Fig. 2.9). This increase makes a much wider variety of configurations for grasping a given object and is more robust to positioning errors in the grasp location. These factors are particularly important given the imprecise state estimation and actuation time delays [14] typical of soft robots. Fig. 2.12 illustrates the variety of grasp options available for handling a coffee mug, many of which would not be possible with a non-gecko

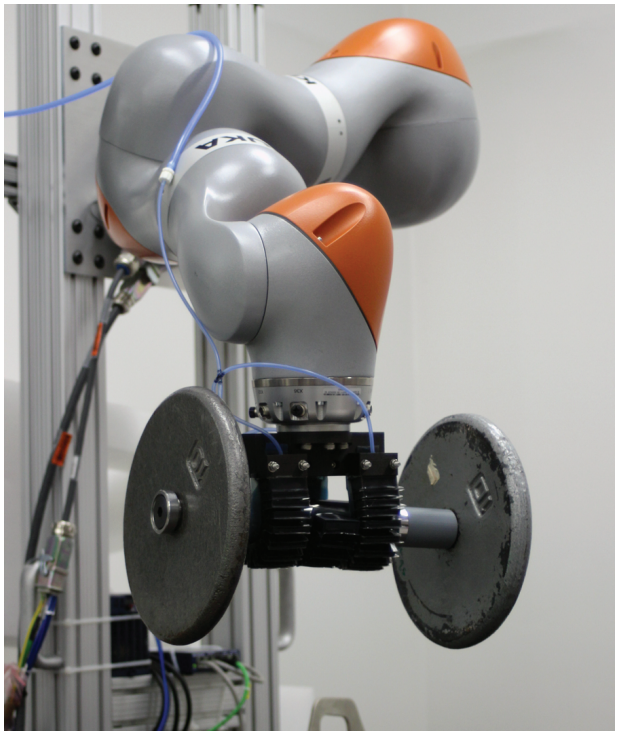


**Figure 2.11**: Three actuators create a wrapped grasp, engaging the gecko-inspired adhesives and supporting an 11.3 kg (25 lb) mass at 40 kPa of pressure.

elastomer actuator gripper.

This work shows how gecko elastomer actuators deliver new capabilities (grasping large curvature and new grasp configurations) and improve performance in other cases (higher strength grasps, lower fluid pressures, faster operation). This work serves as a guide for making gecko elastomer actuators and demonstrates their applicability to high-load applications. When the adhesives do not contribute to grip strength, the performance of non-gecko actuators is recovered. Reducing energy input and increasing grip strength will help extend the use of soft robotics into industrial automation and other applications. New models that promote surface conformation across a range of fluid pressures may also be applied broadly to other fluid elastomer actuators.



**Figure 2.12**: Elastomer actuator grippers with gecko-inspired adhesives are capable of a wide range of stable grasps. Gecko-inspired adhesives enhance grasp choice by reducing the minimum chamber pressure for a stable grasp and by increasing grip strength at a given chamber pressure. Gecko-inspired adhesives also enable grasps that are not possible through load-controlled friction.

## 2.2 Robust capture of unknown objects with a highly under-actuated gripper

Most robotic end effectors are not capable of grasping objects too large to enclose unless purpose-built for the task [40]. A gripper capable of grasping large objects and adapting to unknown geometry has several practical applications including terrestrial package handling and sorting tasks. This challenge is also of interest to NASA, motivating technologies that aid in the servicing of spacecraft and orbital debris [41, 42]. For space applications, versatility is essential due to the cost of launch, variety in spacecraft, and inability to alter hardware post-launch. Capturing a large object of unknown geometry or orientation precludes the use of most available robotic grippers. Parallel jaw grippers are well suited for industrial settings and small objects, but struggle with large or irregularly shaped objects [43, 44]. Adhesion based grippers are well

suited to capturing large objects and are in development for use in space [35, 42, 45]. However, the force of these grippers scales with contact area, and conformation to an object of unknown shape remains a challenge [36, 46, 47]

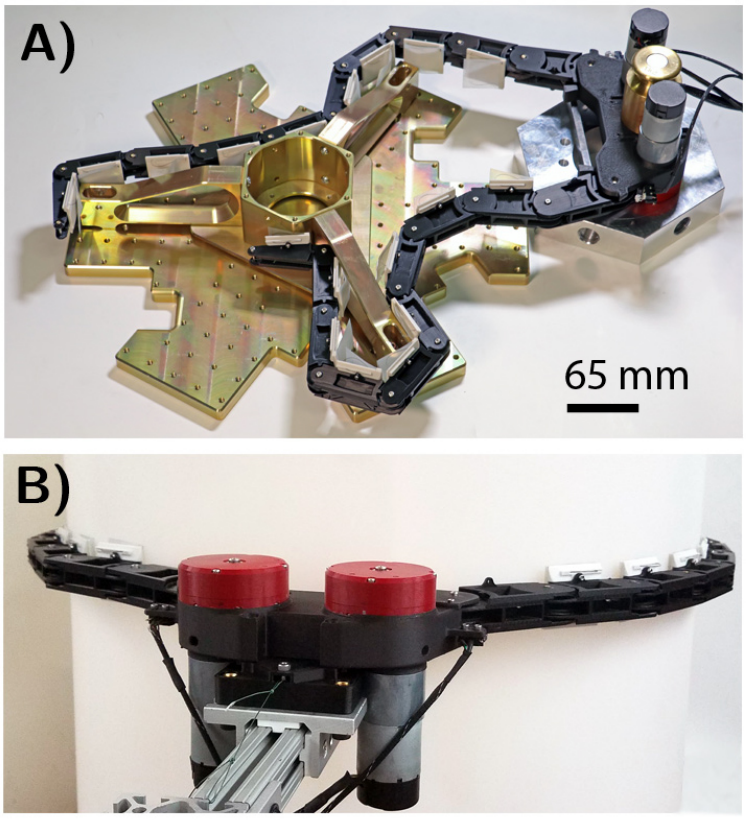



**Figure 2.13**: Highly under-actuated mechanisms exhibit several unique properties that are well suited to grasping large and irregular objects. A) These mechanisms can closely match an object's shape and increase the number of points in contact. B) By deploying from a retracted position along a surface these grippers can enclose large objects, such as this cylinder.

Under-actuated grippers capable of conforming to arbitrary shapes and surfaces offer a potential solution [39, 48]; however, to grasp large objects, an under-actuated gripper should have many joints. Using many joints improves conformation, reduces pressure on the surface of the object, and facilitates mechanical interlocking [49–51]. In fact, one of the first under-actuated grippers —introduced in the 1970's— had many links and popularized the field [39]. While researchers have focused on the development of under-actuated grippers with two or three degrees

of freedom (DOF) [48, 52, 53], little progress has been made on systems with a high DOF. This is the result of a fundamental contradiction in highly under-actuated grippers: they are best suited for tasks involving unknown geometry, but also need to be designed for a specific geometry in order to guarantee strict stability. Strict stability is defined here as each link pushing into the target object with a positive force. There are designs that can guarantee strict stability across a large configuration space for low-DOF under-actuated grippers [48], but this becomes difficult with more DOF. This contradiction masked the potential benefits of highly under-actuated systems, and the field has been under-explored with several exceptions [39, 49].

Grippers from the field of soft robotics are a notable exception to this contradiction and inspired this work [1, 7, 54]. Soft grippers comprised of pneumatic transmissions and soft elastomeric bodies have infinite degrees of freedom. Prior methods of analysis predict that given the infinite dimension of the configuration space, these grippers would be limited by instabilities [48]. However, while many of these grippers do show instability in some cases, this has not precluded their widespread use [54, 55]. The versatility of soft grippers has shown that a successful gripper does not depend entirely on grasp stability, motivating further investigation in highly under-actuated linkages. Furthermore, one of the reasons soft grippers are not limited by instability is the high friction of elastomers, which we investigate as an approach to stabilize highly under-actuated linkages.

In this project, we developed a highly under-actuated gripper (Fig. 1) with five primary strengths: 1) grasp success without requiring strict stability, 2) conformation to irregular shapes, 3) reconfiguration to improve grasp strength, 4) enclosure of large objects, and 5) simplified positioning, control, and sensing. Our hardware builds on the work presented by Hirose et al. [39] by designing both antagonistic pulley mechanisms in tandem to achieve joint torques, adding hard-stops to set a specific retract configuration, and reducing manufacturing complexity/mass by using modern rapid prototyping techniques. We also provide computationally simple tools that generalize the design of highly under-actuated grippers. In this work we address the two primary

weaknesses of highly under-actuated grippers shown by Gosselin et al. [48]: that increasing the number of links both decreases the forces applied by the gripper and increases the chance of instability. We show that using high friction or using two independent actuators in a single linkage each can stabilize a grasp and increase grip strength without propagating instability. To get high friction with low normal forces, we use gecko-inspired adhesives which provide an adhesion-controlled friction, enhancing operation on delicate surfaces such as a spacecraft. In this way, gecko-inspired adhesives can address both issues: preventing instability and reducing the need for large forces to grasp effectively. Our mechanism allows for gripping a wider range of surfaces than prior adhesive grippers since the linkage conforms independently at each joint to engage the adhesive and create mechanical interlocks [46, 47, 56, 57]. To evaluate the gripper, we measure the force at each link and measure grasp strength on a set of four objects. Finally, we demonstrate the unique properties such as conforming to a human hand, capturing a non-adjacent object, and deploying along non-contiguous objects.

### 2.2.1 Design Principles

Each linkage in the under-actuated gripper has two primary components: 1) a transmission capable of generating prescribed torques across many joints and 2) a series of links joined by revolute joints that conform to arbitrary geometry and convert torques into surface pressure. In the following subsections we provide tools to aid in the design and evaluation of this family of under-actuated grippers.

Static analysis aids in the design and evaluation of these grippers. The free body diagram (FBD) is identical at each joint and can be used to generate equations for static equilibrium (Fig. 2.14). This analysis assumes strict stability, where each link is pushing into a surface with a positive force. These equations require a known configuration about which the transmission can be designed, referred to as the design surface $[\vec{c}, \vec{\theta}]$. A torque at each joint $\tau$ rotates the link and must be reacted by the adjacent proximal link. Links make contact with a surface at a center of

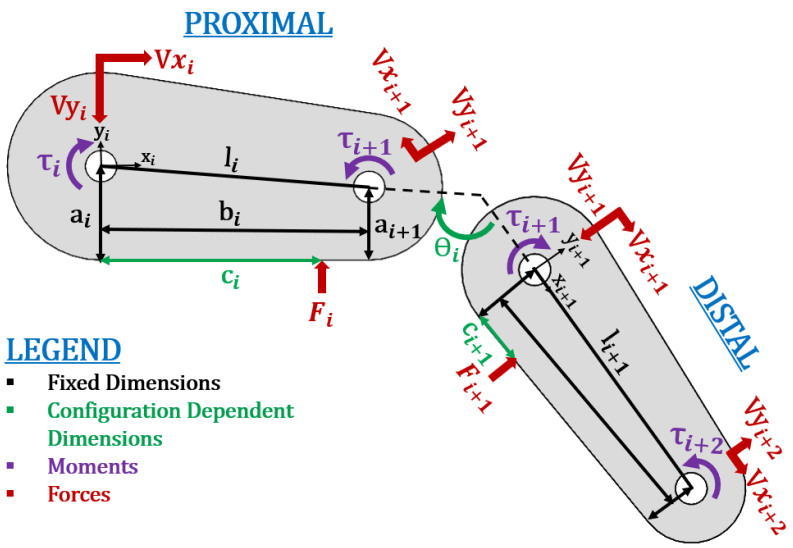



**Figure 2.14**: A free body diagram of each joint can be used to solve for unknowns. Each link has torque $\tau_i$ and link length $l_i$. Each link applies a grip force $F_i$ into the surface with center of pressure located distance $c_i$ from joint $i$. The distal link is at an angle $\theta_i$ relative to the proximal link. The force necessary to keep the link on the surface is $V_i$, which grows from tip to base. $\tau_i$ also balances the moments of the distal reaction forces, $Vy_{i+1}$ and $Vx_{i+1}$ with lever arms $b_i$ and $(a_i - a_{i+1})$.

pressure (COP) at distance $c$ and apply grip force $F$. Remaining engaged on the surface requires reaction forces from $Vx$ and $Vy$ (Eq. 2.5, Eq. 2.6), with increasing magnitude $V$ from the tip to the base of the linkage (distal to proximal).

Each joint is offset from the design surface by a distance $a_i$, and the distance $b$ converges to the link length $l$ if $a_i = a_{i+1}$ (Eq. 2.4). The reaction forces of the adjacent distal link $(Vx_{i+1}, Vy_{i+1})$ will impart moments proportional to $b_i$ and $(a_i - a_{i+1})$. The coordinate frame of the reaction forces $(x, y)$ is a body fixed frame at each joint where $y_i$ is normal to $b_i$.

We assume gravity, mass, and inertia are negligible because our analysis is quasi-static and the links are lightweight. These assumptions are fitting for tasks in orbit and are reasonable if the torques are sufficiently large. In practice, inertial effects during rapid deployment and retraction result in unique behaviors (Section V). We also consider the links rigid bodies and neglect friction in the joints, transmission, and design surface.

In Algorithm 1 we analyze the gripper at each joint sequentially starting from the distal

end. This analysis yields a torque difference $(\Delta\tau)$ between each joint that will stabilize the linkage for a configuration consistent with the design surface (Eq. 2.7). In other configurations, stability is not guaranteed and links can buckle off of the surface. In other words, the torque at a given link must be sufficient to keep the following distal link pressed into the surface (Fig. 2.19 B).

Algorithm 1 (equations 2.4-2.7) also derives the normalized vector $\vec{\tau_{pat}}$; referred to as the *torque pattern*. This pattern defines the torque ratios required to maintain strict stability on the design surface for user-defined parameters $\vec{a}, \vec{c}, \vec{l}, \vec{F}, \vec{\theta}$. The grip force profile $\vec{F}$ defines the shape of the force distribution across the gripper. These equations consider arbitrary design surfaces, force profiles, and linkage geometry, generalizing the design of highly under-actuated grippers [39].

$$b_i = \sqrt{l_i^2 - (a_i - a_{i+1})^2} \tag{2.4}$$

$$Vy_i = Vy_{i+1} \cdot cos(\pi - \theta_i) - Vx_{i+1} \cdot cos(\theta_i - \frac{\pi}{2}) + F_i \tag{2.5}$$

$$Vx_i = Vy_{i+1} \cdot sin(\pi - \theta_i) - Vx_{i+1} \cdot sin(\theta_i - \frac{\pi}{2}) \tag{2.6}$$

$$\Delta\tau_i = \tau_i - \tau_{i+1} = Vy_{i+1} \cdot b_i + Vx_{i+1} \cdot (a_i - a_{i-1}) + F_i \cdot c_i \tag{2.7}$$

The transmission was designed to deploy the links along a surface sequentially from base

to tip, conforming to the surface. When all the links have rotated towards the target surface, the gripper is fully deployed. From that point, $\vec{\tau}$ can be scaled higher or lower to control grip pressure, or the linkage can be retracted into a spiral leaving the surface sequentially from tip to base. Retracting into a spiral is a spatially efficient storage configuration for long linkages.

In our case the $\tau$ is the sum of grip and retract torques $(\tau_E, \tau_R)$ at each joint (Eq. 2.9). The grip and retract pulley series were designed in tandem to increase the $\Delta\tau$ achievable at each joint within practical design constraints such as maximum and minimum pulley sizes. These torques result from applying cable tension $T_E$ to the grip pulleys of radii $\vec{r_E}$ and $T_R$ to retract pulleys of radii $\vec{r_R}$.

According to (Eq. 2.9) sequential motion simply requires $\tau$ to monotonically decrease from base to tip. Positive $\tau$ will deploy the gripper and negative $\tau$ will retract the gripper. If the gripper is initially retracted, a quasi-static analysis without gravity, friction, and inertia predicts that the proximal links with greater torque will actuate before distal links with less torque. In practice, friction and inertia place limits on the torques required for sequential motion. In most cases the $\Delta\tau$ needed to prevent links from buckling off the surface will inherently enforce sequential motion.

$$\tau = \tau_{Ei} - \tau_{Ri} = T_E \cdot r_{Ei} - T_R \cdot r_{Ri} \tag{2.8}$$

$$F_i = \frac{\Delta\tau - Vy_{i+1} \cdot b_i + Vx_{i+1} \cdot (a_i - a_{i+1})}{c_i} \tag{2.9}$$

If a linkage is designed using Algorithm 1 but in a configuration not consistent with the design surface $[\vec{c}, \vec{\theta}]$, stability is not guaranteed. Here we invert the problem and assuming a transmission design $\vec{r}$, evaluate stability and the inward grip force profile $\vec{F}$ in a new configuration.

In Algorithm 2, iterating the forces in each link using equations 2.4, 2.9, 2.5, and 2.6, each link is evaluated from tip to base to solve for $F_i$. If $F_i < 0$ is needed to satisfy the FBD, then that link is unstable and will leave the surface because $F_i < 0$ cannot be realized on a static surface. We chose to approximate the instability by resetting negative grip forces to zero (not in contact with surface). This approximation will generally further destabilize the predictions of Algorithm 2 because $F_i$ remaining negative decreases the force and moments necessary for proximal links to be stable. In practice, links leaving the surface led to more instability and resetting $F_i$ in the case of instability enables Algorithm 2 to capture this trend. However, using an iterative approach avoids building an analytic expression for the Jacobian which can be advantageous when modifying models to account for loss of contact or friction forces.

One of the key properties of under-actuated grippers is the ability to reliably grasp without modeling the interaction. Low-DOF under-actuated grippers are capable of this task because designs exist that guarantee stability across a large configuration space. As the dimension of the configuration space increases, guaranteeing strict stability over large and contiguous regions becomes increasingly difficult [48]. We introduce two complementary methods that can stabilize an unstable configuration: high-friction interface materials and use of two actuators per linkage.

*Using Surface Friction-* In general, surface friction cannot be used to guarantee stability since the friction is both configuration and material dependent. Surface friction refers to the friction between the linkage and the surface it contacts. Neglecting surface friction will generally predict instability for highly under-actuated grippersGosselin et al. establish that surface friction provides a torque that counteracts motion and acts towards stabilizing the configuration in all cases [48]. Surprisingly, friction even helps stabilize links that are not pushing into the surface because links elsewhere held in place by friction prevent an instability from propagating throughout the gripper. Consequently, highly under-actuated linkages often have one or more links not pushing into the surface, but the system as a whole still performs as desired. Finally, surface friction does not impede retracting, since the normal force drops during retraction. We use friction

to stabilize highly under-actuated grippers in arbitrary configurations and use gecko-inspired adhesives to provide normal load-independent friction. We demonstrate friction stabilizing the gripper (Fig. 2.19) and also show that friction can prevent instabilities from propagating on arbitrary surfaces by measuring the forces on each link (Fig. 2.20)

*Using Two Actuators Per Linkage-* Surface friction depends on normal forces, and using two actuators per linkage can increase these normal forces without causing an instability to propagate. Using two actuators instead of one to control the linkage offers the ability to simultaneously scale the tension in each pulley series. If both the grip and retract tension are scaled by the same factor, the torque pattern is preserved and system stability is maintained. Similarly, the forces into a surface will be scaled by the same ratio, increasing friction.

### 2.2.2 Mechanical Design

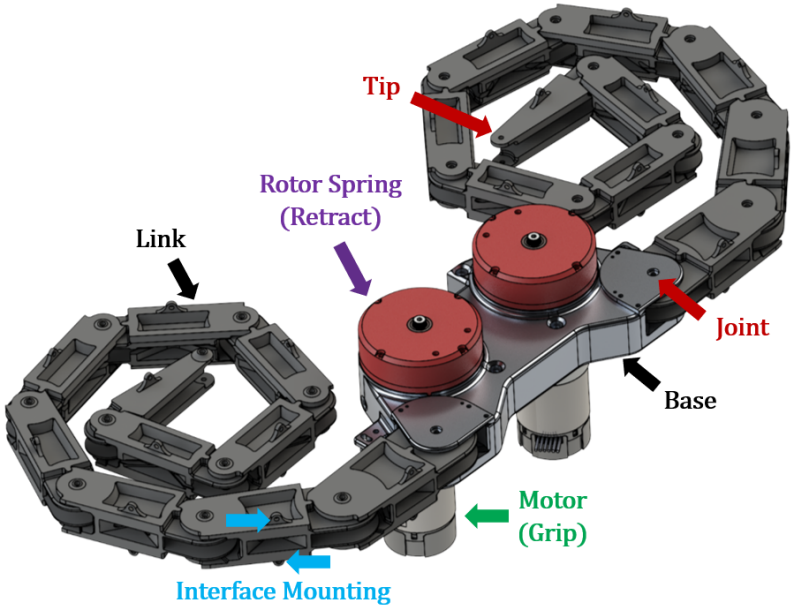



**Figure 2.15**: A CAD rendering of a highly under-actuated gripper with two opposing linkages. Each linkage has 10 links, 10 joints, 2 pulleys at each joint, a motor-actuated grip series, and a spring-actuated retract series. Each link has mounting for friction interfaces.

We present a gripper with two opposing linkages similar to that presented by Hirose et

al. [39] (Fig. 2.15). The transmission consisted of two independently driven pulley mechanisms that opposed one another to generate a net torque at each joint. The links were joined with shoulder bolts that each held two pulleys that rotated independently (Fig. 2.16).

Each linkage consisted of both a grip and retract pulley series that work in opposition. The grip series was actuated by a brushed DC motor while the retract series was coupled to a rotor spring. The spring was preloaded and provided nearly constant stiffness throughout the cable stroke. Ball bearings (R133-2Z) minimize friction at the joints, allowing the pulleys to rotate without resistance. Standard plain bushings were not used because they develop substantial friction that increased with the joint load. The links and pulleys were 3D printed from carbon fiber filled PLA to make them lightweight, stiff, and easy to manufacture. Each link also had mounting points for interchangeable interface tiles that can be outfitted with different materials. The interface tiles had a large impact on grip strength and four different types were evaluated on a variety of surfaces (Section V).

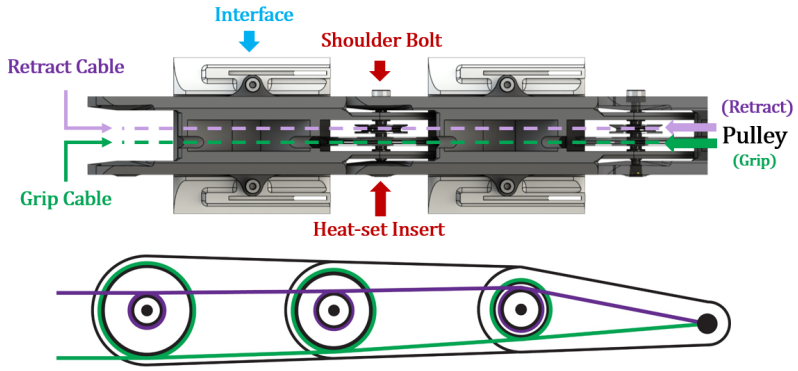



**Figure 2.16**: Linkage mechanism: The links are joined by shoulder bolts that each hold a retract and grip pulley. Cables wrapped in opposite directions provide antagonistic actuation and are both fixed at the tip.

The more links in an under-actuated gripper, the more important it becomes to densely package $\Delta\tau$ in the transmission. The torque pattern, $\tau_{pat}$ generated by Algorithm 1 will demand an increase in torque from tip to base. A vector of pulley radii needed for the transmission is found by scaling $\tau_{pat}$ by the smallest manufacturable pulley radius. Therefore, the size of a

gripper with this transmission is directly related to the lower limit of the pulley radii. With more links the required range of torques from tip to base $(\tau_n - \tau_1)$ and subsequently the radius of the largest pulley will both increase. Large pulleys place limits on gripper scalablity and transmission packaging.

The $\tau_{pat}$ achievable with the transmission is constrained by practical limits such as size and tension. Algorithm 1 does not model friction and thus over-predicts the pulley radii necessary to stabilize a configuration. For a flat design surface, uniform link geometry, and uniform COP, Algorithm 1 prescribes a quadratic increase in torque from tip to base (as seen in [39]). If every link has the same COP, the rate of the quadratic governing $\tau_{pat}$ increases as the COP decreases and vice versa. Monotonic curvature actually reduces the torque required to stabilize because the shear force at each link will be divided into components and the horizontal component has a small lever arm; contributing little to the torque that must be reacted (Fig. 2.14).

The pulley sizes can be designed with Algorithm 1, but in our case many of the pulley radii were outside our physical size constraints, so we adjusted the transmission by fitting a quadratic function between the smallest and largest practical pulley radii for both pulley series. The grip series grows whereas the retract series shrinks from tip to base (Fig. 2.17). This approach allows greater $\Delta\tau$ without increasing the largest pulley size. The $\tau_{pat}$ constructed here does not have the strict stability of those derived using Algorithm 1, but has many stable gripper configurations and can be further stabilized with surface friction. Model predictions for the net torque at several grip tensions are shown (Fig. 2.17). As the tension in the grip cable increases, links deploy when the net torque at a joint becomes positive. If the tension in the grip cable grows independent from the tension in the retract cable, the net torque will approach the torque profile $(\tau_E)$ of the grip pulley series (Fig. 2.17-B at 16 N). Eventually the quadratic increase in torque required to stabilize the growing grip tension will be too great, however, and can lead to instability.

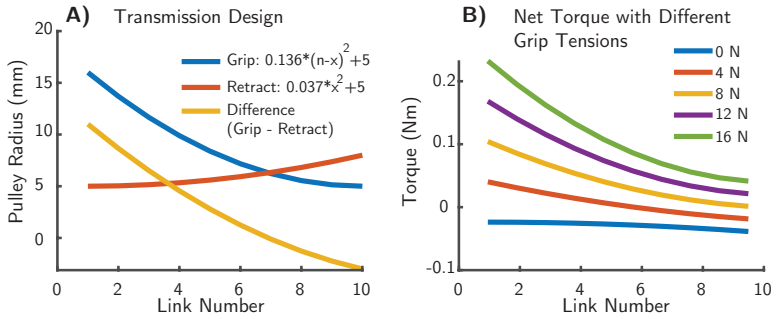



**Figure 2.17**: Plot of pulley sizes and modeled torque at different grip tensions. (A) Each pulley series is a quadratic fit with $n$ links and $x$ as the link number. The two series work antagonistically to generate a net torque at each joint. For sequential actuation the net pulley size at each joint should monotonically decrease from the base to tip of the gripper. (B) The net torque at different grip tensions given a constant retract tension of 5 N. Positive $\tau$ will deploy the gripper and negative $\tau$ will retract the gripper.

### 2.2.3 Results

To reliably conform to arbitrary shapes, each link must actuate sequentially. This was done with two independent transmission mechanisms inside the gripper that provided torque in opposite directions through a set of grip and retract pulleys. Based on the difference in pulley size and the tension in each cable, a link can have a net positive or a net negative torque (Fig. 2.17). To get sequential motion, the difference between the sizes of the pulleys at each link decreases monotonically from base to tip. We measured the required grip tension to actuate each link compared to Equation 2.9 (Fig. 2.18). This experiment was performed three times with an error of less than 2%. While the trend of sequential actuation is clear, the values are off by as much as a factor of 1.65 due to friction. For our mechanism, friction was dominated by the cable sliding against itself, and this depended on both the tension in each cable and the configuration of the linkage. Once deployed, less tension was needed to maintain a gripper configuration due to friction in the transmission.

While highly under-actuated grippers are unlikely to have strict stability, we show two complimentary and model-free approaches to stabilize a configuration (Fig. 2.19) 1) simultaneous scaling of grip and retract tension to increase normal pressure without destabilizing a configuration

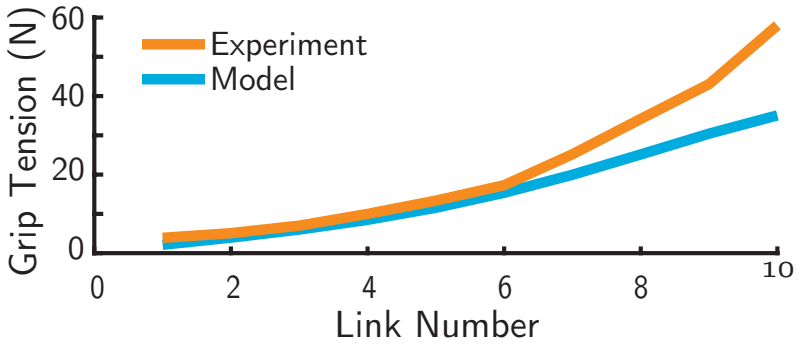



**Figure 2.18**: Tension required to actuate each link in the gripper on a flat surface. As tension in the gripping cable increases, it overcomes the torque provided by the retract cable to deploy each link sequentially.

and 2) high friction interfaces to increase surface friction. To evaluate these methods we tested both high and low friction interfaces at different grip and retract cable tensions. We also compared the observed behavior with model predictions (Fig. 2.19-E). Figure 2.19-A illustrates that this gripper had stable configurations on a flat surface, but the gripper can be destabilized if the grip tension changed independently from the retract tension. Increasing the tension in the grip cable while keeping the retract tension constant changed the torque pattern and led to instability. With a low friction material this instability can freely propagate throughout the linkage (Fig. 2.19-B). As seen in Figure 2.19-C the cable tensions of the stable grasp were both scaled to preserve the stable torque pattern, scale the grip force profile, and increase frictional forces. Scaling cable tensions is effective over a broad range but is not linear because the friction in the transmission mechanism increases with cable tension. For our gripper the effect is small at cable tensions less than 20 N, but will have more impact on the distal links at higher tensions ( Fig. 2.18). Despite this un-modeled friction dependency, the method still scales well since the tension in the grip cable is much higher than the retract cable. The friction in the grip cable will exceed that in the retract cable and prevent the ratio between the grip and retract from growing and introducing instability. In Figure 2.19-C we tested the impact of a load-independent high friction material: a gecko inspired adhesive [58]. The increased friction maintained stability up to a grip tension of 42 N with a low retract tension of 3 N. On a flat surface instability started at the tip and propagated

sequentially to the base as the grip tension increased. As links in an under-actuated gripper destabilize, the normal force tends to concentrate in distal links since together all the links must react the torque from the base joint. Algorithm 2 captured the force concentration at the tip, but does not consider friction and could not predict loss of contact, such as when the gripper spirals into itself (Fig. 2.19-B) or in the case of stabilization through high-friction (Fig. 2.19-D).

These two methods do not depend on prior knowledge or modeling and can be used to stabilize an arbitrary configuration and prevent unstable links from propagating instability to adjacent links. In this case, the unstable links may not push into the surface, but the remaining stable links will maintain the grasp. The methods are also complementary as increasing normal pressure makes the high-friction interfaces more effective, with additional benefit in the case of mechanical interlock or object closure. Using the two methods together is beneficial in all cases, but there are a few additional considerations. On a featureless curve or object too large to enclose, use of gecko-inspired adhesives will have more impact than scaling the tensions due to the angle of the force vector along the surface of the object [46] (Fig. 2.21- Cylinder, Dish). For grasps that rely on mechanical interlocking or targets with rough surfaces, scaling the tension in the cables is particularly effective (Fig. 2.21- Box, Mirror Mount). This scaling is also important for a load-dependent approach to friction (in contrast to the adhesion-controlled friction provided by the gecko-like material).

Measuring the forces into the surface at several links revealed that strict stability was rare, but generally did not prevent the gripper from finding stable configurations and reconfiguring into a stronger grasp if sliding occured. To measure the forces, we installed force sensitive resistors on five links with mounts to ensure each sensor was loaded with a consistent contact area. Though calibrated with known masses, a 15 % error remained due to hysteresis and trial-to-trial inconsistency of the sensors, as per the data sheet.

We tested the gripper on four surfaces and several interesting trends are visible in the data (Fig. 2.20). During deployment, the measured forces never exceeded 0.5 N. Gentle deployment

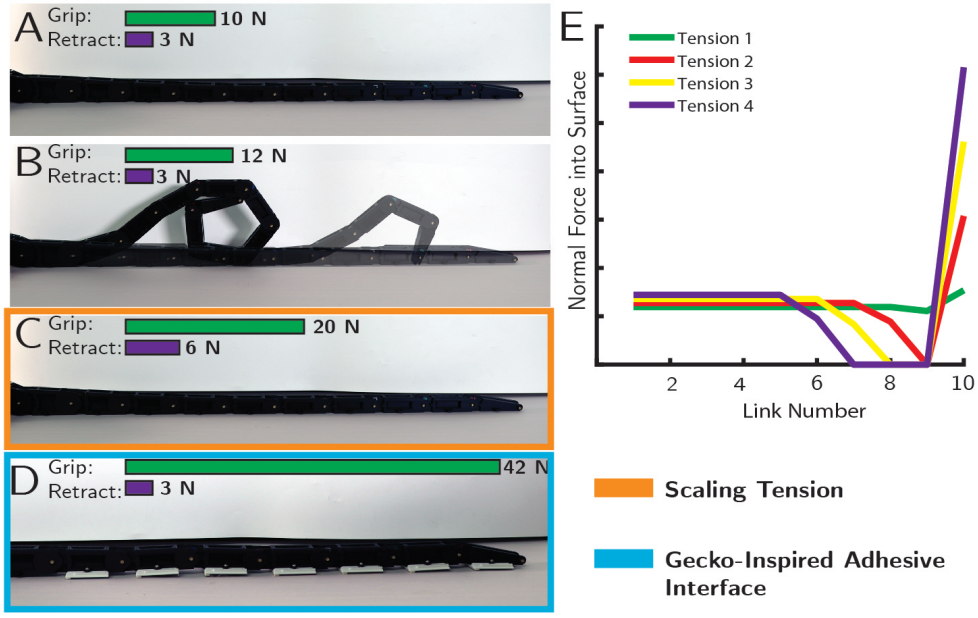



**Figure 2.19**: Gripper modeling and behavior on a flat surface. A) The gripper in a flat configuration can become unstable. B) With increasing grip tension, instability propagates. Two methods can stabilize the configuration C) scaling the tension cables and D) using high friction materials. E) Our model shows that as grip tension increases, successive links are destabilized for this surface geometry.

is an important feature for grasping unconstrained objects since the gripper should not push the object away before it is enclosed. Furthermore, the gripper typically did not exert large localized forces onto the object even at high cable tensions; during the pull test the force in the grip cables peaked at nearly 110 N, but the maximum inward grip force did not exceed 2 N. With a compliant interface capable of distributing contact, this grip force equates to a link pressure of only 1.25 kPa, showing that these grippers are safe for contact with delicate objects. Furthermore, during the pull test (Fig. 2.20 D) the forces at different links actively redistributed, showing how the force distribution adapts as the gripper reconfigures during a task. Lastly, there were only a few instances of all 5 links pushing into the surface simultaneously. This highlights how unlikely strict stability is for a highly under-actuated gripper but also shows that instabilities don't necessarily prevent successful grasping.

In unstructured tasks it is impractical to guarantee strict stability and even force distribution

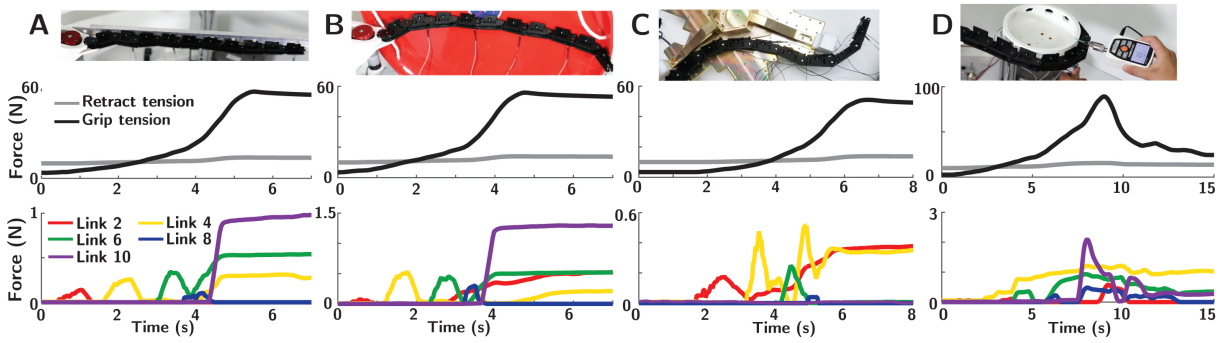



**Figure 2.20**: Force distribution into the surface of different objects: planar (A), concave (B), irregular (C), and a cylinder (D). In the final test (D), a load applied to the object tested the grippers ability to reconfigure. These tests show that having all links pushing into a surface is unlikely -especially for unknown objects. However, instability did not propagate or prevent enclosing these objects.

for highly under-actuated grippers, as they are difficult to achieve and not required to grasp effectively. Grasp success depended on surface properties such as friction, system compliance, and use of adhesives such as magnets and gecko-inspired films. We tested four different interfaces: a gecko-inspired adhesive [58], soft silicone foam, the PLA link without an interface, and magnetic tiles (Fig. 2.21 *top*, from left to right). To further study these effects, we tested these interfaces on four distinct geometries: a cylinder, dish, rectangle, and an irregularly shaped mirror mount (Fig. 2.21 *bottom*, from left to right). Each trial was performed once and further study is needed to quantify consistency. Each trial used a consistent grip and retract tension. A force gauge (Mark 10) measured the maximum pull force the gripper held on each object. The gripper was tested to a maximum of 30 N to avoid damaging the 3D printed linkages.

The best performance resulted from the gecko-inspired adhesive interfaces, which reached the 30 N limit on all surfaces. Previous work with gecko adhesives on curved surfaces provide models for the maximum grip force and dependence on object size [46, 47, 56, 57]. Our gripper performed similarly on curved surfaces with two important differences. 1) The joints in this gripper rotated independently and wrapped more closely around objects with protrusions, improving the adhesive force in arbitrary configurations. 2) The gripper provided normal force into

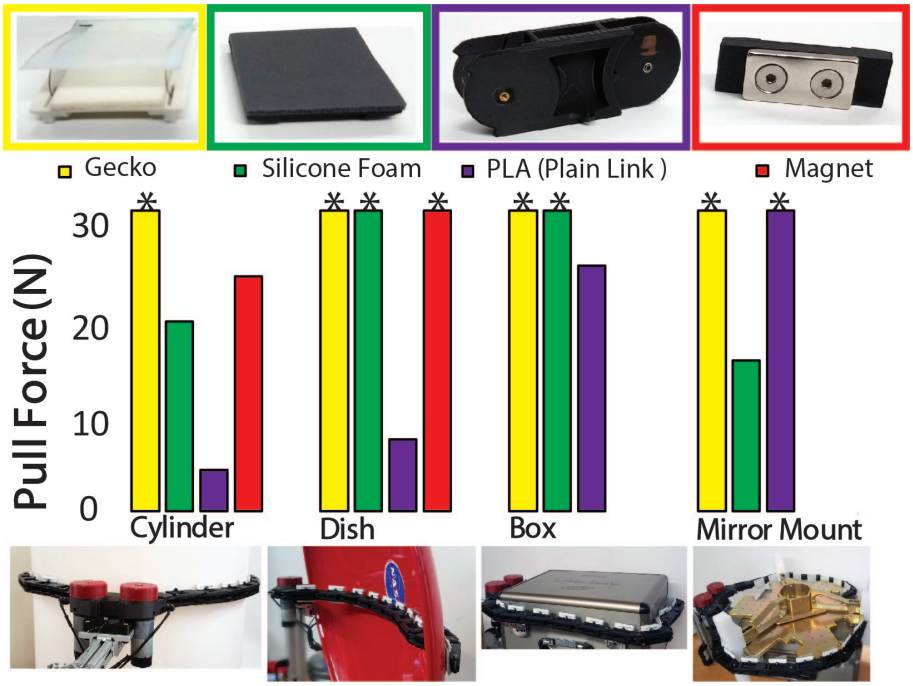



**Figure 2.21**: Maximum grasp strength on different surfaces. Different materials compare the effects of friction, compliance, and adhesion. *These trials were stopped at 30 N to protect the PLA links.

the surface of objects, exploiting mechanical interlocking to allow for grasps that do not depend on the adhesives. The effect of the mechanical interlocking can be seen with the PLA interface, especially on the box and mirror mount.

The magnet provided a normal force attracting each link into the surface of the object, stabilizing the grasp by keeping links in contact with the surface. The increased normal force also increased friction, but is limited because the magnets had a low coefficient of friction. Only the cylinder and the dish were tested with the magnet since the other materials were non-ferrous. The low-friction PLA link performed poorly on the smooth objects. However, on the box and on the mirror mount, the gripper reconfigured and distal links caught a corner of the object, supporting a high pull force. The high-friction foam performed consistently across all trials, but was not as strong as the gecko-inspired adhesive. High friction improved performance across geometries, though the gecko-adhesive and magnet were surface dependent. Unstable links and poor initial

configurations did not limit the utility of the gripper due to stabilization from friction and since the gripper showed an ability to reconfigure into a better grasp.

These tests highlight the ability to increase grasp strength on unknown objects with highly under-actuated grippers as high friction not only helped stabilize a grasp but also improved grip strength. Because these highly under-actuated linkages conform to a target object, the gripper will support large loads simply by preventing shear sliding [46, 47]. Sequential deployment ensures many points of contact between the gripper and target. Initial configuration is not important since the gripper can reconfigure during a task, effectively searching for a stronger grasp if sliding occurs.

### 2.2.4 Discussion

Highly under-actuated grippers offer a unique set of trade-offs. These grippers can deploy to long lengths for grasping large objects while still maintaining conformation to arbitrary shapes and irregular surface features. These grippers perform best when wrapped around an object, and struggle with pinch grasps and in-hand manipulation. Mechanical complexity of the system is high relative to parallel jaw grippers or grippers made from soft elastomers. These trade-offs determine the tasks for which these grippers should be used. There are also several unique properties seen in highly under-actuated systems. Highly under-actuated grippers can conform to concave surfaces through the process of sequential deployment (Fig. 2.21 - Dish). These grippers can be used on or near humans with relative safety because they grasp with low, distributed, pressure (Fig. 2.22-A). These grippers can even follow along a non-continuous path (Fig. 2.22-B). Finally, using dynamic actuation or a pair of linkages, these grippers can capture non-adjacent objects (Fig. 2.22-C).

Highly under-actuated linkages blur distinctions between grippers comprised of low-DOF linkages and soft continuums. There are lessons and designs from these technologies that can flow in both directions. Braking elements are capable of improving grip forces of under-actuated

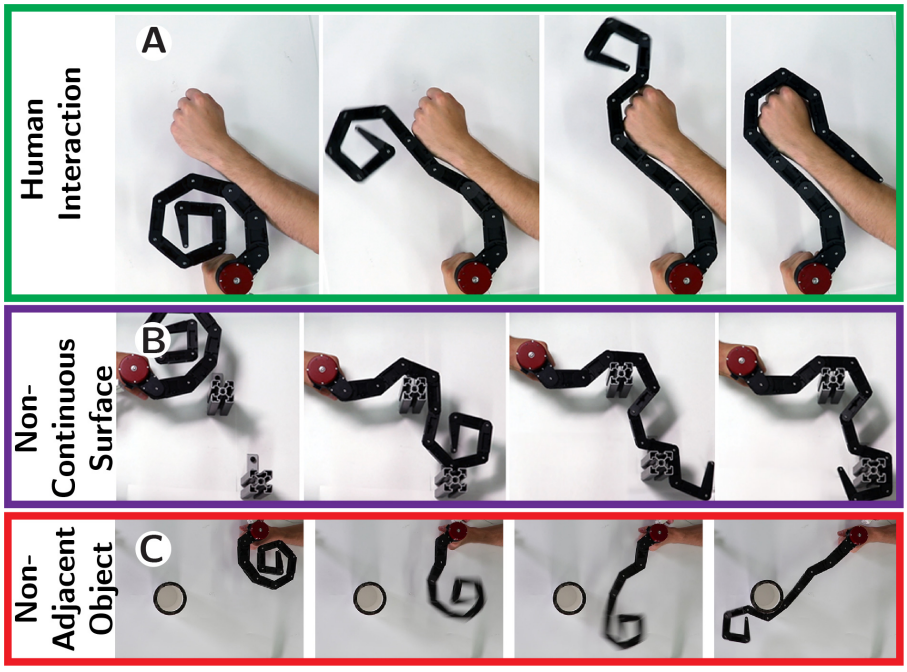



**Figure 2.22**: Demonstrations of unique capabilities: interacting with humans safely (A), deploying along a non-continuous surface (B), and capturing non-adjacent objects (C).

grippers [53]. Compact variable stiffness devices such as the use of low-melting point alloys or layer jamming may be integrated with highly under-actuated linkages [55]. Additionally, some pneumatic transmission mechanisms have a torque that scales cubically which scales well to smaller systems or to the use of many joints [47, 59]. Both linkages and soft material grippers share the issue of stability [47, 59]. Frictionless models of under-actuated grippers suggest that instability should become more problematic with increasing DOF. However, soft grippers are often made of high-friction materials and the wide range of successful soft grippers refute this point in practice [54, 55]. In this letter we show that friction has a dramatic effect on system stability and grasp strength of highly under-actuated grippers. Optimization techniques from under-actuated linkages [59] could offer benefits to the performance of soft material grippers. However, further optimization efforts are needed to account for friction and the high dimension configuration space. Sequential motion, which aids conformation to arbitrary shapes, is rarely found in elastomeric grippers since the retract force in most elastomer grippers depends on the

gripper configuration. There are likely designs that can satisfy sequential motion for soft material grippers. Eversion robots are an interesting class of compliant transmission that exhibit sequential motion and deployment, but have not yet been used to grasp [60, 61].

In this letter, we present a gripper designed to robustly grasp across a wide range of large and irregular surfaces without modeling the interaction. Under-actuated systems offer unique benefits for our targeted application of in space satellite servicing. They allow for both capture of large objects and improved shape conformation; reducing the importance of positioning and control. We find that friction can dramatically improve the grasp strength and probability of stability in a given configuration. Though we focus on a low-force application, we show there are many pathways to broader relevance for highly under-actuated grippers. A range of adhesives such as magnets, gecko-inspired films, suction cups, or micro-spines can increase strength and improve stability. Grasp strength can also be increased through the use of brakes or variable stiffness devices at the joints. Finally, the ability to deploy around an object might be valuable beyond gripping; examples include sensing shape or stiffness, deploying a payload, and bypassing visual occlusions [62].

## 2.3 Acknowledgements

This work was carried out at the University of California, San Diego, and at the Jet Propulsion Laboratory, California Institute of Technology, under contract with the National Aeronautics and Space Administration, and sponsored by the U.S. Government. P.E. Glick Is supported by a NASA Space Technology Research Fellowship.

Chapter 2, in part, is a reprint of the material as it appears in IEEE Robotics and Automation Letters 2018. Glick, Paul E.; Suresh, Srinivasan A.; Ruffatto III, Donald; Cutkosky, Mark; Tolley, Michael T.; Parness, Aaron. The dissertation author was the primary investigator and author of this paper.

Chapter 2, in part, is a reprint of the material abbreviated from IEEE International Conference on Robotics and Automation 2020. Glick, Paul E.; Van Crey, Nikko; Tolley, Michael T.; Ruffatto III, Donald. The dissertation author was the co-primary investigator and author of this paper.

# Chapter 3

# Growth as a Method to Navigate Unexplored Passageways

## 3.1 Eversion and retraction of a soft robot towards the exploration of coral reefs

Coral reefs are among the most biodiverse ecosystems in the world. Occupying less than 1% of the sea floor, coral reefs are home to more than 25% of all marine life [63] [64]. However, the true biodiversity of the reef remains largely a mystery because current technology has limited the study of coral reefs primarily to their outer surfaces [64]. Filling the key knowledge gaps of the internal reef environment has become imperative as anthropogenic threats to the ocean, such as climate change and overfishing, drive the disappearance of healthy reefs worldwide [65]. Coral reefs are massive, three-dimensional structures with many tunnels and crevices that comprise the habitats of the reef matrix. These tunnels and crevices are estimated to be 30-75% of the reef habitat [66] and are thought to be critical for maintaining biological, ecological, and chemical processes [67] [68] [69]. However, the majority of reef species and the properties of coral habitats remain unexplored because of the difficulty of accessing internal reef structures non-

destructively. Current knowledge of life in these cryptic habitats is based primarily on destructive sampling [64] [70] [71]. Aside from issues with destructive sampling to reef health, the limitation of this method is the inability to provide in situ data on organismal ecology or biology.



**Figure 3.1**: The natural crevices and passageways of the diverse coral reef structure present a challenge for accessing the internal structures non-destructively (Above, *Reef photo: M. Johnson*). The soft body of an eversion robot can provide the compliance to traverse through the intricate reef matrix and explore its ecology (Below).

The challenges of accessing delicate internal reef structures are due to factors including small and unpredictable spaces, rough surfaces, variable crevice diameters, irregular geometry, lack of light, difficulty of transmitting data underwater, and lack of prior knowledge on paths through reef cavities. Existing options to explore the reef matrix in situ are limited to either robotic instruments [72] or handheld endoscopic probes [73] [74]. The Cave Cam, an endoscopic video camera with limited ability to penetrate the reef, was the primary attempt to construct such a probe. Controlling a probe is sufficiently challenging in low visibility, underwater habitats such that capturing useful data cannot be guaranteed. Together, these challenges motivate the need for a robotic system that can traverse the extreme spatial environment of the coral reef matrix.

Accessing these reef habitats would allow biologists to document the behavioral and ecological characteristics of cryptic organisms and sample their abiotic environment.

Many of the robots designed to climb or swim through tortuous pathways are not well suited for the particular challenges of a coral reef. Robots that locomote with inchworm-inspired motion rely on external contacts to brace themselves, but in a coral reef such contacts are available only intermittently [75] [76]. Swimming robots are capable of navigating 3D space, but due to the size and communication constraints in the reef, these robots would need to be tethered to provide power and data transmission [77] [45]. Any tether provides a significant constraint due to the high friction of dragging a cable through convoluted paths [78]. However, the emerging technology of eversion robots presents a compelling solution to this technical challenge. Eversion robots are a type of growing robot, characterized by their unique method of tip extension. Inspired by the biological process of growth, eversion robots are pressure-driven to deploy new material at their tip and lengthen their body [60] [79] [80] [81] [82].

Eversion robots are well suited to operate in small passageways and in delicate environments due to their intrinsic compliance to conform to existing pathways (Fig. 3.2) [1] [47] [83]. Since these robots deploy material at the tip, there is no relative motion between the exterior of the robot body and its environment [60]. These growing robots are unencumbered by friction as the base of the robot body is static rather than sliding along a surface.

Previous work has demonstrated the promise of eversion robots. Blumenschein et al. described the parameters that define the constraints on eversion [78]. Multiple studies have evaluated methods for position control of these soft robots and the maximum loads they can support [78] [79] [84]. However, retraction of an eversion robot has yet to be rigorously characterized. The deployed strength of these robots is greatly impacted by contacts with boundary constraints. Furthermore, eversion robots have proven to be well suited for operation in air, but have yet to be fully demonstrated in liquid environments (e.g. pipes, oceans).The main contributions of our work are the design, implementation, characterization, and modeling of a water-pressurized

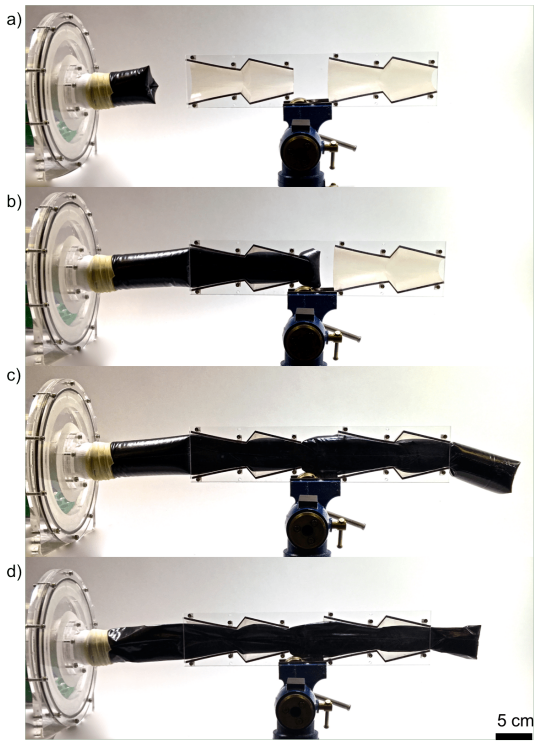



**Figure 3.2**: The robot can evert through varied passageways. This property makes these soft robots apt for operation in the highly variable coral reef matrix. (a) Robot at initial state before eversion. (b) Eversion through a constricting passageway. (c) Eversion proceeds through both passageways and free space. (d) The robot can enter a depressurized state to avoid blocking external flows or to conserve electrical power.

eversion robot.

### 3.1.1 Design and Fabrication of the Underwater Eversion Robot

The three main components in the design of this eversion robot are: a mechanical drivetrain, a rigid pressure chamber, and a soft body made of flexible fabric (Fig. 3.3). These components provide the necessary torque, pressure, and material for the growth mechanism. Additional design features allow for data collection and operation underwater.

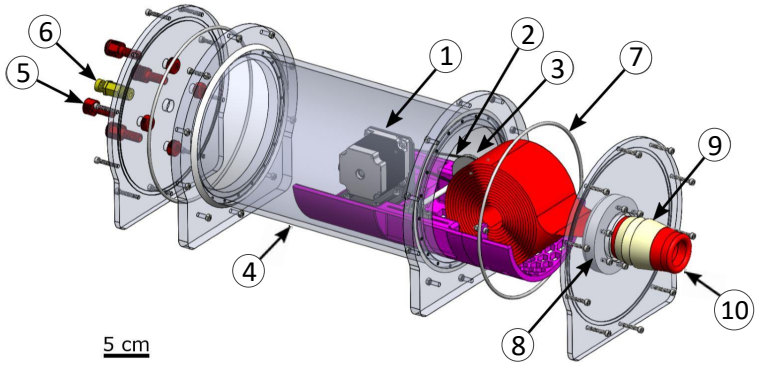



**Figure 3.3**: Exploded 3D model of the robot system. Mechanical drivetrain: (1) stepper motor, (2) timing belt, (3) pulley gear. Pressure chamber: (4) pressure chamber housing, (5) bolt penetrators, (6) pressure relief valve, (7) O-ring coated with grease, (8) bolted pressure seal adapter, (9) latex clamp. Soft robot body: (10) nylon fabric membrane.

### Mechanical Drivetrain

The mechanical drivetrain applies a torque to control the rates of extension and retraction during deployment of the system. A stepper motor, located inside a cylindrical pressure chamber, winches the spooled fabric body. The motor provides torque to counteract the pressure acting on the soft robot body and either spools or unspools the fabric. The radius of the spool with the wrapped fabric changes as the robot grows, which affects the torque output from the drivetrain. The use of a stepper motor eliminates the need for a feedback mechanism to command the robot to a particular position. If the robot is depressurized and in a passageway, there is no tension along the fabric body and the robot will hold its position due to the passageway (Fig. 3.2). In this case, the power to the motor can be disconnected to save power on long duration deployments.

### Pressure Chamber

The pressure chamber provides internal pressure to drive the inflation and growth of the fabric body (Fig. 3.3). This rigid pressure chamber houses all the components and connections. The rigid frame of the pressure chamber provides a secure mount for the drivetrain, electrical

feedthroughs for the motor, and fluid connections used for the pump and pressure relief valve. At the front of the pressure chamber is a flange for the everted fabric body to be clamped against. The back plate contains bolt penetrators to connect to an external pump that supplies the fluid pressure and a relief valve for self-regulation of the internal chamber pressure. Acrylic and 3D printed components allow for optical transparency and rapid prototyping, but should be replaced with corrosion-resistant metal parts for long-term field implementation.

**Soft Robot Body**

The fabric body provides the new material at the tip for the eversion mechanism. The body of the robot is a soft membrane comprised of two layers of soft fabric sewn together. We used a silicone-coated ripstop nylon (Ripstop Nylon, Seattle Fabrics) for the membrane material and a silicone adhesive (Silnet Seam Sealer, Gear Aid) to seal the seams. This fabric body connects to a 3D printed flange on the front plate of the pressure chamber to create a pressure-tight seal.

**Data Collection Payload**

Eversion robots can support payloads to collect scientific data, such as a camera or water-sampling device. Prior eversion robots typically use tethers to support payloads [60]. We implement a new untethered payload mechanism at the tip using ring magnets (Fig 3.4). This tip device is comprised of two parts, one inside and one outside of the fabric body. The inside piece is a torus with the fabric inserted through the center hole which keeps the mechanism centered as the robot grows. If the payload gets caught in a pathway, the robot can easily disconnect from the device and continue to evert or retract. This feature is important to avoid damaging the reef and can even be used specifically to deploy a payload inside the reef. We mounted a miniature waterproof camera onto this magnetic device at the tip to record video data as the robot grows.

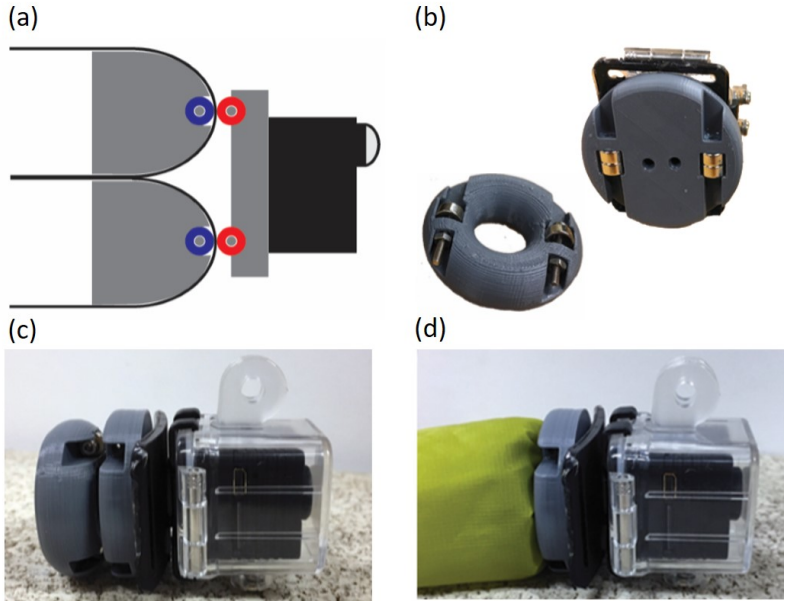



**Figure 3.4**: Payload mechanism for the eversion robot. (a) A cross section of the magnetic mechanism to support a payload at the robot tip. (b) Using a torus inside the robot keeps the mechanism constrained along the axis of growth. Free-spinning ring magnets allow the fabric to slide between the inner and outer parts. (c-d) The rigid plate can support payloads, such as a small camera, with the soft fabric body inserted through the torus.

### Underwater Operation

Eversion robots are well suited to operating underwater, but this requires design and operational modifications. These robots use pressure to drive growth, and so must be designed as pressure-tight systems. With the exception of the pressure pump, most pneumatic-driven eversion robots are already waterproof without modification. However, using air to drive growth in a liquid medium will lead to large buoyancy forces acting along the body of the robot. Ideally, the fluid used to drive growth should have the same density as the fluid in the surrounding medium. For our application, we used surrounding water to make the robot neutrally buoyant and we generate pressure for growth using a submersible pump.

However, the use of seawater inside the robot necessitates design changes to address three resulting challenges. 1) Liquids are generally incompressible, which complicates the process of growth and retraction. 2) Electronics must be insulated from seawater, which is both conductive

and corrosive. 3) All components, both inside and outside of the robot, need to withstand the marine environment.

Eversion using a liquid-filled robot is slower than with air since the working fluid is incompressible and cannot expand to fill the increasing volume of the robot. The rate of growth is limited by the flow rate of the pump and the increased viscosity of the fluid. Retraction is also affected when using a liquid-filled robot because when the volume in the soft body decreases, the pressure in the chamber will increase significantly. Since water pumps provide only positive pressure, removing water from inside the robot to maintain a desired internal pressure presents a challenge for fluid control. We used a nylon pressure relief valve to enable retraction. Pressure relief valves open only when the pressure increases above the set-point threshold. This simple change allows the robot to retract successfully even when filled with incompressible fluid.

With seawater inside of the robot, electrical components need to be protected. The conductivity of water does not short-circuit brushless motors (including stepper motors), but seawater can lead to undesirable corrosion and electrolysis. Commercially available stepper motors that are waterproof can be costly and limited in submersible depth and operation time. To prevent motor corrosion, we fabricated a pressure-tight housing for the motor with a rotary shaft seal. This 3D-printed housing has a soft diaphragm and is oil-filled to equalize pressure between the inside and outside of this housing. The oil is incompressible, electrically insulating, inert, and acts as a heat sink.

Finally, all components need to withstand the challenges of the marine environment, particularly corrosion, temperature fluctuations, biofouling, and hydrostatic stress. Passive mechanical components should be made of corrosion-resistant, temperature stable, and incompressible materials. For this prototype, we used several materials (acrylic, 3D printed plastics) that are not suitable for long-duration or deep-sea applications. However, the depth of operation does not require significant modifications to the overall design of the robot other than material changes. Because each sealed area of the robot is filled with incompressible fluid and connected via soft

membranes, the pressure differences (between the ambient water, interior of the robot, and motor housing) are on the order of several kilopascal, regardless of the depth of the robot (Fig 3.5). As such, the most significant forces on the robot will be hydrostatic stresses due to depth. As long as the material of each component of the robot can withstand the hydrostatic stress associated with a particular depth, the actual depth of the robot does not necessitate change to the overall design or operation.

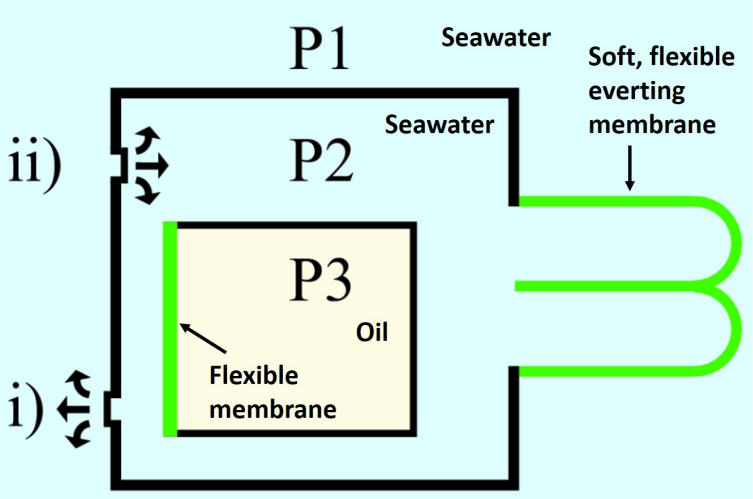



**Figure 3.5**: The pressure differentials between each chamber in the robot remain low, regardless of the ambient pressure (P1). A pump (ii) and pressure relief valve (i) regulate the internal chamber pressure P2 to be slightly higher than P1. The oil-filled motor housing has a flexible membrane, which maintains a minimal difference between its pressure P3 and P2.

### 3.1.2 Modeling the Eversion Robot

#### Loading on the Robot

We describe models for the loading conditions with eversion robots. Load bearing capability in free space has been well modeled for inflatable beams and eversion robots pressurized by air [78] [79] [85] [86]. We briefly review these results for both the case of axial and radial loading cases. Axial buckling describes the maximum compressive force an inflatable beam can

withstand before failure [85]:

$$F_{cr} = \frac{EI\frac{\pi^2}{L^2}(B + G\pi rt)}{EI\frac{\pi^2}{L^2} + B + G\pi rt}, \tag{3.1}$$

where $r$ is the radius of the everted tube, $E$ is Young's modulus, $I$ is the area moment of inertia for a cylindrical shell, $L$ is the length of the beam, $B$ is the axial force due to internal fluid pressure $P$, $G$ is the shear modulus, and $t$ is the cylindrical wall thickness.

The maximum radial load for an eversion robot in free space is also well described by inflatable beam theory [79] [84] [87] [88]. Failure under transverse load occurs by wrinkle propagation and bending of the beam. The maximum radial force of an inflatable beam is described by Eq. 3.2 and the moment by Eq. 3.3 [88].

$$F_{radial} = \frac{\pi pr^3}{L} \tag{3.2}$$

$$M_{bending} = \pi pr^3 \tag{3.3}$$

However, these models for critical loads need to account for external contacts along the length of the soft membrane in a constriction or along a passageway. These boundary constraints provide mechanical reinforcement to the robot that can drastically impact the maximum loads of the robot. We demonstrate how these models can be extended for behavior with constrictions in the Results section.

**Effect of friction during retraction**

Friction occurs between the inside and outside of the soft membrane body in a bend and is an important parameter for modeling eversion and retraction in a constrained environment (Fig. 3.6). Modeling this friction establishes mechanical requirements for the drivetrain of an eversion robot given a coefficient of friction, pressure in the robot, and particular path. These models help describe the maximum forces that eversion robots can exert on their path, which is relevant for

guaranteeing non-destructive exploration of sensitive coral. While the tension required to initiate retraction at the tip of the robot may be readily found, the matter is complicated by friction, which is dependent on the path of the robot. The magnitude of axial force exerted by the internal pressure is simply the pressure times the cross-sectional area. Under static conditions a force balance yields Eq. 3.4.

$$T_i + T_o = PA \tag{3.4}$$

To initiate retraction we must exert a tension at the tip $T_i > \frac{PA}{2}$. However, based on Euler's formula for belt friction, the drivetrain of the winch motor must apply a force [89]:

$$F_{drivetrain} = (\frac{PA}{2})e^{\gamma\mu}, \tag{3.5}$$

where $\mu$ is the coefficient of friction of the tube material against itself, and $\gamma$ is the total contact bend angle across the everted length. As illustrated in Fig. 3.6b, the bend angle depends on each contact along the robot's path in the environment. In this way, the force required to guarantee retraction may be found. For a spooled membrane, the torque supplied by the drivetrain depends on how much spooled material remains as this affects the gear ratio [79]. While the retraction force increases exponentially as a function of the total bend angle, the pressure in the robot may be lowered and the tube material may be lubricated with low-friction coating to ease the process.

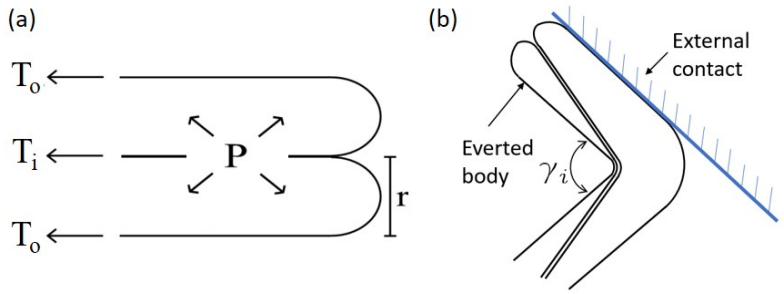



**Figure 3.6**: Free body diagram of the eversion robot. (a) Cross-sectional side view of the free body diagram of the tip of the robot. $P$ describes the internal pressure and $T_i$ and $T_o$ are the inner and outer tensional force acting on the material. (b) The sum of all individual $\gamma_i$ is the total bend angle of the everted body for all external contacts in the robot's path.

**Retraction Forces on the Environment**

While it may be possible to guarantee retraction with a sufficiently powerful drivetrain, we present two models to evaluate the force of an eversion robot on its environment during the retraction process. We seek to model the pressure that the robot exerts on the objects with which it comes in contact, and model the reaction forces on an environment that arise from the tension in the robot. While Eq. 3.5 evaluates the robot path as a whole, these models instead concern each individual bend within the robot path. For this reason we generalize the tension on each side of a bend to be $T_1$ and $T_2$, defined such that $T_1 < T_2$ (i.e. friction is acting to resist motion towards $T_2$), the angle of a particular bend as $\gamma_i$, $r$ as the radius of the soft robot body, and $C$ as the radius of curvature of the bend. Eq. 3.6 describes the maximum contact pressure $\rho_0$ across a bend angle $\gamma_i$ [89].

$$\rho_0 = \frac{T_1}{2rC} \tag{3.6}$$

The magnitude of the reaction force on a bend may be found with

$$F_{reaction} = \sqrt{T_1^2 + T_2(\gamma_i)^2 - T_1 T_2(\gamma_i) cos(\gamma_i)} \tag{3.7}$$

where $T_2(\gamma_i)$ is defined by Euler [90]:

$$T_2(\gamma_i) = T_1 e^{\mu r \gamma_i} \tag{3.8}$$

Using these equations with knowledge of the path of the robot, it is possible to fully describe the reaction forces and local pressures on the environment through which the robot has everted. With enough fluid pressure and motor torque, the robot may evert long distances through winding passageways. These equations provide further tools to model the forces from eversion and retraction on the pathway itself.

### 3.1.3 Results

#### Axial Loading

The maximum axial force is dependent upon the pressure applied. Thus we varied the pressure inside the robot and held the beam at a constant length of 30 cm, applying an increasing load axially until failure occurred both in free space and in a cylindrical constriction with a radius smaller than the body of the robot (Fig. 3.7). To measure the axial load, we recorded the force required to deflect the tip 3 mm, which was determined as the failure point across varied pressures. Measurements were taken with a force gauge (Mark 10 M3-20), and each data point represents the average of five trials (Fig. 3.8). We evaluated the model using two different radii for the soft body. Radii A and B were 1.6 cm and 2.4 cm, respectively. To generate the model, we used $G = 0.742MPa$, determined experimentally. The membrane material was nylon taffeta with 0.16 mm thickness.

Fig. 3.8 shows that the experimental data when the robot is in free space is well approximated by the model and agrees with prior results [79]. However, the failure mode of the robot depends on the effective length. Shorter beams tend to fail due to crushing rather than buckling. With a short enough effective length (i.e. in a constriction), the failure mode of eversion robots shifts from buckling to crushing. Constrictions serve to shorten the effective length of the robot and thereby change the failure mode and increase the maximum axial force (Fig. 3.8). Because the outer membrane is flexible, failure is not catastrophic and is reversible once the load is removed.

#### Radial Loading

We experimentally validated that Eq. 3.3 describes the maximum bending moment in an eversion robot. Importantly, passageways provide a mechanical reinforcement that effectively shortens the moment arm. To collect the data, we deployed the robot with a radius of 2.4 cm

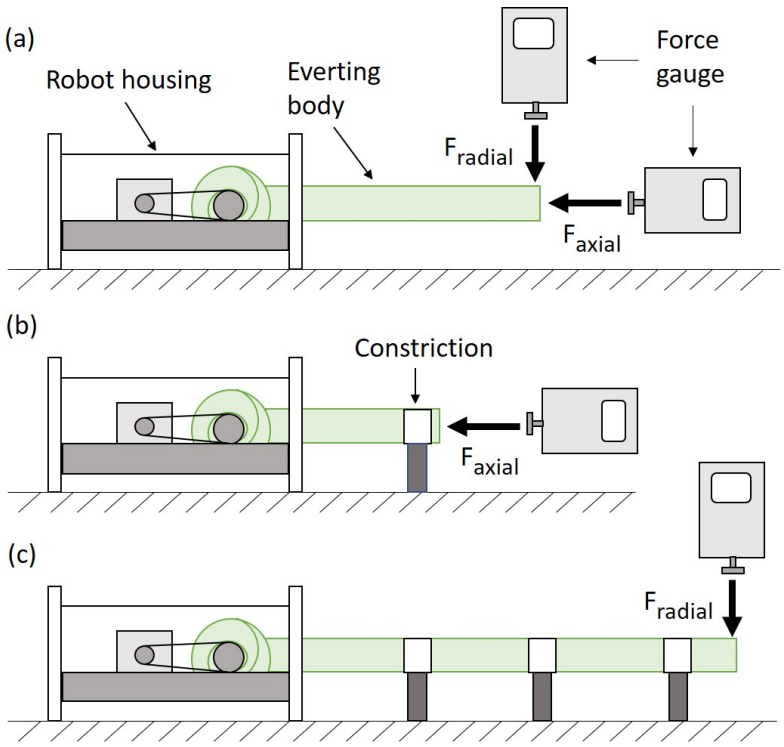



**Figure 3.7**: Experimental setup for measuring maximum loads of the everted soft body. Axial and radial loads were measured in (a) free space and (b-c) with constrictions. Measurements were performed using a force gauge and applying a force in the axial and radial directions as shown until failure occurred.

operating at $10kPa$ and measured radial load at periodic lengths up to 0.8 m. Measurements were taken with a force gauge (Mark 10 M3-20), and each data point represents the average of five trials. We then measured the radial force as we deployed the robot through a series of constrictions positioned along the length of the beam (Fig. 3.7c).

In comparison with radial load measurements in free space, we observed that the constrictions effectively reset the length of the beam. A result of Eq. 3.2 is that the maximum radial load before failure does not depend on the overall length of the robot, but instead depends on the moment arm of the applied load. The moment arm of a load applied radially at the tip of the robot may be taken as the total everted length since the contact with the last constriction. We model this behavior and show these results in Fig. 3.8.

Equations 5, 6, and 7 help quantify both the impact of the robot on its environment and

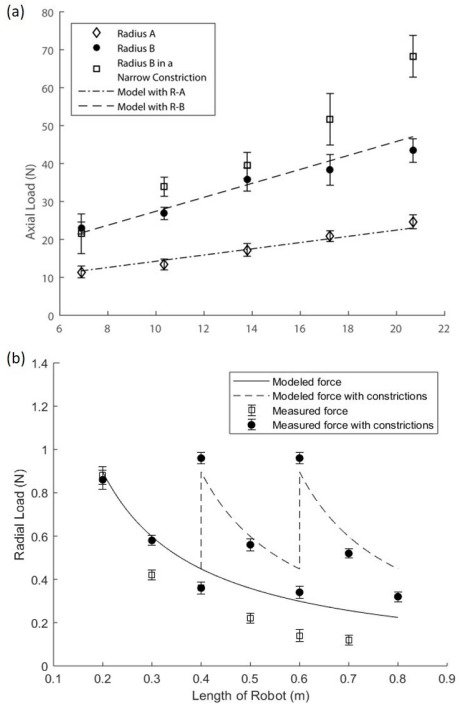



**Figure 3.8**: Radial loading of the everted soft body. (a) Relationship between internal pressure and axial load at failure. The passageway acts as an boundary constraint, shortens the effective length of the robot, and increases its axial load. (b) Maximum radial force depending on the everted length of robot body. When the robot passes through periodic constrictions, the effective moment arm of the load is shortened.

design requirements of the robot. Pressure may be reduced to ease retraction, but there is a minimum pressure beneath which the everted membrane loses shape. By selecting a material with a low coefficient of friction (polyurethane coated nylon), retraction becomes much easier. We found that the robot at an internal pressure of $40kPa$ with a bend angle of $\frac{pi}{2}$ radians exceeded the maximum force achievable with the drivetrain. By decreasing the internal pressure to $15kPa$, the robot was able to successfully retract.

### Underwater Demonstration

To demonstrate eversion underwater, we implemented waterproof components and applied a constant pressure with a small submersible pump. We pressurized the internal chamber with surrounding water to drive the robot. Excess fluid pressure within the vessel was released through

the relief valve outlet, with a set pressure of $20kPa$, to maintain constant internal pressure. Additionally, a miniature waterproof camera was attached at the robot tip with a magnetic payload adapter. With neutral buoyancy, the eversion robot may deploy large lengths of unsupported material without buckling due to its own weight, a behavior that is more challenging in air. Using water as the working fluid, the robot everted at a rate of 1 cm/s. As compared to air, the growth rate was decreased due to the incompressiblity of water and the limited flowrate of our pump.

In this demonstration, we conducted several qualitative experiments. We showed successful eversion and retraction underwater and through constrictions simulating a coral reef environment (see supplementary video). We also presented the capability for underwater data collection with a camera mounted at the tip (Figure 3.9).

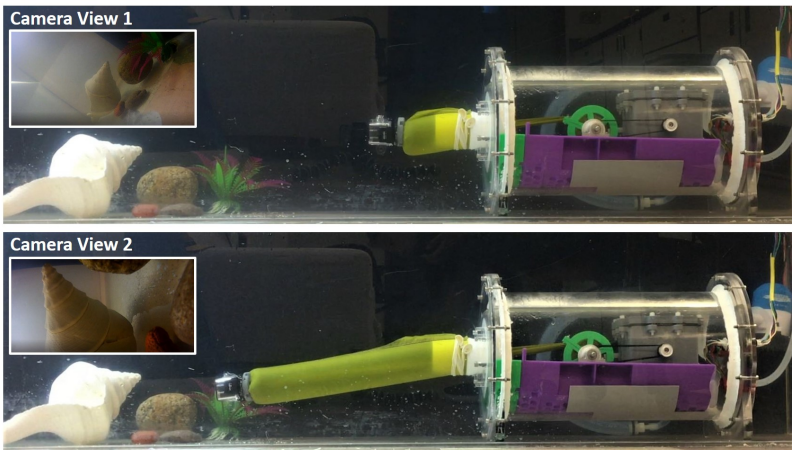



**Figure 3.9**: Demonstration of eversion underwater. The main chamber of the robot was flooded with water and pressurized to drive the eversion process. Using water instead of gas creates a neutrally buoyant robot. An untethered camera attached at the tip allows for data collection as the robot moves along a path. Images 1 and 2 capture the side view of the robot and the camera's point-of-view in the initial (top) and final (below) positions as the robot everts towards an object.

## 3.2 Branching Vine Robots for Unmapped Environments

Robotic exploration of unfamiliar environments is a fundamental problem with many unique instantiations. Exploration of unfamiliar environments is made more difficult when the

terrain impedes the use of traditional wheeled, legged, or flying robots. Relevant examples include collapsed buildings for search-and-rescue applications [91], coral reef cavities for ecological monitoring [61], cave networks for mining or rescue tasks [92, 93], shipwrecks for archaeological surveys [94], and the human body during medical interventions [95, 96]. Despite the importance of the exploration of—and navigation in—unmapped passageways, and the many practical applications motivating the field of research, many of these environments are characterized by tight spaces, precluding the use of onboard energy storage and motivating tethered designs. Challenges of data transmission over long lengths and through certain mediums further push systems towards the use of tethers [97]. However, tethers limit mobility and can generate significant friction due to the capstan effect [78]. Tethers can significantly limit the exploration of confined spaces since the force from this friction grows exponentially with the total change in angle along the tether (which, in general, is a function of the geometric complexity of the environment). Another challenge of navigating these environments is the non-planar nature of many of the spaces. Wheeled or legged robots that are constrained by gravity may face impassable obstacles [98]. Flight offers a potential solution, but is energy intensive and generally only works in relatively large spaces [99]. Finally, the exploration of these constrained and unmapped environments often leads to physical interactions between the robot and the environment that can result in damage to the robot, the environment, or both.

Recently, there has been great interest in soft growing robots that present a potential solution to this area of applications, addressing each of the challenges that complicate the exploration of these environments [100]. Growth in robotics has been realized most notably through the pressure driven eversion of flexible tubes (called *vine robots* or *eversion robots*) [60], extension of concentric tubes [101], or the additive extrusion of a thermoplastic [102]. By growing the robot at the distal tip, these growth processes remove the relative motion between the robot body and environment, which can greatly reduce friction [60]. With reduced friction, it may be possible for these robots to penetrate further into confined spaces enabling the ability to deploy

long lengths without concerns regarding power and data transmission, although this capability is yet to be proven. Another key advantage of growing robots is the self-supporting nature of their deployed structures [103, 104]. Since the grown structure supports new material deployed at the tip of the robot, the new growth can be directed freely in 3-D space. This 3-D mobility gives growing robots the ability to follow complex pathways and avoid obstacles. Finally, soft growing robots are not hindered and are even aided by rich interactions with the environment [105]. Structural compliance seen in soft robots allows for adaptation to irregular features that would otherwise hinder rigid systems. Due to their compliance, both the robot and environment are unlikely to be harmed by interaction [83, 106]. Furthermore, these environmental interactions are helpful for soft growing robots, aiding with navigation [105], and helping to support the deployed structure and increase payload capacity [61]. By contrast, most mobile robots must conduct path planning to carefully avoid obstacles. A direct analog can be found in nature with root and vine structures that would not be self-supporting without external reinforcement (see Fig. 2.13). A soft growing robot may navigate more precisely [105], support larger payloads [61], and reach a larger workspace [107] through rich interaction with its environment. For these reasons, pressure-driven soft growing robots hold great promise for the exploration of narrow and complex passageways. However, this promise is not yet realized for passageways that have not previously been mapped.

Due to the challenge of supporting a large payload with a soft growing structure, approaches for steering eversion robots have bifurcated into: active steering [102, 108, 109] and obstacle-aided navigation [61,105,110]. Active steering approaches face challenges in unexplored spaces due to the spatial constraints of the environment and the difficulty associated with carrying mass at the tip of the robot for sensors or actuators. Vine robots may be gentle enough to adapt to their environment without risk of damage, but the trade-off for this compliance is a limited ability to support payloads. The maximum payload that these robots can support depends on the length deployed, getting smaller as the robot grows [61]. Additionally, in small spaces, a bulky payload at the tip can limit mobility and restrict the robot to only growing through orifices

larger than the payload diameter [111]. For these reasons, everting robots are most capable when unencumbered by payloads at the tip [60]. This behavior drives designs towards smaller and simpler payloads which conflicts with the sensing and actuation hardware required to map and navigate unknown environments. A solution may be found through open-loop growth, reliant on a rich use of obstacle-interactions to help guide the robot. Instead of active steering, designers can leverage the compliance of vine robots to conform to preexisting paths in the environment. The promise of this approach is compelling, allowing the robot to deploy without much mass its tip. For environments that have been mapped in advance, this obstacle-aided navigation can be used to reach a desired location reliably and easily without any active control [105]. However, in the absence of prior knowledge of the environment, a straight robot body is limited by the condensation of many robot paths into a single vertex of an obstacle, as explained by Greer et. al. [105]. This phenomenon of trajectory condensation means that open-loop growth requires some predefined bends or structure in the robot to improve the reachability in the workspace. Yet specific placement of these bends requires prior knowledge, precluding the use of this approach in unmapped spaces. Researchers are developing planning and control algorithms using a hybrid of both obstacle-interactions and active steering [112,113], but this does not address the fundamental limitations of each in a confined and unexplored space.

To realize the potential of vine robots for unmapped spaces, we propose the use of branching vine robots. Here we present a customizable framework for optimizing the design of branching structures for unmapped spaces. To accomplish this goal, we leveraged a set of known maps from a target environment, and simulated the deployment of branching structures on those known maps. We paired application-specific reward heuristics with population-based optimization methods to find high-performing designs to evaluate on unseen maps from the same training environment. In addition we tested our results on hardware, developing a manufacturing approach to realize simulated designs. We found that using optimized branching robots can successfully navigate unmapped spaces, overcoming the trajectory condensation issue that limits

non-branched (single-path) vine robots in unmapped spaces. Our branching designs replicated three properties found in nature: anchoring, coverage, and reachability. Branching designs were able to reach over 25% more of a given environment compared to non-branching structures. We used both anchoring and sensor-coverage as two different example tasks for our optimization process, and tested the optimized designs in hardware. Branching vine robots showed promise for deploying into and attaching to cluttered spaces, evidenced by our system which held 5.65 N with a mass of only 5 grams.

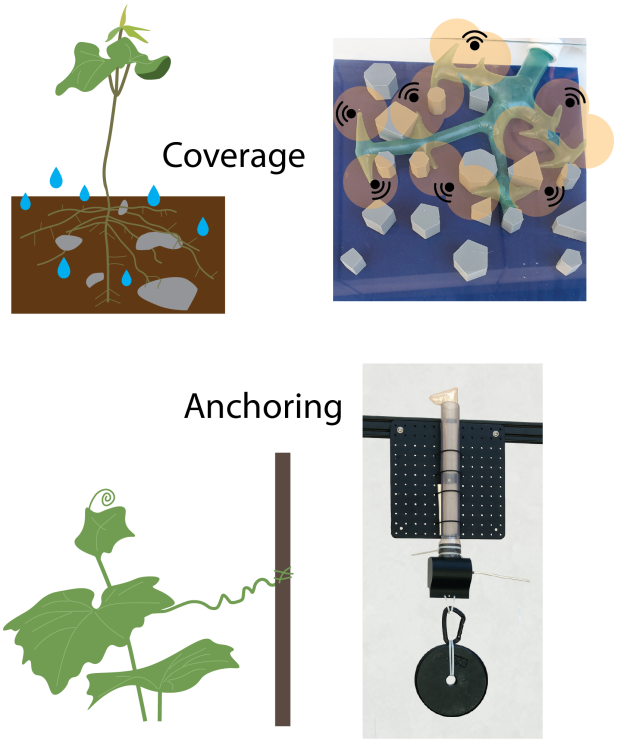



**Figure 3.10**: Branching vine robots for navigating unexplored spaces. Examples of branching growth in nature include roots, vines, and slime molds. Branching designs show several additional properties with practical relevance. Branches are able to deform independently and interact with the environment providing structural reinforcement to the system through anchoring. Distributing branches across a larger space allows for greater simultaneous coverage for water collection in nature or sensor placement for robotics. Finally, using many different routes for growth improves the reachability of the system in case one path becomes stuck in an obstacle such as a rock or wall. We demonstrated anchoring with a single branch growing through a confined space, then supporting a payload of 66.7 N (15 lbs) at an internal pressure of 50 kPa. We also optimized our branching design to accomplish tasks such as sensor coverage in an unmapped space.

### 3.2.1 Materials and Methods

To optimize the design of these structures we used a gradient-free search where heuristic rewards were calculated from simulation (Fig. 2-A). However, the computation of an expected reward for each candidate design for branching eversion robots intended for exploring unmapped spaces presented a challenge. To provide a reward estimate for the optimization process, we developed a simulator that predicted the final position that an eversion robot reaches through open-loop growth given i) a known map, ii) an initial state, and iii) a parameterized design morphology. The reward was based on an application-specific heuristic calculated from the final state of the robot. Tuning this reward prioritized different spatial properties such as exploration and area-coverage or kinematic properties such as anchoring forces. Since this process still required known maps to calculate expected rewards, we leveraged a set of known archetypal maps that contained relative similarity to the final unmapped target application location. Through this process we were able to optimize for an environment, rather than for any one specific map. A central premise to this approach was that there should be some overlapping similarities to the known and unknown instances of a specific environment for the optimization results to transfer. We detail this optimization framework in the following section.

## Simulation Framework

To predict the growth process of a branching eversion robot in open loop, we simulated the deployment of branches recursively, letting us adapt a set of well-established algorithms. Kinematics and buckling in inflatable beams are well studied [**?**, 106]. Greer et al. consolidated these into a set of algorithms that predict the final position of an eversion robot given the initial state, map, and body-length of the robot [105]. This work has since been refined and the simulation of soft growing robots has been developing rapidly [110, 113, 114]. These algorithms predict how a vine robot will deflect as it comes into contact with obstacles, relying on the contact mechanics

of inflatable beams [78] and assuming the robot will always buckle about a distal environmental contact [**?**]. The specific contact point from which the robot will deflect is determined by the relative orientation of the robot and the obstacle. The robot is assumed to grow tangentially along an obstacle while in contact [105]. These algorithms were validated experimentally and can be adapted to include analysis of confidence or the use of pre-formed bending designs [105, 114].

We built on this prior work to include branching by treating growth as a recursive problem (Fig. 2-D). Branching has been previously introduced for reconfigurable antennas [60, 115], but has not yet been considered for mobility or obstacle interaction. We assumed that each hierarchical level of branching deployed sequentially and that the forces resulting from object interactions in one branch did not impact the position of the remaining structure. To allow for morphological changes during optimization, we parameterized the design space. The number of design variables depended on the morphological complexity of the design. The design parameterization included the number of levels in the branching hierarchy. The other parameters were the lengths of the branches in a level, starting angle of new branches in a level, number of new branches in a level, and a length growth scalar that added variation to the lengths of branches within a level (Fig. 2-B). Along with a parameterized design approach and the algorithms to predict growth, optimization also required an environment (a map or set of maps that contain obstacles) and a heuristic reward function. Since each fitness evaluation depended on the specific map and starting orientation, each evaluation only represented an approximation of the true fitness for a particular design across an entire environment. Therefore, we evaluated fitness for each design on several map instances using our task-specific heuristics. We then weighted these fitness scores into a single composite fitness for each design. This weighting allowed the user to tune the optimization process given the variability in a particular environment. This weighting was chosen to prioritize average performance, a "greedier" peak performance, or the minimization of variability.

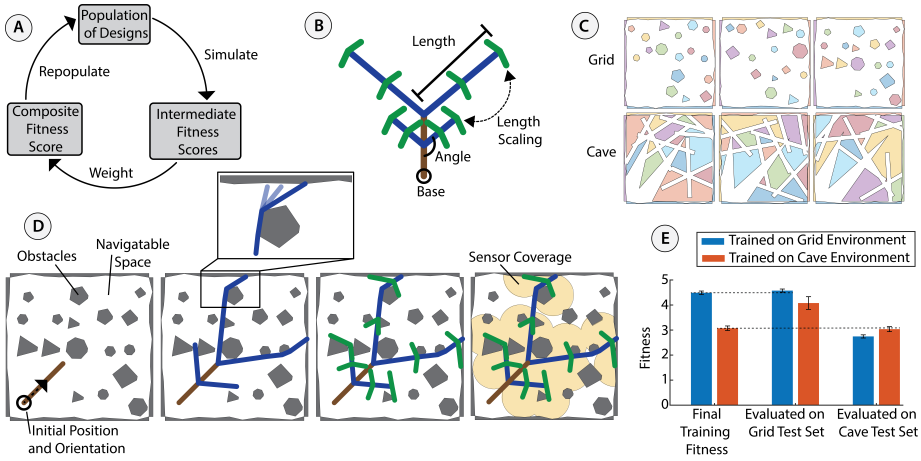



**Figure 3.11**: Optimization process through simulation. A) We used a particle swarm algorithm to guide the optimization of the robot design. Within a generation, each design was evaluated on several maps by simulating open-loop growth. We assigned a fitness score for each evaluation using a task-specific heuristic which then get combined through weighting (e.g. averaging) into a single composite fitness score. Designs were then repopulated based on the composite fitness scores. B) Example parameterized robot design. Each level of the hierarchy is in a different color. Within a level, branch lengths, angles, and a growth scalar determine the morphology. C) Examples of simulated maps from the simulated Grid and Cave environments. Each obstacle is represented by a distinct color. D) Example output from the simulator, where final position is predicted based on initial orientation, the map, and the design. The simulator treats the branching structure as a recursive open-loop growth problem. After simulating growth we can include other post-processing to give task-specific scoring information (in this case sensor coverage). Inset shows buckling about distal obstacle during collision. E) Optimization results for designs trained in different environments. These results show that the optimization transfers well from training environment to unseen test maps (dashed lines). Additionally, each design specialized to its training environment.

## Example Applications

To realize desirable optimization results, the maps and reward function used to guide the design search must be tailored to the intended application. We wrote our simulator to accept 2D maps containing a randomized number and shape of obstacles. Obstacles in the map were closed polygons defined by a set of ordered x and y coordinate pairs. To optimize for an unmapped instance of a known target environment, we used a set of known maps from the same environment in the optimization. To control the randomness between map instances within an environment, we created map-generating algorithms which each produced randomized polygons following a

set of environment-specific rules (see SI.A). This is analogous to real-world environments where even if each instance is unique, the same geological or biological processes drive the creation of an environment. In our experiments we used two computer-generated types of environments—referred to as a *Grid* environment and a *Cave* environment (Fig. 2-C). Details on how we generated these environments are presented in the supplementary materials SI.A. While map sets were selected from one of these environment types, we defined the fitness functions as an application-specific user-defined heuristic. Since the simulation and model predict the final state given input parameters, a fitness function was required to define what constituted a successful design. The following subsections detail example tasks and the fitness metrics used to evaluate designs. We used two different biologically inspired applications as examples in this work.

**Sensor Coverage**

In this example task, the objective was to distribute sensors throughout a cluttered space to maximize coverage with the simplest branching robot design. To calculate a reward, we added a post-processing step to the simulator. At the end of growth, each unique branch deployed a sensor with fixed circular area of coverage at its tip. Since the goal was to maximize area coverage, we only considered unique area as productive. Therefore, we calculated the reward as the union of the area covered by sensors. To balance design simplicity with area coverage we added a cost that depended on several variables. The first consideration for the cost was the efficiency of the sensor coverage. In other words, if the covered areas were not overlapping, each sensor was providing productive information. We penalized both the number of total sensors and the total length of the robot design, where each was scaled by the efficiency of the covered area (how much of the sensed area overlapped). Additionally, we added a small penalty based purely on the total length of the design to minimize the design in the case that two designs had similar efficiency. Finally, we normalized each of these four values (union of the sensor area, number of branches scaled by efficiency, length of design scaled by efficiency, and raw length) to fall in the range [0,1] and then

weighted them to balance coverage and simplicity.

### Anchoring

Analogous to root growth in plants, the goal in this task was to distribute forces across the branched structure to anchor into the environment. Even with low internal pressures, we assumed anchoring forces would become appreciable due to two synergistic effects: First, we assumed each branch would act as an inflatable anchor, capable of jamming in narrow or constrained spaces (Equation 1) where Ftip, P, Ac, and Mu represent the anchoring force of the pouch, internal pressure, area in contact, and coefficient of friction respectively [116]. Second, we assumed that as the robot wrapped around or grew past obstacles, the capstan effect would produce an exponential increase in anchoring force (Equation 2) with Fanchor as the anchoring force of the branch and gamma as the total change in angle along the path of the branch [61, 78]. We assumed that this capstan effect would amplify the frictional increase from jamming in narrow spaces.

$$F_{tip} = 2 \cdot P \cdot A_c \cdot \mu \tag{3.9}$$

$$F_{anchor} = F_{tip} \cdot e^{\gamma \cdot \mu} \tag{3.10}$$

For our fitness score, we used a nondimensional scaling of the anchoring force. The anchoring force for each branch can be measured based on the interaction with obstacles which predicts jamming and capstan friction. We assumed branches were narrow and did not provide any jamming on their own, and instead relied on a pouch anchor at the tip of each branch to provide the base anchoring force for that branch. This allowed us to calculate anchoring forces for the branched robot based on the total angle change of each branch, where the total anchoring force is the sum of the anchoring force of each branch. While in practice, that magnitude of the anchoring force would depend on the internal pressure of the robot, the size of the pouch at the

tip, and the friction of the material of the anchors, we assumed that these properties would scale the magnitude of the anchoring force equally for all branching morphologies, thus we ignored them during optimization. For this task, we used a simplified design space to improve accuracy of the model predictions, so we did not add a penalty to the fitness function for the complexity of the design.

**Search Methods**

We found multiple gradient-free optimization techniques that enabled the optimization of branching eversion robots for operation in unmapped environments. In S2 we show both a customized evolutionary algorithm and a commercially available particle swarm algorithm (Matlab) that both yield similar performance [117]. For the results in this paper, we used the particle swarm algorithm. Though we demonstrated that multiple gradient-free methods perform suitably, searching the design space was an interesting challenge. The lack of an explicit objective function motivated our use of gradient-free search methods. The challenge of selecting the proper search method was complicated by the fact that the fitness landscape was heavily dependent on the task-specific fitness function and the set of maps used in the training phase. Furthermore, since there was symmetry and redundancy in the design space, some dissimilar designs performed equivalently. Though there is no guarantee that a single global optimum existed, we did not test local search methods such as hill climbing algorithms due to the high number of local optima present in many of the fitness landscapes [118]. Finally, to avoid overfitting we introduced randomness in the start position and orientation for each fitness evaluation which added noise to the fitness evaluation. These complicating factors led us to choose a search method that was sufficient, rather than hunting for an optimal search method since the optimal search method and associated parameters would depend on the specific task and environment. Population based methods such as particle swarm and evolutionary algorithms were good search methods though each benefitted from multiple runs with different random number generator seeds to ensure a

quality solution [118]. Ultimately the fitness landscape was smoother than we expected (evidenced by fast convergence to quality solutions), likely due to the stochastic initial position and training maps. For these tasks in these environments there may be sufficient search methods that are computationally less expensive but do not scale as well to harder problems. A comparison of the two methods we tested and our sufficiency criteria are included in the supplementary materials S2.

**Hardware Design**

We fabricated the branching robot designs using a thermoplastic polyurethane (TPU) laser-welding technique. To adapt simulation results into manufacturable hardware, we imported the branch joint locations and angles into computer aided design (CAD) software (Solidworks) and added thickness to each line (Fig. 3.14). With the full design outline, we exported as the file to a digitally controlled CO2 laser cutter. We used a laser welding approach to precisely join two sheets of TPU (Fibre Glast Stretchlon 200) along the outer seam only. Laser welding is a repeatable fabrication method for fabricating customizable pouches with a long lifespan that has previously been used to manufacture soft bending inflatable actuators [119]. This fabrication method allowed us to simultaneously cut and seal the TPU to remove excess material from the exterior of the robot which aided the eversion process. This material was thin (which helped deployment) and elastic (which prevented creasing). The laser welded seams supported up to 70 kPa (as documented by Amiri et. al. [119]). Laser welding the TPU required fine tuning of the settings of the laser cutter and preparation of the TPU film with a heat-press to eliminate bubbles or wrinkles. The laser settings and TPU properties are included in the Supplemental Materials section D.

### 3.2.2 Optimization and Hardware Results

#### Transferability and Specialization

The optimization process should result in a design that is transferrable to unseen instances of a particular environment, it should also result in specialization to the environment used during training. To test this hypothesis, we compared the designs that were each trained in different environments. Training followed the procedure in Section 2.3 for the sensor coverage task, and was run five times with different random seeds. The top performing design, based on fitness for its representative training set, was selected for evaluation. First both designs were evaluated on their own training set (i.e. the design trained on the Grid Environment was tested on its own Grid Environment training set to provide a baseline of performance). The results from these training sets show that for the same task with the same reward heuristics, the Cave Environment was more challenging. The two optimized designs were then each tested on unseen evaluation map sets for both environments (Fig. 3.11-E). The design trained on the Grid Environment maintained its performance on the Grid Environment evaluation set compared to the training set, and similarly the design trained on Cave Environment maintained its performance on the Cave Environment evaluation map set. These results show the transferability of designs trained on known maps to unseen new maps in the same environment. We also evaluated each design on the other environment (i.e. the design trained on the Grid Environment was evaluated on the Cave Environment). As seen in Fig. 3.11-E, the top design for each environment was the one that was trained natively in that particular environment. This experiment showed that the optimized designs specialized to the training environment, and also provided a sense of the relative challenge of completing a given task in different types of environments.

**Impact of Diversity in Training Data**

Number of Known Maps: To quantify the impact of this optimization approach and to measure how much training data is required to generate high quality designs, we compared a set of designs that were optimized with different training datasets. These optimizations were run on the Grid Environment and with the sensor-coverage heuristic. The baseline unoptimized design was manually selected using the authors' best intuition with no further training or optimization. The optimized designs were trained on known a set of known maps, varying the number of unique maps in the training set. During training, the initial condition of the design used either a constant initial condition (location and orientation) or was variable from generation to generation. For the optimizations with more than one map in the training data, we measured fitness once per design per generation to make sure each design had the same number of fitness evaluations. We ran the optimization five times with different random seeds with and from these five runs selected the best performing design (measured on the training set) to be evaluated. We also measured fitness over generational time through ten runs of a single test configuration showing the training process is repeatable (Fig. 3.12-A). To evaluate a design, we tested on 25 unique, unseen instances of the Grid Environment with three different initial conditions for a total of 75 fitness evaluations per design.

Performance in the unseen evaluation maps was significantly improved by the optimization process (Fig. 3.12-B). The unoptimized design performed poorly and had a high variance. The next simplest optimization, training on one map with constant initial conditions, improved performance relative to the unoptimized design but resulted in overfitting to the single situation presented during training. Injecting noise in the training by using variable initial conditions and using additional maps both increased performance above this baseline. Moving the start orientation helped prevent overfitting evidenced by the jump in performance between the two designs trained on only one map. Adding additional maps further improved the transferability of designs, but only incrementally. Though our results show a positive relationship be between

the quantity of training data and the transferability of the designs, the specific amount of training data required to improve performance in other cases will depend on the environment and task.

Tuning Performance Through Weighting: The choice of weighting method had a significant impact on the distribution of performance of optimized designs on unseen evaluation sets (Fig. 3.12-C). During optimization, we evaluated each design on several different maps in the training set since each instance with a given initial orientation only provides an approximation of true fitness. Evaluating a design on several training maps during optimization provided more information which can lead to a better approximation of true fitness. However, how these multiple approximations get weighted and combined into a single fitness score led to different performance of the final designs. These weighting methods are a powerful design tool because they provide selection pressure and can shape the probability of different outcomes in the transfer to unseen instances. Though there are many possible weighting approaches, we selected three for evaluation: averaging, selecting the best fitness, and minimizing deviation. In the optimization that minimized deviation, 25% of the composite score was based on the average fitness to ensure there was some pressure to improve performance. We optimized each on the Grid Environment for the sensor coverage task, varying only the weighting method used. We also compared the results to an optimization run with no weighting (with only one fitness evaluation per design). We then tested these designs on an unseen evaluation maps from the same Grid Environment and compared the distribution of results. Figure 3.12-C shows the probability distribution for the scores of each design in the evaluation set. Selecting the highest score resulted in greedy performance, with the best possible outcomes during evaluation but with a higher spread in the distribution including some poor scores. Averaging scores resulted in a mostly positive performance but performed worse than the multi-objective weighting that also minimized the standard deviation. A weighting that only considered the deviation would not necessarily select for high performance but combining the mean and standard deviation into a single score resulted in a design that showed both high performance and consistency across the set of evaluation maps. The weighting method

selected had a noticeable impact on the distribution of performance on unseen maps, but comes at a cost of increased computational effort through additional fitness evaluations in each generation.

### Unique Capabilities of Branching Vine Structures

In this section we consider the additional benefits of biologically inspired branching. Branching robots offer unique benefits in the ability to monitor multiple locations simultaneously as shown in the sensor coverage task. In time sensitive situations, a branched robot can explore multiple areas faster since branches grow in parallel compared to a single-path design or active steering using sequential redeployments. Additionally, the branched structure can help mitigate the phenomenon of trajectory condensation, which we show by comparing the reachability of branched and single-path designs. Furthermore, we demonstrated the benefits of the improved anchoring force with a physical prototype.

Reachability and Coverage:To compare branched and single-path designs, we studied the reachability of each in both simulated environments. As previously reported, in open loop eversion robots are limited by trajectory condensation through interaction with obstacles [105]. Branched designs are able to recover non-redundant mobility through a space by deploying new material that is independent of prior obstacle interactions. To provide a fair comparison between these two classes of designs and explore the issue of trajectory condensation, we used a reachability comparison. For the single-path robots, we ran 50 sequential deployments, each with a different initial orientation. In an example from the Grid Environment, these 50 unique initial configurations were reduced into 6 final configurations. Similarly, in the Cave Environment, the 50 unique initial configurations turn into approximately 5 final configurations once growth is complete. For each of these instances we took a buffer around the path of the robot to define the reachability, then took the union of this area across each of the 50 deployments. For the branched systems, we optimized the design for each environment with the reward heuristic that measured a buffered reachable area surrounding the path of the robot. The reachability of the branched design

was only calculated from a single deployment. On the Grid Environment, the branched design reached 93.0% of the space with a single deployment compared to the multiple deployments of the non-branched design which covered 68.3% of the space. In the Cave Environment, the branched design also outperformed, covering 94.3% of the space compared to the non-branched which only reached 61.6% of the space (Fig. 3.13).

Demonstration of Deployment for Sensor Coverage: We demonstrated the fabrication and deployment of a design optimized in simulation. We optimized for sensor coverage and used the Grid Environment for training. We created a manufacturable design from the optimization output by adding thickness to each branch and fillets to each joint, where size was scaled by the level of branching hierarchy (Fig. 3.14). We evaluated the branching robot on an example map fabricated with 3D printed obstacles. We used a laser welding fabrication approach to ensure precision and repeatability in the manufacturing process. This approach simultaneously cuts and seals layers of TPU and has previously been used to make soft bending actuators [119]. To deploy the system, we took the cut TPU and placed it inside a pressure vessel, inverting and attaching the non-branching end. Our approach was repeatable and allowed for redeployment after manually resetting the system. Through hardware validation we observed several properties. Though the device is scalable, deployment was easier at lager sizes since there was less internal friction to overcome while transporting new material to the tip. The device was reusable but required manually resetting the robot between trials and overtime the TPU seal developed leaks. Furthermore, head-on collisions with obstacles especially at branching vertices sometimes prevented growth, though this effect may be overcome with nutation [107]. Though the path taken by the robot was highly sensitive to initial position and orientation, the optimized design was able to reliably navigate through the environment due to its branching structure and high degree of compliance.

Optimized Anchoring Forces with Hardware Validation: Branching provides significant opportunity to grip inside of an environment due to capstan friction and the pouch-anchoring effect. We optimized two designs in simulation according to the task in 2.2.2 on the Grid and

Cave environments (Fig. 3.15). We simplified the design space and added a pouch at the end of each branch to improve the accuracy of our anchoring force prediction. The similar force capacity and optimized design show this problem has a simpler solution compared to other tasks, especially since we do not penalize for length or design complexity in this task. We also fabricated an example Cave Environment using 3D printed obstacles to validate force capacity. A single pouch with no capstan effect held 0.65 N, and the optimized design held 4.25 N when manually deployed. The measured anchoring magnification was 6.54, compared to the model prediction of 6.86. This difference comes from the assumption in the model that each branch makes good contact and evenly shares the load. In the experiment we found that out of the six branches, one did not make contact with the sidewalls and another had slack preventing it from sharing the load. The TPU robot weighed only 5 grams and therefore had a 86x payload to weight ratio. The robot was unable to deploy itself into the environment due to the closeness of the branches output from simulation- limiting branch diameter. The approach of deploying into an environment and subsequently loading the robot is an interesting alternative to traditional robotic gripping and manipulation. Furthermore, this test showed the adaptability of the optimization approach to scale to a variety of tasks. Finally, using stiffer materials we tested a high-force version (Fig. 3.10) with a peak payload capacity of 66.7 N at only 50 kPa of internal pressure and holds promise as a high force soft robot [47].

### 3.2.3 Supporting Details

#### Computer Generated Environments

In this project we used two computer generated environments: a Grid Environment and a Cave Environment. To allow for fair comparison between designs optimized for each environments they have the same size and are enclosed spaces. A 100x100 unit box bounded every map in both environments. The outer walls had a randomized texture to prevent the design

search from over-exploiting growth along these outer boundaries. Additionally, both environments had an empty region in the bottom left of the space to allow for randomized initial conditions at each fitness evaluation. The Grid Environment was comprised of a grid of convex polygons. The randomized variables were: i) the number of polygons in a particular row, ii) the number of rows, iii) the number of points in a particular polygon, iv) the size of a particular polygon, and vi) the orientation of a particular polygon. Maps in the Cave Environment began with a solid 100x100 obstacle and subsequently had randomized pathways cut out from the initial solid obstacle. These pathways were rectangles with dimension 70 units by 5 units. Three of these pathways were initialized at 4 distinct locations ([25,60],[75,25],[80,80],[55,55]) for a total of 12 pathways subtracted from the initial obstacle. We then added a random rotation and added/subtracted a random value to the X & Y coordinates of the centroid of each obstacle. Finally, two channels with randomized tip locations are added to connect the starting region to the network of pathways.

**Search Method Comparison**

To ensure a search method is finding quality solutions, we used a simplified task that does not rely on obstacle interactions or introduce randomness into the fitness evaluation. For this task, we initialize the given design in an open space with no obstacles present. We rewarded unique area covered and penalized the total length of the design. To improve understanding of the fitness, we set the penalty for length to be an order of magnitude smaller than the area for reward. This means that an optimal design should maximize the number of sensors with no overlap between the sensed areas. Any designs that meet these criteria can then be compared through the total length used to maximize this sensor area (where a shorter length is better). While analogous to a circle packing problem, the parameterized design of the robot added additional constraints which made the optimized solutions less dense. The results from a manually coded and a commercial toolbox are seen in Fig S.2. The results in (A) show the custom evolutionary algorithm and in (B) a commercially-available particle swarm search (Matlab). The total length of the design in S.2-A

was 2303.1, and the total length of the design in S.2-B was 2303, these results were within .005% of each other. To test the reliability of the results we ran five trials of evolutionary algorithm, and two of the five solutions were within 5% this optimal length. The fact that three of the five random seeds produced sub-optimal designs shows the risk of getting stuck in a local optimum, consistent with our use of an elite pool. It also shows that through using multiple runs with different seeds to the random number generator, we were able to mitigate this problem. Finally, the two optimized designs in Fig S.2 have nearly the same fitness but with distinct morphologies, showing that there may be multiple fit design solutions for a certain task with this type of robot. For the evolutionary algorithm we used a ($\mu$+$\lambda$) method with an elite pool of six in a population of 54 to preserve promising candidates since each fitness evaluation only provides an approximate estimate of true fitness. Though the elite pool can cause premature loss of design diversity, in our case it also helped ensure convergence given the noise in the fitness evaluation. We used a relatively high mutation rate without crossover since in our representation there were vestigial design parameters depending on the morphology of the design (a function of the structure of the simulator), and focusing on mutation allowed us to only alter relevant genes which reduced computation time.

**Laser Settings and TPU Properties**

We used a laser welding process for repeatable fabrication of the branching vine robots. This fabrication method allowed us to simultaneously cut and seal the actuator to remove excess material from the contractile section of the actuator which can restrict motion. The membrane that encloses the dielectric fluid was made out of Fibre Glast Stretchlon 200 TPU (thermoplastic polyurethane) which can stretch up to 400-500% its original length. We performed tensile tests on five samples to test the elasticity and strain of the TPU material. The samples were strained at 0.05mm/mm/s until failure.

This material is very robust making it a great material choice for a collapsible robot. Laser welding the TPU requires fine tuning of the laser cutter settings until the pouch successfully seal.

To laser weld the TPU layers, we used the following procedure:

Steps for TPU Laser Sealing

1. Place the TPU layers on heat press and roll out any bubbles.
2. Press both layers of tpu at $77^{o}$F for 2 minutes
3. Let the TPU cool on the heat press for 5 minutes

To laserweld the actuator, we used the PLS6MW laser cuter from Universal Laser Systems. We used two sets of settings to cut and seal the actuator. The first set of settings cuts and seals the the actuator simultaneously. Those settings are 80 % power, 100 % speed, and 500 pulses per inch at a bed height at 0 mm. We also used settings that just seals the top TPU layer to the bottom layer. These settings are These settings are 20 % power, 100 % speed, and 500 pulses per inch at a bed height at 0 mm.

**High Strength Anchor Demo**

To hold the payload seen in Fig. 1, we adjusted our materials and fabrication methods to support greater force. We used a thicker TPU (Stretchlon 800) which prevented the body of the robot from significantly deforming or tearing under load. This thicker TPU prevented a quality laser-weld seam which was our method for creating a branching design. To accommodate this change we used an impulse sealer to create a straight tube without branching. With the non-branching we positioned the robot below a target passageway, deployed the robot through the passageway, and then clipped on the payload to the base of the robot suspended in air. The robot held 66.7 N (15 lbs) at an internal pressure of 100 kPa, the same pressure used to deploy the robot through the passageway.

**Anchoring Tests**

We evaluated how consistent the anchoring effect is by comparing several simulated predictions to measured forces in the same configuration. We used the same map and same robot design for every trial. Results show that the accuracy of the prediction depends on configuration of the robot. Redundant branches in the same passageway seem to not contribute well to overall anchoring force and may be the cause of error in the prediction.

## 3.3 Acknowledgements

This work was carried out at the University of California, San Diego, and at the Jet Propulsion Laboratory, California Institute of Technology, under contract with the National Aeronautics and Space Administration, and sponsored by the U.S. Government. P.E. Glick Is supported by a NASA Space Technology Research Fellowship.

Chapter 3, in part, is a reprint of the material as it appears in IEEE International Conference on Soft Robotics 2019. Luong, Jamie; Glick, Paul E.; Ong, Aaron; deVries, Maya S.; Sandin, Stuart; Hawkes, Elliot W.; Tolley, Michael T. The dissertation author was the co-primary investigator and author of this paper.

Chapter 3, in part, is currently being prepared for submission for publication of the material. Glick, Paul E.; Adibnazari, Iman; Drotman, Dylan; Ruffatto III, Donald; Tolley, Michael T. The dissertation author was the primary investigator and author of this paper.

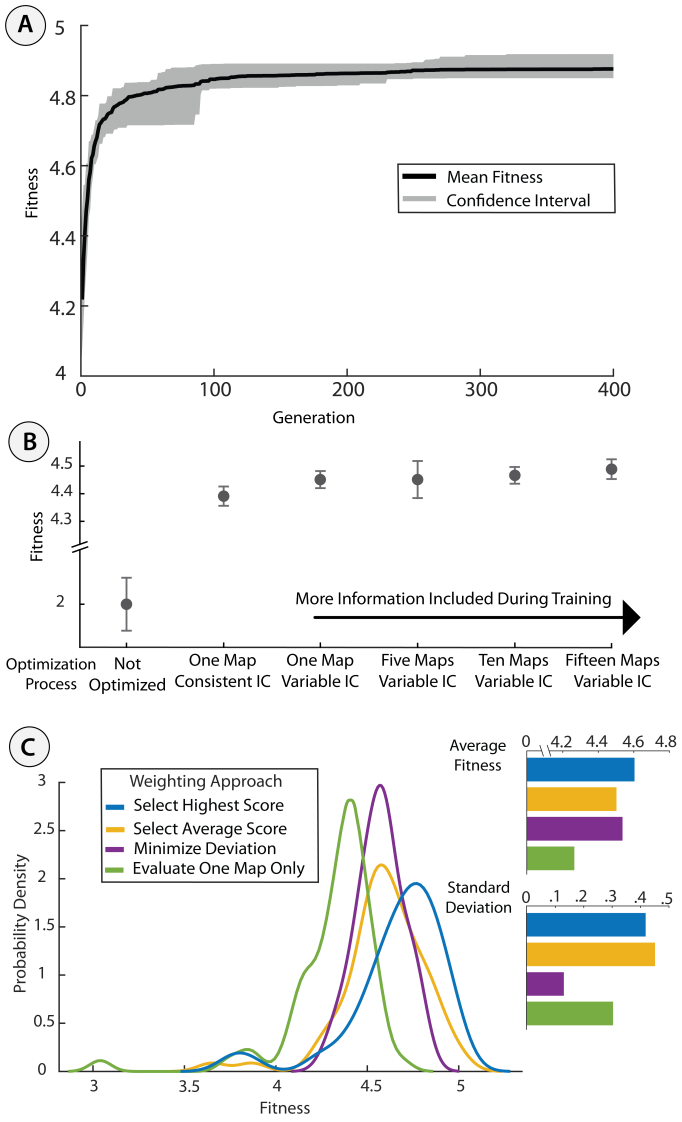



**Figure 3.12**: Evaluating the impact of diversity in the training data. A) Fitness improvement over generational time from a sample of 10 runs. B) Fitness on unseen evaluation maps by optimization approach. The unoptimized design that was selected based on human experience performed the worst. Two independent variables were compared in the optimization process: the number of maps used during training and the initial conditions (IC's) used. Using different starting positions and orientations (Variable IC's) reduced overfitting in the case of training based on only one known map. Additional information during the training stage about the environment (in the form of including more known map instances) improved performance but with diminishing returns. C) Distribution of fitness scores during evaluation based on different weighting methods. Selecting the highest fitness improves performance but with tradeoff of poor performance in some cases. Minimizing deviation results in a consistent performance. All methods show some improvement from only using one fitness evaluation.

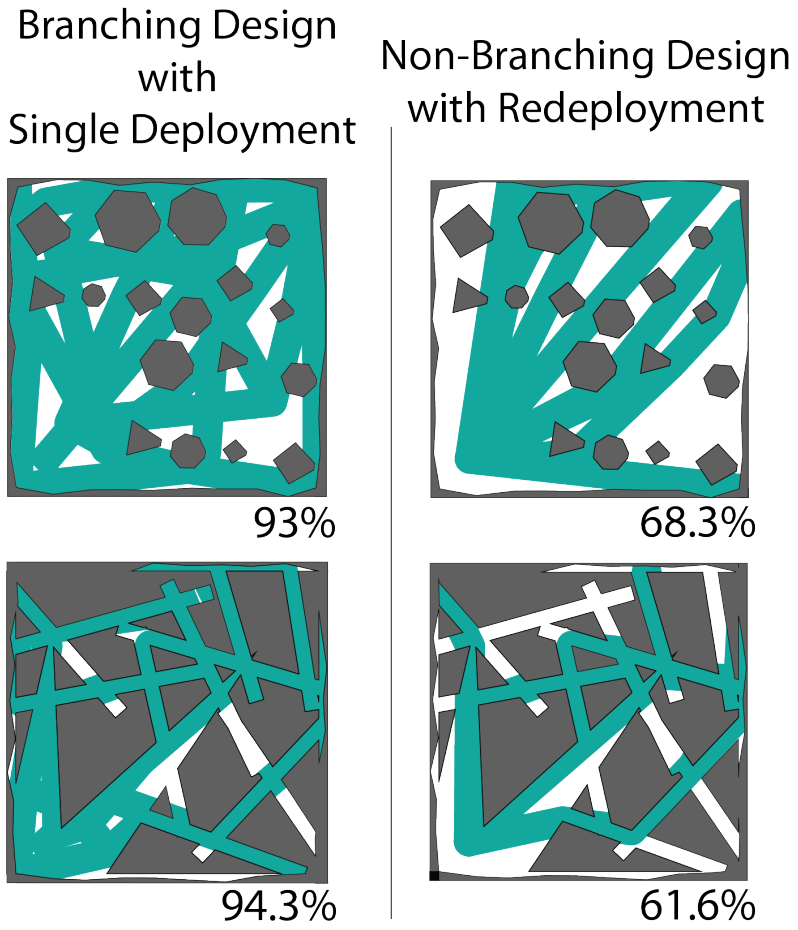



**Figure 3.13**: Comparison of the reachability of the space. Even allowing many redeployments, a vine robot without branching cannot access large areas of the space. In contrast an optimized branching robot can cover much more of the space once deployed. Branching successfully mitigates the issue of trajectory condensation and provides other interesting properties like covering multiple locations simultaneously, distributing forces, and faster exploration of a space.

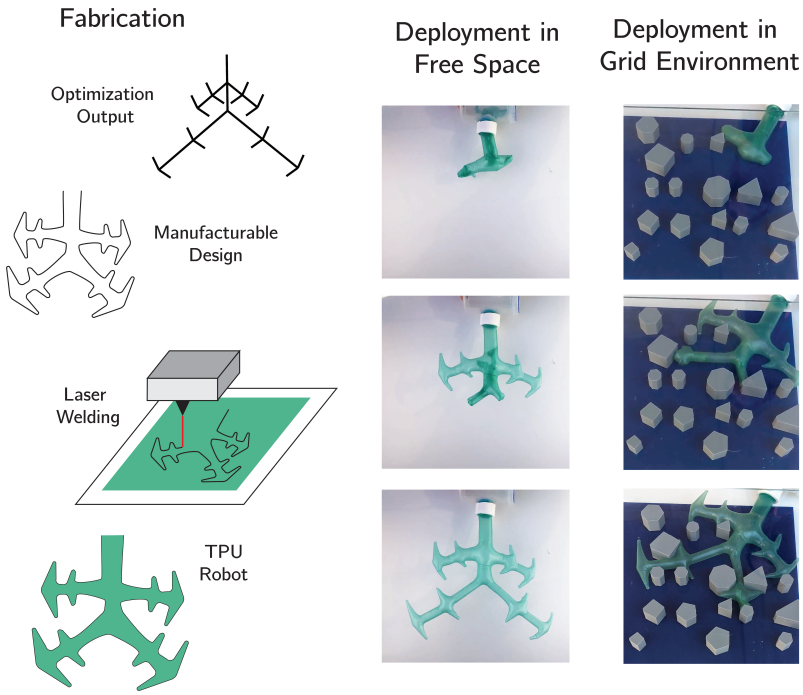



**Figure 3.14**: Demonstration of fabrication and deployment of an optimized design. To manufacture the designs we added thickness to the line-output and cut the robot out of TPU using a laser-weld process. Decreasing the diameter of the robot at each hierarchical branch-level improved deployment.

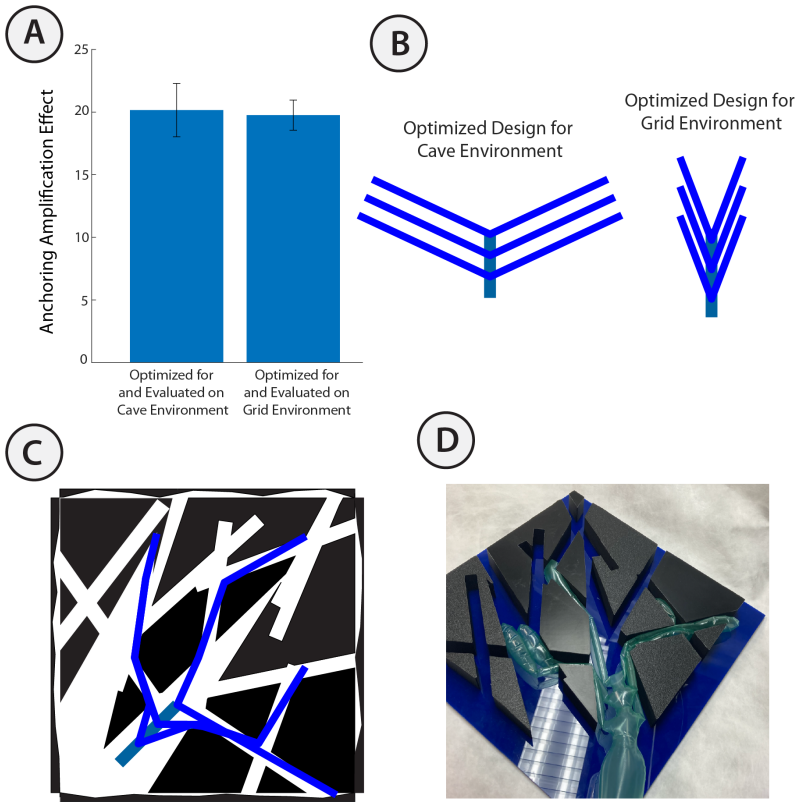



**Figure 3.15**: Optimization and hardware validation of anchoring. A) Anchoring amplification effect of an optimized branching vine robot compared to a single pouch anchor in both cave and grid environments. B) Optimization output of similar designs from different training environments. C) Simulated final position of optimized design in cave environment. D) Manually deployed robot to ensure alignment with simulation, used for anchoring validation.

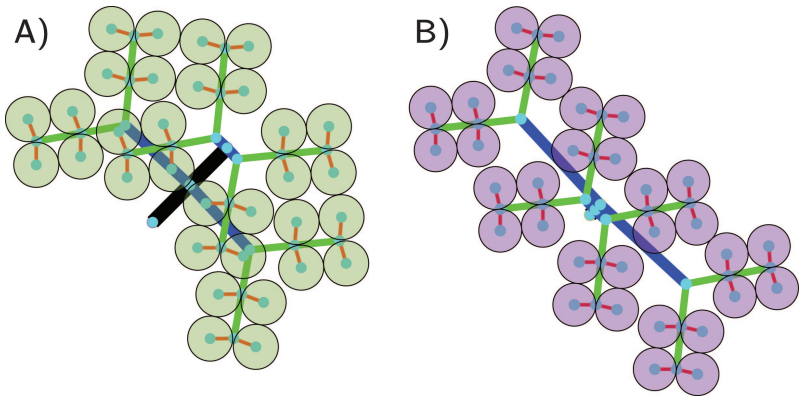



**Figure 3.16**: Comparison of the results with the two different optimization approaches. Though the morphologies are different, the fitness of the two designs were within 0.005% of eachother. A) Custom evolutionary algorithm. B) Commercially-available particle swarm search.

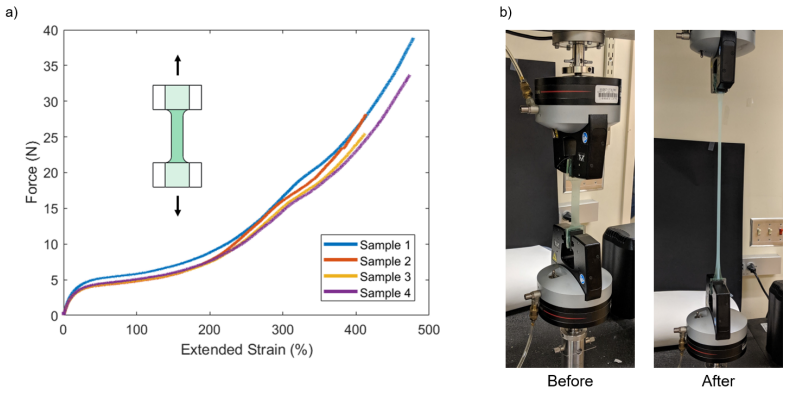



**Figure 3.17**: TPU testing. a) Tensile testing of the TPU material. b) Stretching TPU material 400%-500%.

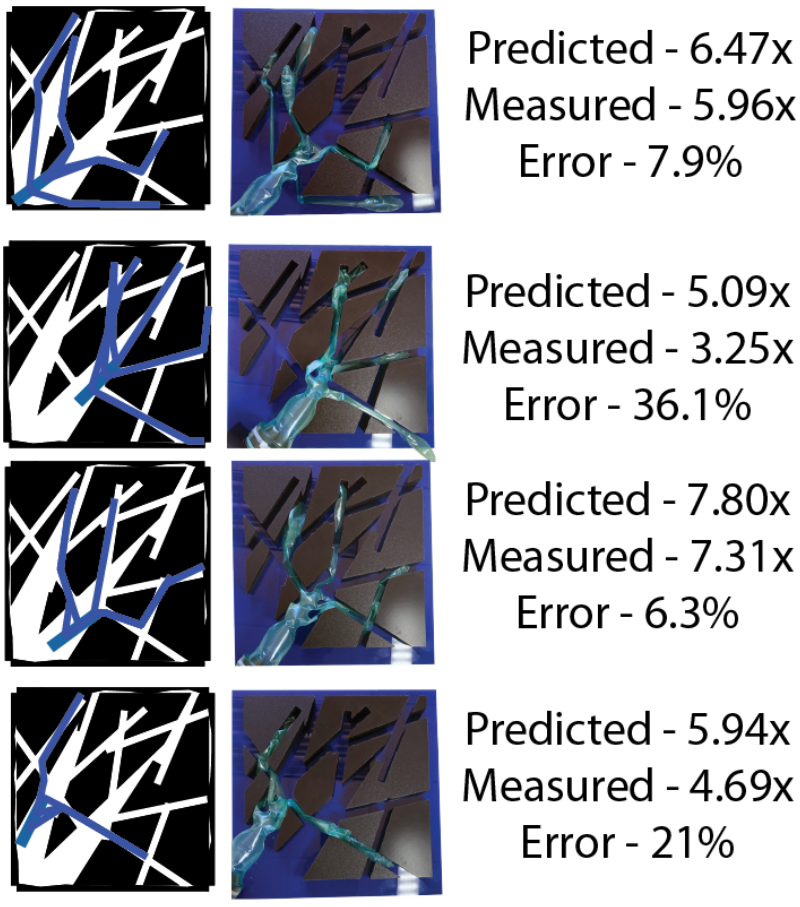



**Figure 3.18**: Repeatability of anchoring.

# Chapter 4

# Varying the Complexity of Object Interactions in Soft Gripping

This chapter explores projects with varying levels of degrees of freedom and actuation complexity. The electrostatic-gecko anchor and the inflatable pouch anchor operate with a simple on-off behavior and are designed to conform to surfaces within a broad range of specifications. In contrast, if greater control is required of soft robots, providing distributed actuation is an ongoing challenge since fluid power must be routed through small, interconnected pathways. Magnetorheological fluid with electropermanent valves may provide a more controlled approach to grasping an arbitrary object with a reconfigurable torque profile along the length of the gripper.

## 4.1 Long-Duration Surface Anchoring With a Hybrid Electrostatic and Gecko-Inspired Adhesive

For many robots and systems, it can take as much energy to maintain a static position as it does to move. This is particularly true when attempting to reach difficult to access areas, where systems such as quadcopters and climbing robots are required. The ability to maintain a

temporary stable pose is desirable under various scenarios; to hold position during recharge [120], to reduce sensor or camera noise [121], to observe a single location or activity for an extended period of time [122], and to ensure safety in the case of interruptions to communication [123]. For untethered payloads or robots, power consumption while holding a pose is a significant design consideration [124] [125]. For most wheeled or jointed robots, this can be done with mechanical brakes in the drivetrain or by relying on low backdrivablilty gearboxes. However, for systems that move without the aid of -or even against- gravity, the task becomes more complex. Quadrotors, free-flying robots, wall-mounted payloads, and wall-climbing robots must use a wider variety of methods to achieve a safe, stable waiting position.



**Figure 4.1**: Two sizes of electrostatic anchors, 54x60 mm and 66x98 mm, that can be integrated with mobile robots or static payloads. With a mass of 30 g and 37 g including an on-board battery, each can anchor a payload for over one week.

To perch or hold position on a vertical surface, controllable adhesion or anchoring is required. For rough surfaces, such as porous concrete, brick, or textured rock, the use of sharp hooks, microspines, or claws may be sufficient [126] [127]. Removable anchors or temporary drilling are suitable for supporting large loads, but can permanently mar or alter the surfaces that they attach to [128] [129]. To nondestructively maintain position on smooth surfaces, such as

glass, there are a variety of options. Suction is a power intensive process, noisy, and not well suited for untethered systems [130]. Tacky or chemical adhesives generally require as much force to engage as they require to disengage and often damage or leave residue on the surface, prohibiting use in most mobile systems. Alternatively, gecko-inspired adhesives, by contrast, take no power to maintain adhesion, scale with area and thus can support large loads, and can be disengaged with low forces due to anisotropic adhesive behavior. Indeed, gecko-inspired adhesives have been used extensively for wall climbing [58] [24] [131], manipulation [47] [36] [42], and even as temporary anchors on the international space station [38].

Despite their advantages, gecko adhesives do have several limitations. On semi-smooth or rough surfaces, with RMS greater than a few microns, their performance declines. It has been shown that a hybrid adhesive, using both an electrostatic film coated with a thin layer of gecko-inspired adhesives, demonstrates robust engagement and improves adhesion on semi-smooth surfaces [35] [132]. Electrostatic adhesives alone can enable wall-climbing [133] [134], manipulation [35] [135], and temporary anchoring [136], but provide a lower adhesive pressure than the gecko-electrostatic hybrid [132]. The power consumption of an electrostatic adhesive pad itself is very low, on the order of a few microwatts, and is due to leakage current. However, the electronics that supply the high-voltage across the electrodes typically consume power on the order of 100's of milliwatts which may be relatively large for an untethered system, especially over long periods of time.

Here we present a low-power electrostatic anchoring device paired with a surface layer of gecko-inspired adhesives that is capable of temporary, repeatable anchoring for as little as few seconds to over 5 weeks. We greatly increase the maximum supported distance between the center of mass of a payload and the vertical surface by implementing two structural layers on the hybrid adhesive. To minimize peeling a rigid plate distributes load through a soft foam interface in the direction normal to a surface, allowing the electrostatic adhesive to react the torque caused by mass suspended off of a vertical surface (Fig. 2). Between the rigid plate and the adhesive

surface is a compliant foam, providing sufficient compliance for the gecko-inspired adhesive to engage effectively and support large shear forces. We model this effect, and can design an anchor for a particular payload size, load, or surface. To extend the operable life of the anchor, we introduce two primary innovations. We select a dielectric material that does not degrade after over 5 weeks of operation, in contrast to previously used materials that failed in a matter of hours. We also reduce power consumption of the device by cycling power supplied to the embedded high-voltage converter. This approach takes advantage of the natural capacitance of the electrostatic adhesive, and allows it to maintain adhesion while reducing power use by an order of magnitude. The system is non-marring and maintains performance on semi-smooth surfaces such as wood, drywall, and painted metals. In this paper, we discuss design considerations that allow for this approach to loading the hybrid adhesive, present our manufacturing process, demonstrate the improved longevity of the device, and quantify both its load capacity and power savings.

### 4.1.1 Design of the Electrostatic Anchor

The goal of the electrostatic anchor design is to realize a low power device that is capable of maintaining adhesion for multiple days and is scalable to support payloads of various masses and geometries. To meet these demands, we implement a new backing structure that allows for payloads to be suspended further from the wall, model the limits on payload mass as a function of anchor geometry, design the anchor to maximize payload capacity, investigate material selection for the dielectric insulator, and introduce a switching circuit to reduce power usage by an order of magnitude.

The limits on payload mass, $m_p$, are a function of both the anchor geometry and adhesive capabilities (see Fig. 4.2). To design an effective anchor, we model the two primary modes of failure: sliding and rotation off the wall. Shear sliding can be evaluated based upon the shear adhesion supplied by the hybrid adhesive pad. As shown in Eq. 4.1, the peak shear stress provided by the hybrid adhesive, multiplied by the pad area must be greater than the payload weight to

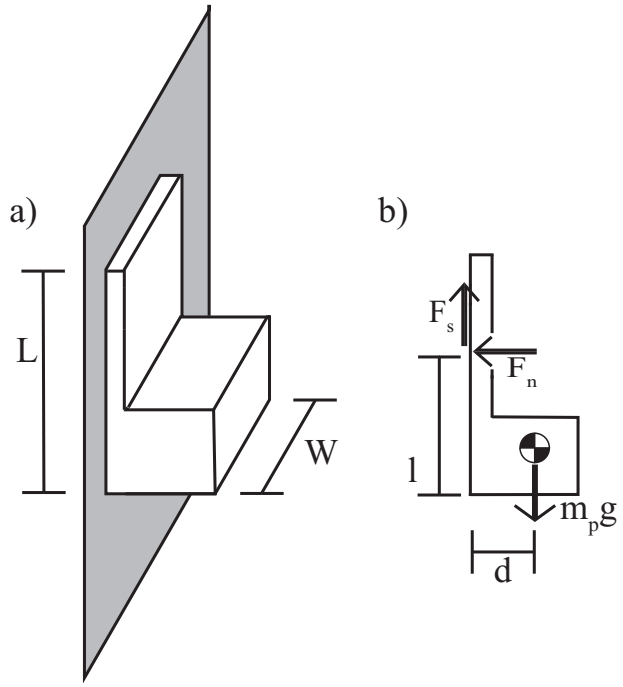



**Figure 4.2**: Free body diagram of the anchor. The temporary anchor allows payloads or robots to rest on vertical surfaces. a) Diagram of the anchor on a vertical wall, with the overall pad size labeled. b) Free body diagram of the anchor on a vertical wall. The force of gravity acts at the center of mass of the payload while the adhesive forces act at the center of adhesion pressure. These values are used to model the load capacity of the anchor.

prevent sliding,

$$F_s > m_p g \tag{4.1}$$

where $F_s$ is the peak shear adhesion, $m_p$ is the payload mass, and $g$ is acceleration due to gravity.

The second constraint, rotation off the wall, can be derived from a balance of moments about the bottom edge of the anchor which is in contact with the wall. The anchor provides a maximum moment resistance, $\tau$, that must be greater than the mass of the payload times its center of mass measured from the vertical surface, $d$. This moment resistance can be approximated as the net adhesive force in the normal direction $F_n$ applied at the center of pressure. These values in

turn are functions of both pad area and anchor length L. This relationship is shown in Eq. 4.2

$$\tau > m_p g d \quad , \quad \tau = F_n(W,L) \cdot l(L) \tag{4.2}$$

where $\tau$ is the moment resistance provided by the adhesive, $F_n$ is the anchor's normal adhesion force, l is distance from the base of the anchor to the adhesion center of pressure (typically half the anchor length).

In typical use, the value of d is greater than the anchor thickness, 3 mm, due to the mounting of an added payload. This results in the moment resistance of the anchor acting the primary failure mode for the sizes tested as the pure shear strength of the gecko-inspired material is over an order of magnitude higher than the hybrid adhesive normal adhesion [133] [137]. Therefore, the previous failure criteria were simplified to directly estimate payload force capacity, $F_p$, based on the anchor's peak normal force and geometry.

$$F_p = m_p g = F_n \left( \frac{l}{d} \right) \tag{4.3}$$

It is important to note that while the peak $F_s$ is largely decoupled from $F_n$, due to the nature of directional gecko-inspired adhesive the peak $F_n$ does increase based on the applied shear force [58]. The magnitude of this effect is difficult to quantify due to its dependency on the surface material texture and roughness [137]. Therefore, for a simplified analysis the normal force component from the gecko-inspired adhesive has been omitted and left for future work, resulting in a more conservative estimate. This results under estimate of payload capacity at low $d$ values and on smooth surfaces, particularly on glass as seen in the later experimental data. We validate these models experimentally (see Results section).

A key implication is that the distance between the center of mass of the payload and the wall, $d$ in Figure 4.2, directly limits the maximum mass that the anchor may support. Therefore it is ideal to have the anchor longer in the vertical direction in order maximize $l$, the distance from

the anchor base to the center of adhesion pressure. However, to distribute stress evenly across the adhesive surface, it is also required to have a stiff element in the anchor. To achieve the desired stiffness while minimizing the thickness and mass of the anchor, we use a thin magnesium plate. A further implication is that the length of the anchor is a more important parameter than the width of the anchor. While increasing the overall area of the anchor increases the total adhesive force, while increasing the length of the anchor increases both the adhesive force and the moment arm over which the adhesive force acts. This indicates that a long thin anchor is the most efficient design, though both the width and length dimensions are typically constrained by the application.

Material selection for the dielectric insulator film has a significant impact on overall electrostatic film performance. Adhesive force is proportional to the square of the electric field strength, which is in turn dependent on the material's dielectric strength and thickness. Furthermore, dimensional stability under high temperatures is a requirement for the dielectric substrate material as it must survive the electrode deposition process. Excessive shrinkage during metallization would also negatively effect the positive and negative electrode alignment. A high dielectric breakdown voltage is needed to insulate the applied 4 kV differential. Finally, stability of the pad over long periods of adhesion is required for this long-duration temporary anchoring application.

Polyimide (PI) is a common choice in the flex circuit industry and of interest for thin film capacitors due to superior temperature stability, high breakdown resistance, and dielectric constant. However, it was observed during testing that over a period of several hours the performance of a PI film adhesive would degrade under the exposure to a high electric field intensity, leading to breakdown through the film. This motivated a study of alternative materials. Both polyethylene-terephthalate (PET) and polyethylene-naphthalate (PEN) films were demonstrated to serve as viable alternatives. PEN and PET not only showed slightly higher adhesive pressures, but more importantly did not breakdown or measurably degrade during long-term adhesive testing. Polyphenylene sulfide (PPS) films were also identified as a material candidate but was not tested

due to difficulties sourcing the material.

We demonstrated an electrostatic adhesive utilizing PET film of thickness 50 mm, and an anchor with electrode gap size of 50 mm did not experience any dielectric breakdown over the course of a 5 week trial with a 5 kV differential applied across the film. In comparison, previous Kapton based adhesive films would consistently experience dielectric breakdown after a matter of hours. As seen in Table 1, PEN and PET have much lower water absorption rates than PI. We believe this absorbed water may be altering the performance of PI film under extended duration tests. Indeed, prior work using thin films of PI kept samples under a vacuum between manufacture and testing [138]. We therefor use PEN as the dielectric substrate due to this observed qualitative phenomenon.

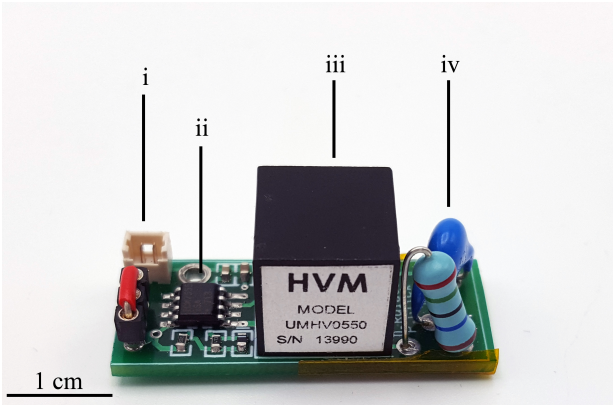



**Figure 4.3**: Switching circuit that enables power saving behavior, by using this circuit the anchoring device consumes one eighth the power. Components include i) battery connector ii) 7555 timer iii) voltage converter iv) high-voltage resistor and capacitor. Neglecting the voltage converter, which would still be required for un-tethered electrostatic systems, the incremental mass and cost of this circuit are 3.1 g and $4.84. The circuit has a footprint of 14.5mm by 36.5mm.

To reduce the power consumption of the electrostatic adhesives by nearly an order of magnitude, we introduce a switching circuit (Fig. 4.3, Fig. 4.4). Electrostatic adhesives rely on electrical charge between two sets of electrodes, but there is no load across this differential, and the only loss of charge comes from leakage current through the dielectric substrate. Despite this, voltage converters continuously draw power to maintain the charge across the electrodes.

As most of the power in an electrostatic anchor is actually consumed by the voltage converter itself, and not the adhesive pad, we may scale the adhesive pad to be larger with a minimal impact on power consumption. We selected a voltage converter with a low no-load power draw (HVM UMHV0550) to partially mitigate this effect. However, to substantially reduce power use of an electrostatic pad, it is necessary to disconnect the voltage converter, while maintaining the charge across the electrodes. Due to the leakage across the dielectric, the voltage converter must still be periodically reconnected to keep the voltage differential sufficiently large for adhesion. We use a low-power 7555 timer (Maxim Integrated) chip to cycle the power supplied to the voltage converter at a set interval. This interval is adjustable through the selection of fixed on-board resistor values (R1 and R2). To protect the thin electrodes from any sudden spikes in voltage associated with switching, a high-voltage resistor is connected in series with the positive electrodes. To increase the allowed off time between cycles, we place a high voltage capacitor, 23 pF, in parallel with the electrodes to maintain charge during the off cycles. For reference, the capacitance of the 54 mm x 60 mm anchor alone is approximated to be around 0.6 pF based on simplified model for IDE's shown in other research [139].

This device uses low-cost, commercially available components while drastically reducing the power usage of electrostatic adhesives. The total cost of the circuit board, and all components except the voltage converter (which would still be required for untethered payloads) is $4.84. The mass of the switching circuit is 7.1 g, but the bulk of this mass is the voltage converter itself (4 g). The footprint of the circuit is 14 mm by 31 mm. The nominal power savings can be modeled by $PS = (t_{off} + t_{on})/t_{on}$. However, because the switching circuit itself draws power, this equation slightly overestimates the true power savings. In the results section, we quantify this discrepancy and find that the true power savings differs minimally from the nominal savings. Importantly, this circuit may service electrostatic adhesives of varying size without need to reconfigure the circuit itself.

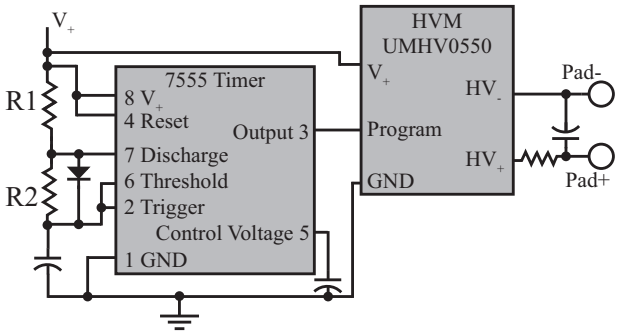



**Figure 4.4**: The circuit diagram for the switching circuit. The circuit outputs a square wave signal to the high-voltage converter. The duty cycle and frequency of the square wave can be controlled by selecting R1 and R2.

### Electrode Geometry

The geometry of the electrodes has a significant impact on electric field strength, and prior work investigated this effect [132] [140]. For this work, we select the electrode geometry of an interdigital electrode comb pattern with a bi-layer adhesive construction. This layout maximizes the area of electrodes coverage for a rectangular anchor, and has been presented in previous work [133]. We use electrodes with a 400 $\mu$m width and a gap of 150 $\mu$m. This width corresponds with the optimal values of 200-400 $\mu$m established in previous work [133] and with manufacturing limitations for the shadow mask used during electrode fabrication. Additionally, previous worked found it advantageous to keep the electrode gap size as small as possible without inducing dielectric breakdown [140]. However, testing showed that an electrode gap size of 50 $\mu$m would lead to shorting after a few hours, establishing a lower bound. As a result a slightly larger electrode gap size was used which sacrificed minimal adhesion performance, around 5%, for improved reliability.

## 4.1.2 Manufacturing

To create the electrode pattern a set of shadow masks are used on top of the base 50 $\mu$m PEN film during the electron beam evaporation process (Fig 4.5 - feature 1). Magnets mount

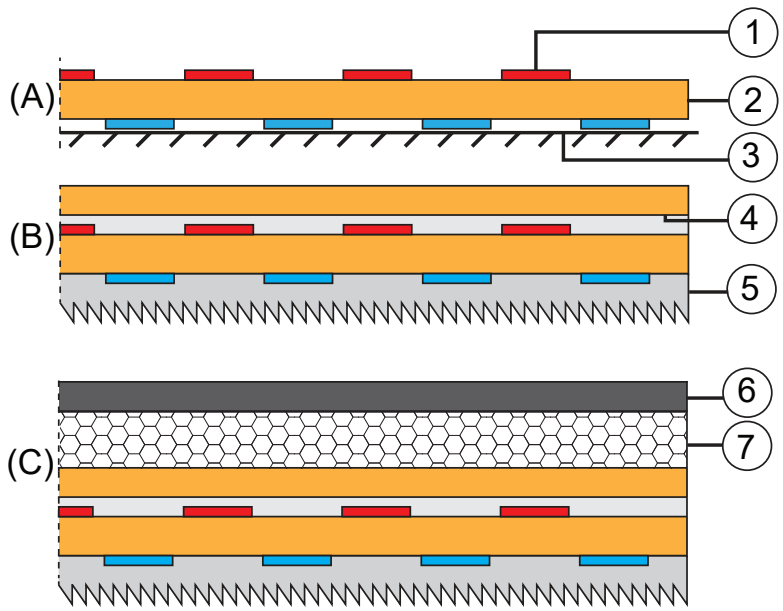



**Figure 4.5**: Primary phases of the fabrication process. A) Complete metal deposition process resulting in the desired electrode pattern on the substrate. B) Insulating the electrodes and adding gecko-inspired adhesive to the front surface completes the adhesive pad. C) The full anchor is completed by adding a foam backing and magnesium plate to promote surface conformation and load distribution. Before application of the backing, the electrostatic film has a total thickness of around 155 mm.

both the substrate (Fig 4.5 - feature 2, DuPont) and shadow masks to a rigid base-plate (Fig 4.5 - feature 3). This process takes several steps, each requires alignment between the mask and substrate, which is made possible with specific optical alignment features designed into the mask itself. These features allow for top/bottom electrode alignment to within less then $\pm 10\ \mu$m.

An additional layer of 25 µm PEN film is applied over the positive electrodes (Fig 4.5 - feature 4) to act as an insulator. A 10 µm thick layer of silicone (Smooth-On MoldStar), used with a bonding primer (PR1200), bonds the two sheets. Additional details for the deposition process and electrode insulation process are described in our previous work [35], and can be seen in Figure 4.5. To add the gecko-inspired surface features (Fig 4.5 - feature 5) we spin coat silicone over a microstructured wax mold and roll the insulated electrode composite onto this surface

before the silicone has cured. This process results in a thin, 155 $\mu$m thick, hybrid adhesive film.

To complete the anchor, two additional elements are needed to help distribute load across the adhesive pad. A sheet of silicone closed cell foam (Fig 4.5 - feature 7, McMaster Carr) is included as a compliant layer behind the electrodes to help the anchor conform to irregularities or protrusions on a surface. The thickness of the foam, 1.5 mm, is thick enough to allow for appreciable displacement of small protrusions, while thin enough to not greatly increase the distance to the center of mass of the payload. Behind the foam, a metal bracket is used to distribute load evenly across the pad (Fig 4.5 - feature 6). The bracket is machined from a magnesium plate to achieve high stiffness and low mass. After this adhesive composite is fabricated, the switching circuit mounts directly at the base of the rigid magnesium backing plate.

### 4.1.3 Electrostatic Anchor Results

All testing described in this section was performed with the 54 mm $\times$ 60 mm anchor at 4 kV, unless otherwise stated.

#### Adhesive Performance

Adhesive force depends on the electrical properties of a given surface and the roughness of the surface. We quantified the adhesive force in the normal direction on several surfaces of interest including drywall, finished wood, glass, and aluminum (see Tab. 4.1). Importantly, there was no shear load applied to the anchor during these tests. The directional gecko-inspired adhesive used provides a negligible effect in the normal direction until a shear load is applied. This test captured the effect of the electrostatic adhesive film, which does not depend on shear load. We applied an increasing load in the normal direction, measured by a digital force gauge (Mark 10 M5-10), and repeated each trial five times. Adhesion depends on the dielectric properties of the target surface, with an observed lowest adhesive pressure on drywall (0.55 kPa) and highest on polyurethane finished wood (1.16 kPa). Furthermore, this normal adhesion load capacity does not represent the

maximum mass of a possible payload, instead it helps react the moment caused by the distance between the wall and the payload center of mass.

**Table 4.1**: Adhesion in the normal direction with no shear load applied to the electrostatic anchor

| Material | Normal Load (N) | Standard Deviation (N) | Adhesive Pressure (kPa) |
|---|---|---|---|
| Drywall | 2.18 | 0.14 | 0.55 |
| Wood | 4.64 | 0.52 | 1.16 |
| Metal | 3.38 | 0.35 | 0.85 |
| Glass | 2.59 | 0.29 | 0.65 |

### Model Validation and Payload Capacity

To validate the model presented in Eq. 4.2 and quantify the torque capacity of the anchor, we took force data at an increasing moment arm to apply a known torque. We applied a force oriented downwards with gravity at a known distance off the wall, increased force until failure, and recorded data using a digital force gauge (Mark 10 M5-10). Each data point represents 6 trials. There is good agreement between the model and experimental results, except at low distances, where the model under-predicts the adhesive force. Electrostatic adhesives provide a maximum shear and normal force, and these two values are largely decoupled and constant. Gecko-inspired adhesives similarly provide a maximum shear and normal force, but the maximum normal force (required to resist a torque applied to the anchor), depends on the shear load. As a payload acts with an increasing moment arm, as represented in Figure 4.6, there is less shear load at failure, which limits the contribution of the gecko-adhesives. The model does not capture this behavior, and at low center of mass distances, the model under-predicted load capacity. If a larger center of mass is required for a given application, but there is a limit on the adhesive pad size, the moment arm of the adhesive pad may be passively increased by adding a long beam at the bottom of the

anchor. This beam shifts the pivot point of the payload, and allows the anchor to apply more torque proportional to this beam length [141].

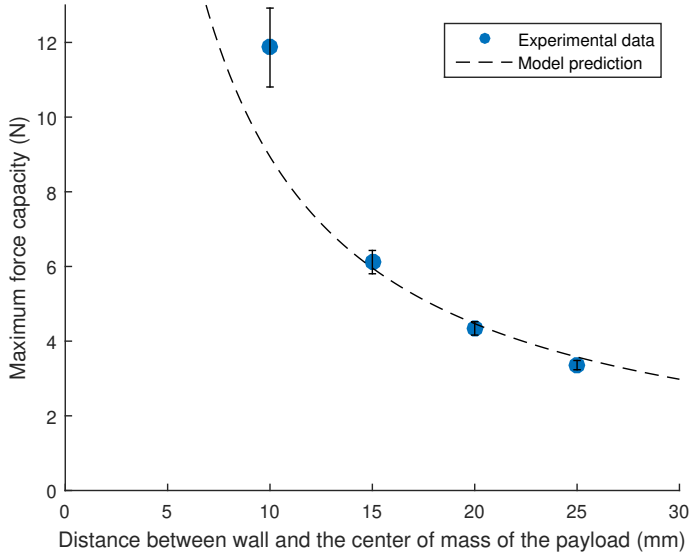



**Figure 4.6**: Impact of the center of mass on the anchor. As the center of mass of the payload increases, the anchor can support decreasing masses.

### Power Savings

For most electrostatic adhesives, power is predominantly consumed by the voltage converter to maintain a high-voltage but no-load power source. We cycle power to the converter, and in doing so are able to consume an order of magnitude less power. However, the components of the switching circuit do consume some power. In Table 3 we compare the power of an all-on adhesive pad, with an adhesive pad powered by the switching circuit running at a 8.3 % duty cycle. Our power supply, a single cell (1s), 350 mAhr lithium polymer battery, supplies a lower voltage than the maximum allowed by the voltage converter. We show that to boost the voltage from a 1s battery to 5 V is inefficient (it more than doubles power consumption but the incremental adhesive force increase is only about 20 %).

**Table 4.2**: Power savings due to switching circuit

| Configuration | Power Consumption (mW) | Energy Consumption (kJ/Day) | Days of adhesion using 350 mAhr battery |
|---|---|---|---|
| Always ON (5V) | 90 | 7.78 | 0.6 |
| Switching (5V) | 17.9 | 1.55 | 3.0 |
| Switching (1s 4V) | 7.5 | 0.65 | 7.2 |

However, the switching behavior does have an impact on adhesive performance. This is likely due to the duration of time without a high-voltage supply to recharge the pad (off time). To increase the power savings, we increase off time. Due to the leakage of charge through the dielectric substrate, the voltage differential between the electrodes decreases during this off time, which reduces the adhesion generated by the pad. This effect is not significant at short off times, and is partially mitigated by a capacitor added in parallel to the adhesive pad. To quantify this effect we measure adhesive strength as a function of the duty cycle of the switching circuit. We record force values with a digital force gauge, and repeat each trial 3 times, loading the pad to failure (Figure 4.7).

The adhesive force is fairly constant for duty cycles above 10%. After this point, depending on the required torque capacity, battery size, and payload configuration, there is a trade-off between power consumption and adhesive performance. It is worth noting that the gecko-inspired adhesive features do not rely on supplied power, and for payloads that are close to the wall, or payloads with a long tails to lengthen the moment arm of the adhesives, the duty cycle may be decreased further to conserve power.

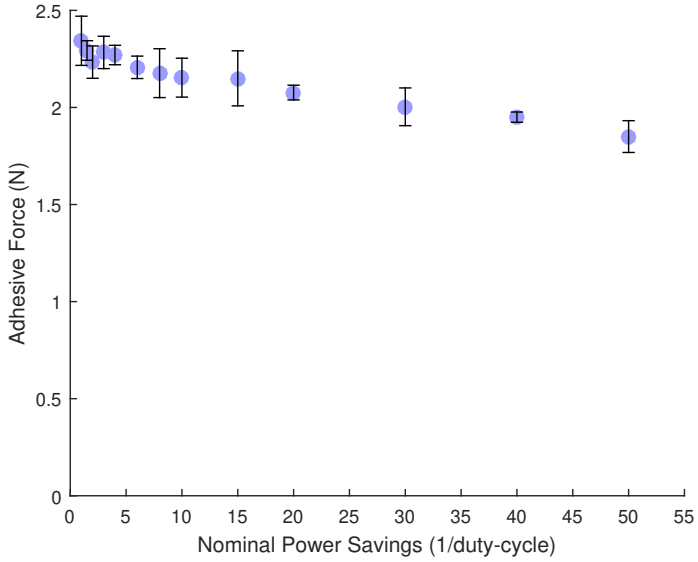



**Figure 4.7**: Impact of switching on adhesive force. As we provide less power to the electrostatic adhesive, the adhesive force of the pad decreases. However, by using 10x less power, the anchor maintains 93% adhesive force.

## 4.2 High Strength Inflatable Pouch Anchors

The shift towards simplicity in mobile robots has resulted in many novel designs, utilizing new materials and manufacturing approaches [142]. Mass is an important parameter for mobile systems that drives design and efficiency. Many robots even avoid metal joints and fixtures which do not scale well to low-mass and small-size platforms [143, 144]. Furthermore, these small mobile systems often generate complex motions with a limited number of controlled degrees-of-freedom (DOF), as each additional actuator consumes power and adds mass to the system [145, 146]. Power consumption, system mass, and operational lifespan are linked through limits on power density. Anchoring for mobile robots is a powerful tool to reduce demands on system power, which is especially important for small, mobile, or flying robots [45]. An anchor can help these systems in two ways– (1) deploying a payload or (2) perching for flying and climbing robots. Since mass tends to limit system performance and since most mobile robots cannot support a high DOF arm, the ideal anchor should be strong, low-power, light-weight, and




**Figure 4.8**: An inflatable anchor that is light weight and easily positioned. (A) Components of the anchoring system include $CO_2$ cartridge (i), pressure regulator (ii), valve (iii), and inflatable pouch (iv). (B) The pouch is easily placed in a wide range of channels when deflated, and conforms to arbitrary surfaces to provide holding force when inflated. (C) We demonstrate the capability of these anchors by holding a human ( $<$ 700 N load) at 105 kPa of internal pressure using a microspine interface.

easy to position.

However, anchoring in an unstructured environment is difficult due to variations in surface features, geometry, and materials. Creating a strong but reversible anchor with an unknown object and no steady-state power consumption is a challenge; especially on a small platform that may only have limited sensing, computation, and communication capabilities. Reversible adhesives such as suction [147], electrostatics [35, 132], gecko-inspired films [58], and electromagnets [148] are possible solutions, but are surface dependent and not well suited for natural surfaces [46, 47, 149]. Parallel jaw or fluid-driven elastomer grippers rely on finding a suitable feature to wrap around or

pinch [40]. Similarly, biologically inspired solutions such as octopus-like continuums [150, 151] or growing robots [60, 61, 108] require features to wrap around. Furthermore, most grippers require strong actuators and a high number of controlled DOF to position, making their suitability for low mass applications limited [43]. Mechanical locks are common for docking and anchoring but typically require known surfaces or mating features [152]. Microspines are another option for adhering to natural surfaces. Microspines are made of arrays of flexures embeded with sharp hooks, and excel at opportunistically engaging small features in natural rock [127, 153]. However, existing applications of microspines rely on complex linkages or actively controlled legs [126, 154]. These solutions help optimize payload on a given surface but their deployment can require a large mass, number of sensors, and computation.

The sport of rock climbing inspires a simpler solution through the use of negative space. Rock climbers frequently use negative space in a wall such as a crack or cavity to create a temporary anchor. The nuts and cams used by these climbers are exceptionally strong supporting loads of up to 10 kN, over 9000 times the weight of the anchor itself. However, these devices are not practical for small robots. Cams and nuts take skill to position and are only suitable for specific sizes of cracks and channels.

We adapt the concept of using negative space, as found in rock climbing, by using soft pressure-driven materials with high-friction interfaces. Pressure-driven soft materials expand to fill the space they occupy and distribute forces over a large area, helping these flexible materials conform to arbitrary shapes [1]. Inflatable pouches are a lightweight technology and have been used in robotic applications as structural linkages [155, 156], and artificial muscles [108, 157, 158]. Industrial applications of inflatable pouches include wedges, leveling tools [159], and medical devices [160]. The process for manufacturing pouch actuators can be automated to achieve the rapid fabrication of complex inflatable structures [157] and low-cost robotic systems [161]. Using soft materials, we designed a low-mass anchor that is easy to position in natural cavities and can hold large forces.

Inflatable pouches made of soft materials are well suited for anchoring in natural surfaces. In this work we designed a strong, low-power, and lightweight anchor. Commercially available compressed carbon dioxide ($CO_2$) canisters can provide high pressure with low mass and a small form factor, eliminating the need for heavy battery-driven pumps. A regulator reduces the pressure in the anchor ($CO_2$ is stored at over 800 PSI) and provides a compromise between maximum anchoring strength and the number of deployments. A three-way normally-closed valve eliminates the need for steady-state electrical power during anchoring. To inflate, the valve can connect the anchor to the $CO_2$ canister, and to release the valve can vent the pressure to atmosphere. Microspines increase the strength of the gripper in shear, further reducing the demands on the internal pressure and initial placement of the pouch. Soft materials help engage the spines by conforming to arbitrary shapes. Though the placement of the anchor and geometry of the cavity do impact strength, the dependence on position for a strong hold is relatively low compared to other anchoring technologies.

Our primary contribution in this paper is the concept of using pressure-driven soft materials as a lightweight and versatile anchor for natural concavities to simplify the placement process of a robotic anchor. We modeled the geometry and payload of these anchors, and integrated a high-friction microspine interface to improve performance. We conducted experiments to validate the models, and show that microspines increase the strength and versatility of these anchors. The integration of $CO_2$ cartridges and electronically controlled valves makes the anchor suitable for robotic application. Finally, we demonstrate the anchor in two sample tasks on land and in water.

### 4.2.1 Design Principles

The size of the anchor and the contact area between the anchor and surface both impact the conditions in which the anchor can operate. Increasing pressure increases the maximum holding force, but reduces the number of cycles the anchor can perform with a fixed supply. We modeled the relationship between pressure and force, and also study how the angle of the channel

can impact holding force.

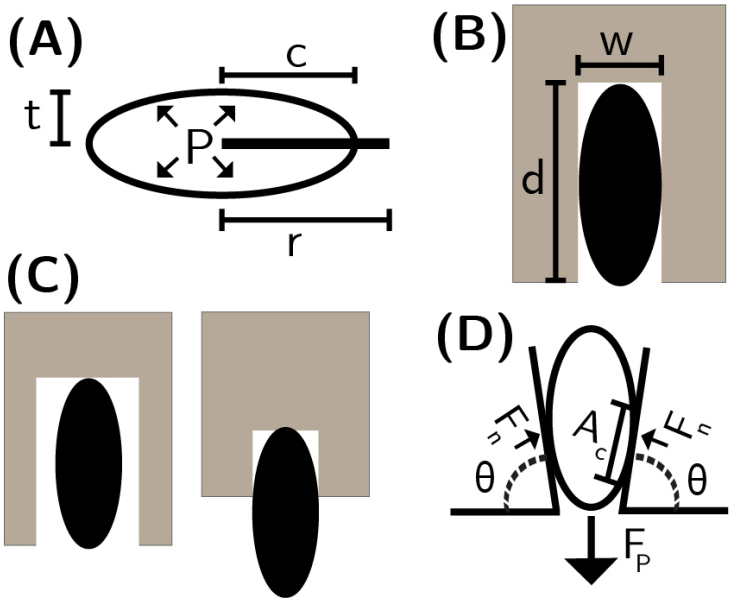



**Figure 4.9**: Schematic of the pouch anchor with an inflated thickness $t$, deflated radius $r$ and inflated radius $c$ (A). (B) To model the anchor we assume channels are smooth with a width $w$ and depth $d$. (C) Channels that are too wide or too shallow are not suitable for anchoring. (D) The taper angle of the channel θ, area in contact between the channel and anchor $A_C$, and internal pressure $P$ can be used to predict the normal force $F_n$ and subsequently the maximum payload $F_P$ of the anchor.

The size of the anchor determines the range of gaps for which it may be a suitable anchor (Fig 2). We used a disk with radius $r$ as the un-inflated shape of the anchor. When pressure is applied to the anchor, it changed shape to increase the internal volume. Pressure works to maximize the internal volume of the shape. Assuming an inextensible membrane, the inflated shape will depends on the geometry of the membrane. For example, an inflated disk takes the shape described by the elliptic integral $f(x)$ [162].

$$f(x) = \int_x^r \frac{t^2}{\sqrt{r^4 - t^4}} dt, \qquad (0 \leq x \leq r) \tag{4.4}$$

The inflated radius $c$, thickness $t$, and volume $V$ are respectively $0.76 \cdot r$ , $0.91 \cdot r$, and $1.219 \cdot r^3$ where $r$ is the radius of the deflated disk [162, 163]. These ratios do not change with varying deflated radii, and neglect boundary effects such as crinkling. Based on this, we can say that the

anchor will only operate in a channel of width up to $0.91 \cdot r$, at which point the anchor will no longer touch both sides of the channel. Furthermore, the anchor will perform best in channels with a depth of at least $0.38 \cdot r$, so that the geometry of the anchor will not push itself out of the channel. These two heuristic constraints place outer limits on the channel dimensions that are suitable for anchoring. However, the maximum load capacity of the anchor will depend on the area in contact between the anchor and surface, which in turn depends on the width of the channel. Since the internal pressure contributes a force proportional to the area in contact $A_c$, the anchor will perform better in narrower channels. Since the membrane is assumed to be inextensible, $A_c$ is independent of the pressure applied, as long as the pressure is larger than the minimum pressure needed to fully inflate the anchor $P_c$. $A_c$ can be found experimentally as function of channel width, $w$ using the nondimensional ratio $w/a$.

We model the maximum payload capacity of the anchor with a static analysis. Assuming the anchor is inflated between two parallel plates with coefficient of friction $\mu$ and with an area of contact $A_c$, the maximum pull force $F_p$ the anchor can support is predicted by equation 4.5. This results from a static analysis and ignores any off-axis loading or deformation in the shape of the anchor. The model predicts an anchor force that increases linearly with internal pressure $P$, motivating the need for an anchor that can hold high pressures.

$$F_p = 2 \cdot P \cdot A_c \cdot \mu \tag{4.5}$$

$$F_p = 2(P \cdot A_c \cdot \mu \cdot \sin(\theta) + P \cdot A_c \cdot \cos(\theta)) \tag{4.6}$$

Though natural surfaces are likely to be irregular in shape, we modelled the effect of the taper angle $\theta$ of a flat, smooth channel (see Fig. 2 D) on the maximum strength of the anchor (Eq. 4.6). It can be seen that for a channel with $\theta < \pi/2$, the force of the internal pressure acts at an angle, pushing the anchor deeper into the channel. This increases the maximum $F_p$. The reverse is true

for $\theta > \pi/2$, decreasing the maximum force. The maximum angle an anchor can operate in can be found when $F_p = 0$ and depends on the coefficient of friction. If $\mu \geq \cot(\theta)$ then the anchor will be able to hold a load $F_p > 0$.

### 4.2.2 Fabrication

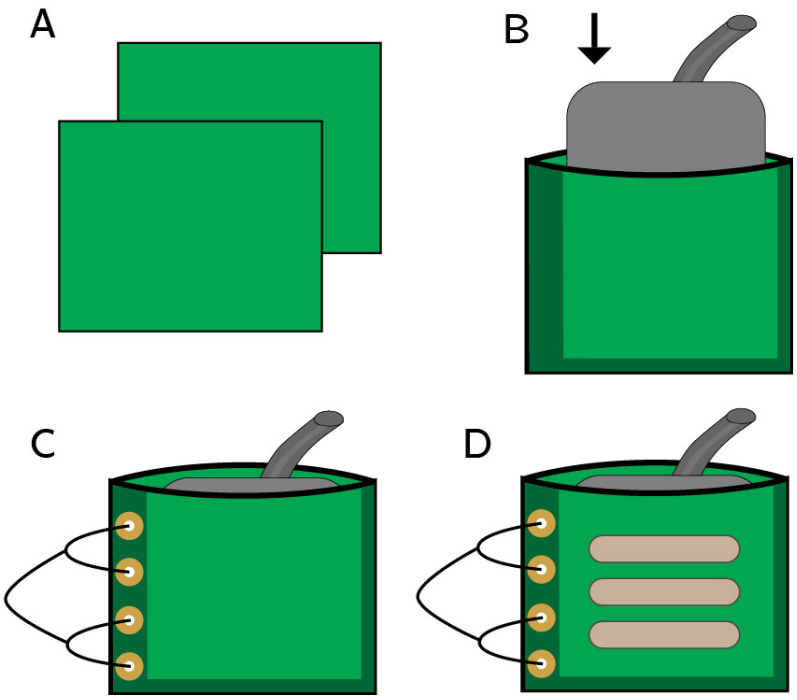



**Figure 4.10**: Fabrication process for an inflatable pouch anchor. (A) heat seal fabric on three sides. (B) Slide in an air-bladder (can then secure the bladder by sealing the fourth side). (C) Add grommets and cables (loadsharing improves strength). (D) High-friction interfaces such as microspine arrays support larger loads.

Fabrication of an inflatable anchor is a simple process but can also be tailored for a variety of conditions. The anchor consisted primarily of a fabric sleeve, inflatable bladder, pressure source, and pneumatic connections. A $CO_2$ cartridge and three-way normally closed valve allowed for repeated autonomous operation with minimal power use— desirable for mobile robots. The four main steps in constructing the anchor are outlined in Fig. 4.10. First, two pieces of heat-sealable fabric (TPU coated Oxford canvas) are sealed together on three sides to make

a sleeve. Alternatively, a single long length can be folded over and sealed on two sides. An inflatable air bladder fit inside this sleeve. We used a commercially available air bladder due to the low cost and ability to withstand pressures over 350 kPa (Air Wedge, Winbag).

Grommets provided a secure mounting point for cables, and reduced the chance of fraying or tearing in the sleeve. We used multiple grommets with load-sharing to reduce stress concentrations. Finally, to improve friction we used microspine arrays comprised of size 20 fishhooks embedded in polyurethane (Vyta-flex, SmoothOn). Three arrays in parallel are bonded to the pouch at their front and back ends, intended to allow for load-sharing between the arrays. The fabrication process for the microspine interface can be seen in Fig. 4.11. An intermediate silicone mold (Moldstar, SmoothOn) is used to cast the polyurethane. Silicone prevents bonding to the polyurethane, and allows for easy and repeated placement of fishhooks.

Our system weighed 425 g in total, mostly due to the pneumatic hardware. The $CO_2$ canister and pressure regulator weighed 180.2 g. The valve weighed 140.4 g. The anchor itself weighed 62 g including the grommets, sleeve, and air bladder. All additional tubing and fittings weighed 42.4 g.

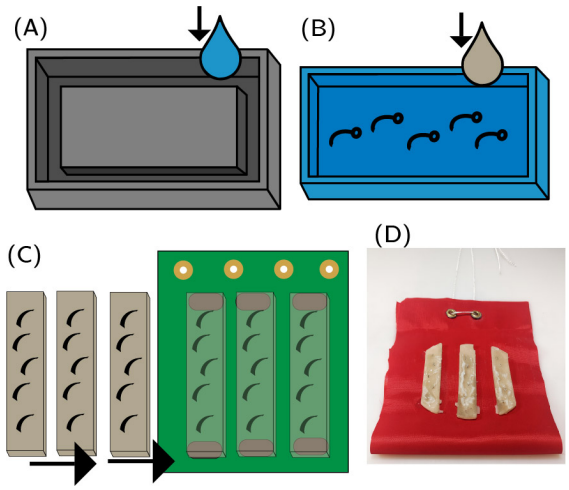



**Figure 4.11**: Fabrication of the microspine arrays. (A) Uncured silicone is added to a 3D printed mold. (B) The silicone is demolded and used to mold the polyurethane. Fishhooks are pressed into the cured silicone so the polyurethane can bond to the back of the hooks. (C) Glue bonds the demolded polyurethane at the top and bottom edges to the fabric sleeve. (D) Photograph of finished product.

### 4.2.3 Pouch Anchor Performance

#### Model Evaluation

Since the force the anchor applies to a channel depends on the area in contact, we studied how that area changes with channel width. In practice, the area in contact will vary depending on the shape of a specific channel so there is inherent uncertainty in the model. We measured the area in contact as a function of channel width, and used this fit to predict force in subsequent tests (Fig. 4.12). We used a non-dimensional ratio of channel width to inflated pouch thickness, and measured area in contact as a percent of total surface area so that this model could be scaled to different sizes. This test was performed in a flat smooth channel, with a 70 mm pouch fully inflated. Since the pouch was inelastic, once it was fully inflated (past $P_c$), the area in contact did not measurably change with increased pressure. The pressure $P_c$ was approximately 25 kPa, so we used a pressure of 35 kPa for the tests in Fig. 4.12 to ensure the pouch was fully inflated. The observed behaviour was well captured by our linear fit.

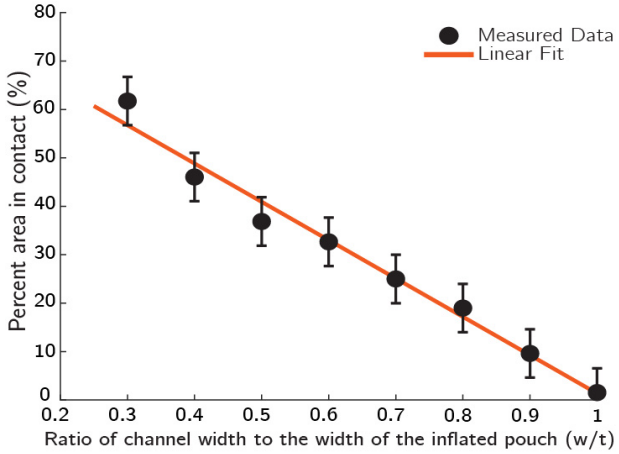



**Figure 4.12**: Non-dimensional experimental model for area in contact between the anchor and surface $A_C$ as a function of channel width. This test is for a smooth and flat plane, and assumes the anchor is fully inflated and inelastic.

he maximum force of the anchor depended linearly on the internal pressure $P$ (Fig. 4.13). Using the linear fit for area in contact and an experimentally measured value of $\mu$, we tested the

anchor at a variety of pressures and compared the results to our model predictions (Fig. 4.13). Though the model assumes $P > P_c$, we began our tests at 10 kPa to show the full range of pull off forces. This test was performed at a channel width to inflated thickness ratio of 0.5 (34 mm) and with the TPU coated fabric sleeve. We tested up to a maximum of 100 kPa, but the pouch and anchor were capable of supporting higher pressures and loads. A laboratory test showed that the air bladder held pressures of over 350 kPa without rupture, suggesting a maximum possible holding-force of over 1 kN.

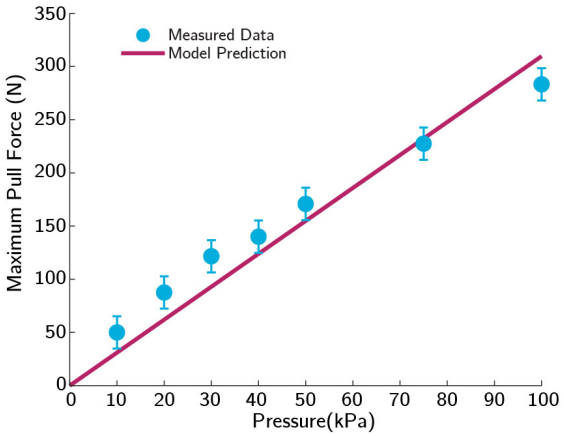



**Figure 4.13**: Maximum load capacity of the anchor as a function of internal pressure.

Since channel width changes the area in contact, we tested the maximum force at different widths, using an internal pressure of 40 kPa (Fig. 4.14). For wide channels, a high internal pressure can compensate for the reduced force. However, increased internal pressure would not be suitable in all cases such as anchoring to fragile rock. Using a larger anchor would improve force in two ways, (1) increasing $A_c$ and (2) increasing the inflated thickness. However, there is a limitation to increasing anchor size. Large anchors cannot penetrate shallow channels so the anchor design must balance width and depth of potential channel geometries.

In unstructured environments, channels ware unlikely to be flat, motivating a study of the impact of channel angle on force capacity. The results of our tests are presented in Fig. 4.15, with a minimum channel width held constant at a ratio of 0.6 (40.8 mm) and internal air pressures

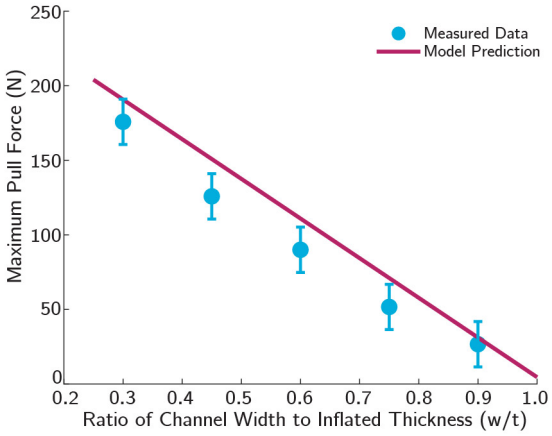



**Figure 4.14**: The width of a channel determines the area in contact and therefore the normal force the anchor exerts outwards.

of 20 and 40 kPa. Depending on the angle of the channel, the resultant normal force vector could act to push the pouch either in or out of the channel. When including the angle, our model (equation 3) under-predicted force at angles above 90 degrees and slightly over-predicted force for angles below 90 degrees. This is likely because of two reasons. The area in contact changes with the angle of the channel. Furthermore the anchor will either compress or expand as it is pulled depending on the angle of the cavity, changing the internal pressure unless connected to the pressure regulator.

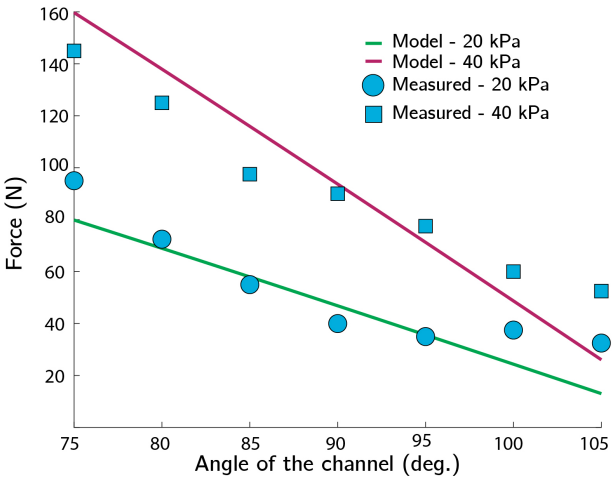



**Figure 4.15**: Maximum force held by anchor as a function of channel angle.

### Materials and Interfaces

One of the most important parameters for the anchoring mechanism is its coefficient of friction against a surface. While higher pressures can increase forces, this comes at a cost of reducing the number of deployments from a fixed supply of $CO_2$ and exerting larger normal forces. In some cases exerting large normal forces is not desirable such as if anchoring to brittle or frangible surfaces. Increasing the coefficient of friction provides the ability to increase force without increasing internal pressure. To validate that the microspine arrays improve friction, we tested the microspine interface on the inflatable anchor and compared the results to the TPU-coated fabric (Fig. 4.16). The width was at a ratio of 0.6 (40.8 mm) and the anchor held an internal pressure of 30 kPa.

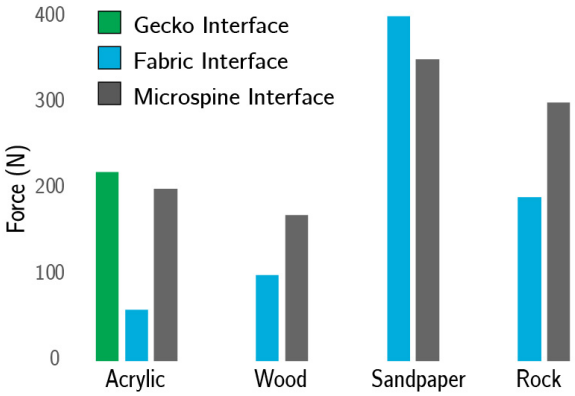



**Figure 4.16**: Anchoring force on different materials. The internal pressure in the pouch was 30 kPa. A demonstration with gecko-inspired adhesive was included on the smooth acrylic. The rock used for this test was a manufactured hard flagstone.

The microspine array performed well in all four tests. Microspines typically provide the greatest performance on hard, porous rock where the spines are able to opportunistically grip available features. However, because internal pressure of the anchor forces the spines against the target surface, the microspines did surprisingly well on featureless but soft surfaces such as acrylic and wood. Inspection of the samples after the trials revealed that the spines slightly dug into the material, improving grip strength. On a hard flagstone, the anchor with microspines

held nearly 300 N, finding some natural features to grip. In the case of 80 grit sandpaper, the fabric held the highest force. Both sandpaper and fabric are engineered materials with structured roughness. We suspect that the grit of the sandpaper interlocked with the fabric fibers to create high friction. The microspines still held over 300 N, but concentrated their force into small areas which increased surface pressure, likely leading to cohesive failure in the sandpaper. Microspine interfaces tend to reduce $A_c$ but increase $\mu$. However on impenetrable surfaces or surfaces with low cohesive strength, microspines will not provide higher friction. A single trial with a gecko-inspired adhesive held 220 N and only failed due the bond between the pouch and adhesive surface.

There are three modes of failure to consider with a pouch anchor in an unstructured environment: 1) insufficient friction between the anchor and the surface, 2) cohesive failure within the surface, and 3) failure in the surface by fracture due to the outward normal force. The selection of the interface mechanism has several implications in regards to the expected type of failure. Friction forces can be increased with additional internal pressure, but this exerts greater normal forces which can fracture thin flakes of rock or damage a delicate surface. Microspines reduce the required internal pressure, but focus the outward force onto a few specific points, increasing the applied pressure. For frangible materials that are more likely to experience cohesive failure, such as sandpaper, this concentration of stress can be a disadvantage. These factors make for interesting design trade-offs between use of pressure, pouch size, and interface material.

**Field Tests and Demonstrations**

Natural rock, with uneven surfaces and irregular angles, can cause deviation from modeled expectations. While laboratory experiments can test different taper angles and coefficients of friction, the variability found in field experiments helped establish more realistic bounds on load-performance and test the effect of anchor-placement. We tested the anchor in three locations, with three trials at each location to get a sense of the deviation possible on natural surfaces. In the

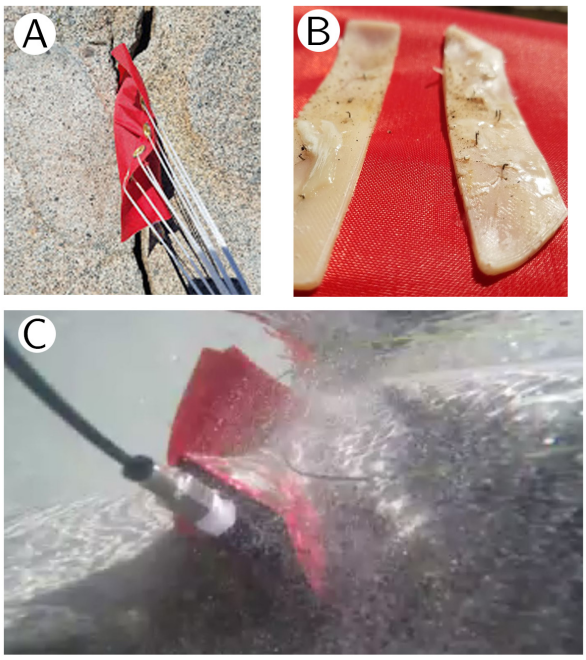



**Figure 4.17**: Field demonstrations for the pouch anchor. (A) Anchor in a natural rock channel. (B) The microspine arrays degraded after multiple tests-to-failure. (C) The anchor is suitable for use under water and could be deployed by ROVs.

second and third trial locations, the deviation between the trials was low, and comparable to the deviation in the laboratory data. Notably the results of the fabric anchor were lower in the natural rock than on the manufactured rock measured in the lab, in particular Table 1- channel 3 can be compared to the rock in Fig. 9. In the field, some channels showed high sensitivity to initial placement, notably in the first test location there was a standard deviation of 108 N. However, the anchor held an average of 350 N so even given the wide range the minimum force was still high. Fig. 4.17-A shows the anchor placed in channel 1. In channel two, we tested the addition of microspines. As expected, microspines increased the anchoring force, but also increased the variance between the trials. The increase in force easily outweighed the additional variance, and all measured trials held more than four times the average force with the fabric sleeve. Our tests showed that even in a wide channel high forces (over 210 N) can be realized through using higher pressures.

Several further demonstrations highlight the capabilities and challenges with the anchor. To demonstrate the high payload capacity of the anchor, we used it to hold a person off of the ground (Fig. 2.13-C). The anchor is intended for robotic applications with lower payloads, but this successful demonstration highlights the ability to scale this anchoring approach. Repeated field tests, often to failure, with the microspine arrays revealed further lessons (Fig. 4.17-B). As the pressure concentrated on a few individual hooks, the polyurethane was not strong enough to keep them in place. This could have been the limiting factor in several pull-out tests. Options to mitigate this problem include using additional hooks to distribute forces more evenly and using stiffer materials to hold the hooks. Finally, we used the anchor underwater off the San Diego coast. The anchor was easily placed since it is not buoyant when deflated. Buoyancy of the device when inflated did not impact anchoring in most cases. Anchoring for ROV's is an important problem since station-keeping can be a significant use of power and is problematic under turbulent conditions.

## 4.3 A low-power, jamming, magnetorheological valve using electropermanent magnets for distributed control in soft robots

Increasing the number of independently controlled actuators in a soft robot can improve dexterity, flexibility, and positional accuracy [1, 2, 47], yet many elastomeric robots consist of only a few actuated degrees of freedom. Each fluidic actuator requires additional infrastructure (tubing, power, valving, and control) to facilitate independent control. The complexity and size of this additional infrastructure has prohibited the use of many (e.g. $O(10)$ to $O(100)$) discrete actuators in a single robot, limiting their use to relatively simple behaviors [164].

There are two ways to achieve independent control of many fluidic elastomer actuators.

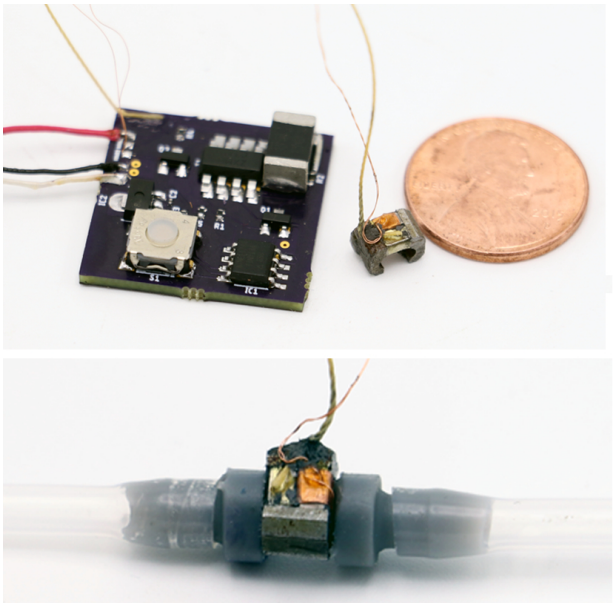


**Figure 4.18**: A small, low-power, magnetorheological valve. The electropermanent magnet weighs only 0.476 g. The magnet is comprised of an alnico magnet wrapped in copper wire, adjacent to a neodymium magnet, between two iron end caps. A small circuit can drive several of the magnets, and it takes no power to hold the OPEN or CLOSED state (top). This magnet can be placed around a constriction, outside of the flow, to create a valve that holds 415 kPa. We use custom fittings with internal constrictions for our valves (bottom).

The first method is to use a larger manifold off-board from, or at the base of, the robot while running a line of tubing to each actuator [165]. Using a manifold may not be suitable for mobile or small robots [5, 142]. Furthermore, there is a fundamental trade-off as more fluid lines are added. Large fluid tubes allow for fast flow of fluid, however when bundled become bulky and stiff. Small diameter fluid tubes are less bulky, but resist flow and result in a large ratio of material to flow cross-section. As more segments are added, the design is pushed further towards small diameter tubes, until they eventually become impractically small. This conflict suggests a second approach to controlling independent soft actuators: distributed local valves. These distributed valves can branch off from a few relatively large supply lines to increase flow rate and save both weight and space. When extra segments are added to the end of the robot, it results in no change to the properties of the base of the robot. This approach would be preferable for soft robots using many actuators, and has clear biological analogs such as the precapillary sphincters in the

human vascular system, which allow for control of blood flow to specific areas of the body while maintaining only a few high pressure arteries. [166].

Efforts to design soft robots with distributed valving have succeeded in producing multi-segmented designs with novel behavior [167–170]. However, with any un-tethered robot or when many valves are distributed along a robot, issues such as mass, size, price, complexity, and power become paramount [45, 125, 142]. The range of existing approaches to valving illustrates this need, with actuators designed using pressure-actuated soft membrane valves [171–173], electrorheological fluid valves [174–176], and commercially available pneumatic solenoid valves [169,170]. Pressure driven valves require additional pressure lines for controlling the valve. These valves can be multiplexed to drive a greater number of valves than the number of control lines. However, these valves are difficult to distribute across a soft robot and multiplexing alleviates but does not solve the issues introduced by having to integrate large bundles of tubes into the robot [2]. Commercially available pneumatic valves do not scale well due to size, power consumption, and price [169, 170]. Electrorheological fluid valves are a compelling solution, but require high activation voltages (i.e. $\sim$kVs), consume power continuously, and require tight constrictions in their flow path that adversely effect fluid flow rate [177]. An ideal valve is small, simple to control, low mass, low cost, and low power. Magnetorheological fluid (MRF) valves use a smart material, similar to electrorheological fluid valves, but are able to operate at lower voltages and with larger orifices. MRF valves have not previously been explored for use in soft robots. Traditional magnetorheological fluid (MRF) valves require $\sim 1\,\mathrm{W} - 100\,\mathrm{W}$ of power in order to maintain their state using conventional electromagnets, limiting their utility in mobile applications.

### 4.3.1 Design of a Magnetorheological Valve

#### Magnetorheological Fluid

Magnetorheological fluid is comprised of two primary components: iron particles and a carrier fluid such as mineral oil or silicone oil. Optional additives such as surfactants and detergents can also be added to enhance MRF properties. With no magnetic field applied, the iron particles remain in suspension and flow past each other, with minimal interference, allowing the fluid to flow, behaving as a slightly shear thinning liquid. When a background field is applied, the iron particles align to the field and form chains, which resist flow. In the magnetized state, MRF can be modeled as a Bingham plastic, solid up to a critical yield shear stress and flowing like a fluid above that yield stress. Previous works have used MRF for variable stiffness devices, shock absorption, and even robotic grasping and climbing [178–180]. The yield stress of MRF increases with magnetic field strength until saturating, at which point increasing the magnetic field does not significantly increase the yield stress. The maximum yield stress for MRF is $\sim$100 kPa, at saturation of $\sim$700-1000 mT. For typical MRF valve designs, when the magnetic field is turned on, the flow will be stopped at pressure below the yield stress and will begin to flow above the yield stress. The maximum holding pressure for an MRF valve based on this yield stress is therefore limited to about $\sim$100 kPa of pressure, and requires a strong magnetic field to realize these pressures [181].

Granular flows, such as in an MRF, are subject to a behavior known as jamming. When a suspension jams, the particles form a stable dome across the passage, mechanically stopping the flow of the grains and carrier fluid (Figure 4.19) [182]. In most applications jamming is avoided, as it can lead to irreversible stoppages. However with MRF, it is possible to design a valve around the formation of jams that can be induced, and reversed reliably by the addition and removal of a magnetic field [183]. Jamming behavior is appealing in our application as we do not require flow modulation and it requires a smaller magnetic field density for a given holding pressure, allowing

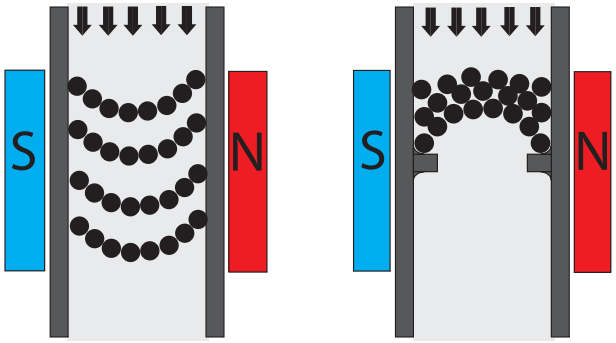



**Figure 4.19**: Constriction behavior for the valve. Traditional MRF valve, left, forms chains across the magnetic field, which need to be broken to flow, resulting in a Bingham Plastic behavior, stable below and flowing above a critical yield strength. Right, a jamming valve forms stable arches across a restriction under pressure, increasing pressure further jams and stabilizes the structure.

us to use smaller magnets, and actuate with higher pressures than we would be able to with a shear valve.

The choice of the carrier fluid will change the viscosity, thermal properties, and conductivity of the MRF. If the carrier fluid is too inviscid the iron will quickly settle out of suspension. If the carrier fluid is too viscous, flow rate will be unacceptably low. For this application, thermal and electrical properties are not relevant, so we used mineral oil as our carrier fluid due to its advantageous viscosity characteristics and low cost.

Increasing the volume percentage and size of the iron particles increases the yield stress, the fluid viscosity, probability of jamming, and the magnetic permeability of the MRF. A successful MRF valve requires a fluid that jams reliably, unjams consistently, and maintains a sufficient flow rate for robot actuation. We test several mass percentages and particle sizes to experimentally select between these variables. Furthermore, additives may be used to change the magnetorheological behavior, such as the the off-state viscosity, and settling time of the fluid. Surfactants, such as oleic acid (used in this work), act to disperse iron particles by attaching to the grains at the hydrophilic end of the molecule, while pulling the grains into suspension with the lipophilic end. The result is that even a very small volume fraction of oleic acid drastically reduces the unmagnetized viscosity for a given iron fraction. We test fluids with and without oleic acid.

**Electro-permanent Magnet**

We fabricated electropermanent magnets similar to that presented by Gilpin et. al. and by Knaian [184, 185]. EPMs, used to replace conventional electromagnets in MRF valves, allow for a latching valve that consumes no steady state power in either the open or closed state. EPMs have a permanent neodymium magnet adjacent to an aluminum-nickel-cobalt (alnico) magnet sandwiched between two iron end caps. The alnico magnet is wrapped in thin gauge wire and connected to an H-bridge circuit that can drive current in either direction through the wire (Figure 4.18). The alnico magnet has a much lower coercivity than the neodymium magnet, allowing it to be magnetized by a short current pulse, while the neodymium magnet is unaffected. The remnant field for alnico 5 and N42 neodymium magnets are very similar $\sim 1.3\,\mathrm{T}$, so when fully magnetized, the two magnets are roughly equal strength. If the alnico magnet is magnetized parallel to the neodymium magnet, their field lines both exit the magnets through the north poles, travel up into the iron end cap, then down to the other end cap and up into the south pole of the magnets. When the alnico magnet is magnetized anti-parallel to the neodymium magnet, the field lines travel up from the north pole of the neodymium magnet, into the iron end, then back down through the south pole of the alnico magnet, into the other end cap, and back into the neodymium magnet. The field lines don't escape from the end caps, and so there are no external magnetic fields (Figure 4.20). The alnico magnets in our work are wrapped in 80 turns of 42 gauge magnet wire. The alnico and neodymium magnet, both $1.6\times1.6\times3.2\,\mathrm{mm}$, are sandwiched between iron end caps, adjacent to each other, and bonded with cyano-acrylate adhesive. Excluding the control circuit, the EPM is $4\times4\times6\,\mathrm{mm}$, 0.476 g, and costs $7.32 USD per device at quantity 100 (Figure 4.18). Switching the state of the alnico magnet is done through a $100\,\mu\mathrm{s}$ pulse, which has a maximum power of $\sim 150\,\mathrm{W}$ and uses $\sim 10\,\mathrm{mJ}$ of energy.

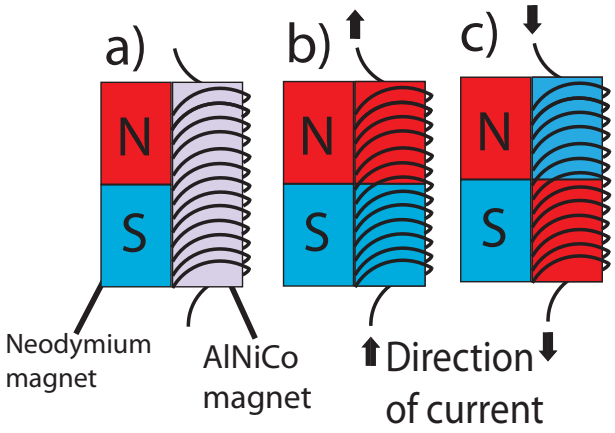



**Figure 4.20**: The behavior of an electropermanent magnet. The neodymium magnet has a permanent orientation. However, the alnico can be magnetized via a short burst of current to have its field either aligned with (b) or opposed to (c) the neodymium magnet. By realigning the alnico magnet, the EPM can be switched to either have a strong external magnetic field (b) or a negligible external magnetic field (c), and will hold this state with no quiescent power draw.

### Control Circuit

The control board is dual layered and populated using SMT components for space savings. A strain-relief cable (Yellow Spectra thread) is bonded between the EPM assembly and control circuit to protect the fragile magnet wire during testing. Our prototype control circuit switches a single magnet per board and consists of an H-bridge, a large tank capacitor, two gate drive BJTs, an ATTiny13 microcontroller, a voltage regulator, and a tactile switch, which, including the board, cost $6.73. The board is $22\times22\times6$ mm. The largest individual component is the capacitor (Board top right), which stores the energy required to switch the EPM on the board, allowing for thinner gauge wires to supply power to the board and charge the capacitor with a low current. The next largest component is the tactile switch (Board bottom left), which is only necessary for the prototype boards for manual actuation (Figure 4.18). The number of valves to be controlled per board, and therefore the valve size including control board, depends on the valve configuration and placement, and can be tailored for a particular application.

**Constrictions**

For both non-jamming and jamming valves, the geometry of the passage can affect the performance of the valve. In the case of a yielding valve, a constriction in the valve prevents the fluid from sliding along the non-magnetic walls of the passage, reducing the holding force, instead creating a plug of solidified material that must yield through the constriction in order to flow. A jamming probability/time to jam is a function of the ratio of constriction diameter to particle diameter. Jams typically only spontaneously occur, with no magnetic field applied, when constrictions are less than around $5\times$ the diameter of the particles [182]. The magnetic field interaction with the MRF reduces the effective diameter of the constriction, while also increasing the cohesion of the grains, allowing jams to occur with larger constriction diameters [183]. An ideal valve will have the maximum constriction diameter that still allows for induced jamming, ensuring that the jam will clear when the magnet is turned off, and improving the OPEN flow rate. The constrictions were 3D printed (FormLabs) and are sized to have openings with 20, 30, and 40 times the maximum diameter of the largest 325 mesh iron particles (0.88, 1.32, 1.76 mm respectively). We confirmed the aperture size using pin gauges as there is some inherent inaccuracy with printing, and only performed tests with valves that were within 0.05 mm of the nominal size.

### 4.3.2 Demonstration in a Soft Robot

We constructed a two segment soft robot, where each segment is comprised of two antagonistic actuators. The actuators have an internal volume of 10.8 $cm^3$, weigh 17.8 g when empty, and weigh 43.42 g when full of Mix 3 in the unactuated (straight) state. We printed our soft actuators using a SLA printer (Carbon3D, Sil-30) then assembled four actuators into a single continuum, bonding the actuators with an adhesive (SilPoxy). Each segment can bend 180 deg in either direction when actuated to 140 kPa using air. However, due to the density of the MRF,

the robot was not able to reach this full range of motion when actuated with MRF as it did not have enough torque to counteract the weight of the fluid. We individually controlled two of the actuators in the robot using MRF valves, showing unique shape generation (4.21). It took 250 seconds to fully pressurize an actuator [186].

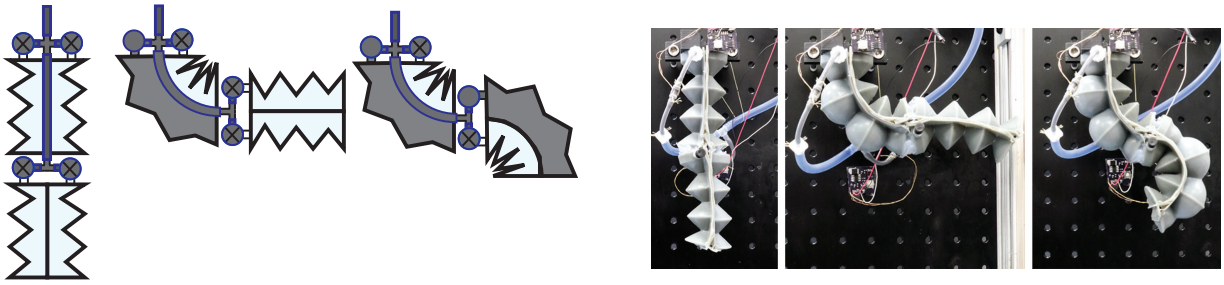


**Figure 4.21**: A demonstration using MRF to drive a 2 segment, 4 actuator soft robotic appendage. With a 140 kPa pressure source applied we control individual valves along the robot to change shape. It takes 250 seconds to pressurize these large actuators volume.

## 4.4 Acknowledgements

This work was carried out at the University of California, San Diego, and at the Jet Propulsion Laboratory, California Institute of Technology, under contract with the National Aeronautics and Space Administration, and sponsored by the U.S. Government. P.E. Glick Is supported by a NASA Space Technology Research Fellowship.

Chapter 4, in part, is a reprint of material abbreviated from IEEE Robotics and Automation Letters 2020. Glick, Paul E.; Drotman, Dylan; Ruffatto III, Donald; Tolley, Michael T. The dissertation author was the primary investigator and author of this paper.

Chapter 4, in part, is a reprint of material abbreviated from IEEE Robotics and Automation Letters 2018. Ruffatto III, Donald; Glick, Paul E.; Tolley, Michael T.; Parness, Aaron. The dissertation author contributed to this paper.

Chapter 4, in part, is a reprint of material abbreviated from Smart Materials and Structures 2020. Leps, Thomas; Glick, Paul E.; Ruffatto III, Donald; Parness, Aaron; Tolley, Michael T.;

Hartzell, Christine. The dissertation author was the co-primary investigator and author of this paper.

# Chapter 5

# Conclusions

This thesis studies the use of compliant design for embodied intelligence for extreme environments. By limiting the need for actuation and simplifying control, it will be easier to send robotic agents to more remote and harsher conditions. In this work we show simple robots with only a single controlled degree of freedom, capable of enabling complex biologically inspired behaviors. These systems include grippers supporting up to forty five pounds and conforming to arbitrarily shaped objects and growing vine robots capable of navigating tortuous passageways.

Though this work builds towards capable mechanical intelligence for extreme environments, it is worth briefly considering how it relates to the field of machine learning. It may seem that these two topics are contrasting, one focused on building capable hardware and the other focused on using simple hardware in more adept ways. However, the link between the brain and the body is essential in biological systems and may prove to be similarly important in robotics. Consider the task of building a gripper that can ”grip anything”. Currently researchers are focusing on using machine learning with simple grippers to learn how to position and move the end effector to achieve success. Using a more capable gripper with gecko-inspired adhesive will extend the capabilities of the end effector to either support more load or decrease the dependence on part orientation. Ideally, these two approaches could be combined and with an appropriate

simulator or training method to learn how to use the more capable gripper most effectively. Similarly, though the growing vine robot was designed to operate in open-loop, adding further control inputs and training the robot how to move within a set of unknown environments could lead to improvements in operation.

Furthermore, we study the application of compliant robots for extreme environments, yet many of the materials used are not suitable for these harsh conditions. Despite this conflict, many of the approaches taken may be readily translated into more robust designs. For example, both under-actuated grippers rely on the same principles and so it is possible to select the specific design based on the intended environment. Similarly, the growing robots hold promise for space applications, but rather than inflatable sleeves, may rely on deployable composite booms.

# Bibliography


[1] D. Rus and M. T. Tolley, "Design, fabrication and control of soft robots," *Nature*, vol. 521, no. 7553, p. 467, 2015.

[2] P. Polygerinos, N. Correll, S. A. Morin, B. Mosadegh, C. D. Onal, K. Petersen, M. Cianchetti, M. T. Tolley, and R. F. Shepherd, "Soft robotics: Review of fluid-driven intrinsically soft devices; manufacturing, sensing, control, and applications in human-robot interaction," *Advanced Engineering Materials*, vol. 19, no. 12, pp. 1700016–n/a, 2017. 1700016.

[3] M. T. Tolley, R. F. Shepherd, B. Mosadegh, K. C. Galloway, M. Wehner, M. Karpelson, R. J. Wood, and G. M. Whitesides, "A resilient, untethered soft robot," *Soft Robotics*, vol. 1, no. 3, pp. 213–223, 2014.

[4] R. F. Shepherd, F. Ilievski, W. Choi, S. A. Morin, A. A. Stokes, A. D. Mazzeo, X. Chen, M. Wang, and G. M. Whitesides, "Multigait soft robot," *Proceedings of the National Academy of Sciences*, vol. 108, no. 51, pp. 20400–20403, 2011.

[5] D. Drotman, S. Jadhav, M. Karimi, M. T. Tolley, *et al.*, "3d printed soft actuators for a legged robot capable of navigating unstructured terrain," in *Robotics and Automation (ICRA), 2017 IEEE International Conference on*, pp. 5532–5538, IEEE, 2017.

[6] K. C. Galloway, K. P. Becker, B. Phillips, J. Kirby, S. Licht, D. Tchernov, R. J. Wood, and D. F. Gruber, "Soft robotic grippers for biological sampling on deep reefs," *Soft robotics*, vol. 3, no. 1, pp. 23–33, 2016.

[7] F. Ilievski, A. D. Mazzeo, R. F. Shepherd, X. Chen, and G. M. Whitesides, "Soft robotics for chemists," *Angewandte Chemie*, vol. 123, no. 8, pp. 1930–1935, 2011.

[8] B. Shih, D. Drotman, C. Christianson, Z. Huo, R. White, H. I. Christensen, and M. T. Tolley, "Custom soft robotic gripper sensor skins for haptic object visualization," in *2017 IEEE/RSJ International Conference on Intelligent Robots and Systems (IROS)*, pp. 494–501, Sept 2017.

[9] Y.-L. Park, B.-R. Chen, and R. J. Wood, "Design and fabrication of soft artificial skin using embedded microchannels and liquid conductors," *IEEE Sensors Journal*, vol. 12, no. 8, pp. 2711–2718, 2012.

[10] A. Atalay, V. Sanchez, O. Atalay, D. M. Vogt, F. Haufe, R. J. Wood, and C. J. Walsh, "Batch fabrication of customizable silicone-textile composite capacitive strain sensors for human motion tracking," *Advanced Materials Technologies*, vol. 2, no. 9, 2017.

[11] S. Ozel, N. A. Keskin, D. Khea, and C. D. Onal, "A precise embedded curvature sensor module for soft-bodied robots," *Sensors and Actuators A: Physical*, vol. 236, pp. 349–356, 2015.

[12] H. Zhao, K. O'Brien, S. Li, and R. F. Shepherd, "Optoelectronically innervated soft prosthetic hand via stretchable optical waveguides," *Sci. Robot.*, vol. 1, no. 1, p. eaai7529, 2016.

[13] C. T. O'Neill, N. S. Phipps, L. Cappello, S. Paganoni, and C. J. Walsh, "A soft wearable robot for the shoulder: Design, characterization, and preliminary testing," in *Rehabilitation Robotics (ICORR), 2017 International Conference on*, pp. 1672–1678, IEEE, 2017.

[14] C. Majidi, "Soft robotics: a perspective—current trends and prospects for the future," *Soft Robotics*, vol. 1, no. 1, pp. 5–11, 2014.

[15] A. D. Marchese, R. K. Katzschmann, and D. Rus, "A recipe for soft fluidic elastomer robots," *Soft Robotics*, vol. 2, no. 1, pp. 7–25, 2015.

[16] B. Mosadegh, P. Polygerinos, C. Keplinger, S. Wennstedt, R. F. Shepherd, U. Gupta, J. Shim, K. Bertoldi, C. J. Walsh, and G. M. Whitesides, "Pneumatic networks for soft robotics that actuate rapidly," *Advanced Functional Materials*, vol. 24, no. 15, pp. 2163–2170, 2014.

[17] S. Terryn, J. Brancart, D. Lefeber, G. Van Assche, and B. Vanderborght, "Self-healing soft pneumatic robots," *Science Robotics*, vol. 2, no. 9, p. eaan4268, 2017.

[18] H. Lipson, "Challenges and opportunities for design, simulation, and fabrication of soft robots," *Soft Robotics*, vol. 1, no. 1, pp. 21–27, 2014.

[19] H. K. Yap, H. Y. Ng, and C.-H. Yeow, "High-force soft printable pneumatics for soft robotic applications," *Soft Robotics*, vol. 3, no. 3, pp. 144–158, 2016.

[20] E. W. Hawkes, D. L. Christensen, A. K. Han, H. Jiang, and M. R. Cutkosky, "Grasping without squeezing: Shear adhesion gripper with fibrillar thin film," in *Robotics and Automation (ICRA), 2015 IEEE International Conference on*, pp. 2305–2312, IEEE, 2015.

[21] K. Autumn, M. Sitti, Y. A. Liang, A. M. Peattie, W. R. Hansen, S. Sponberg, T. W. Kenny, R. Fearing, J. N. Israelachvili, and R. J. Full, "Evidence for van der waals adhesion in gecko setae," *Proc Natl Acad Sci USA*, vol. 99, no. 19, pp. 12252–6, 2002.

[22] D. L. Christensen, E. W. Hawkes, S. A. Suresh, K. Ladenheim, and M. R. Cutkosky, "$\mu$tugs: Enabling microrobots to deliver macro forces with controllable adhesives," in *Robotics and Automation (ICRA), 2015 IEEE International Conference on*, pp. 4048–4055, IEEE, 2015.

[23] K. Autumn, A. Dittmore, D. Santos, M. Spenko, and M. Cutkosky, "Frictional adhesion: a new angle on gecko attachment," *Journal of Experimental Biology*, vol. 209, no. 18, pp. 3569–3579, 2006.

[24] D. Santos, M. Spenko, A. Parness, S. Kim, and M. Cutkosky, "Directional adhesion for climbing: theoretical and practical considerations," *Journal of Adhesion Science and Technology*, vol. 21, no. 12-13, pp. 1317–1341, 2007.

[25] E. Brown, N. Rodenberg, J. Amend, A. Mozeika, E. Steltz, M. R. Zakin, H. Lipson, and H. M. Jaeger, "Universal robotic gripper based on the jamming of granular material," *Proceedings of the National Academy of Sciences*, vol. 107, no. 44, pp. 18809–18814, 2010.

[26] J. N. Israelachvili, "Intermolecular and surface forces," 2011.

[27] A. Parness, D. Soto, N. Esparza, N. Gravish, M. Wilkinson, K. Autumn, and M. Cutkosky, "A microfabricated wedge-shaped adhesive array displaying gecko-like dynamic adhesion, directionality and long lifetime," *Journal of the Royal Society, Interface*, Mar 2009.

[28] L. Ge, S. Sethi, L. Ci, P. M. Ajayan, and A. Dhinojwala, "Carbon nanotube-based synthetic gecko tapes," *Proceedings of the National Academy of Sciences*, vol. 104, no. 26, pp. 10792–10795, 2007.

[29] H. E. Jeong, J.-K. Lee, H. N. Kim, S. H. Moon, and K. Y. Suh, "A nontransferring dry adhesive with hierarchical polymer nanohairs," *Proc Natl Acad Sci USA*, vol. 106, no. 14, pp. 5639–44, 2009.

[30] S. Gorb, M. Varenberg, A. Peressadko, and J. Tuma, "Biomimetic mushroom-shaped fibrillar adhesive microstructure," *Journal of The Royal Society Interface*, vol. 4, pp. 271–275, Oct 2006.

[31] D. Sameoto and B. Ferguson, "Robust large-area synthetic dry adhesives," *Journal of Adhesion Science and Technology*, vol. 28, no. 3-4, pp. 337–353, 2014.

[32] M. P. Murphy, B. Aksak, and M. Sitti, "Gecko-inspired directional and controllable adhesion," *Small*, vol. 5, no. 2, pp. 170–175, 2009.

[33] P. Day, E. V. Eason, N. Esparza, D. Christensen, and M. Cutkosky, "Microwedge machining for the manufacture of directional dry adhesives," *Journal of Micro and Nano-Manufacturing*, vol. 1, no. 1, p. 011001, 2013.

[34] H. Jiang, E. W. Hawkes, C. Fuller, M. A. Estrada, S. A. Suresh, N. Abcouwer, A. K. Han, S. Wang, C. J. Ploch, A. Parness, and M. R. Cutkosky, "A robotic device using gecko-inspired adhesives can grasp and manipulate large objects in microgravity," *Science Robotics*, vol. 2, no. 7, p. eaan4545, 2017.

[35] E. W. Schaler, D. Ruffatto, P. Glick, V. White, and A. Parness, "An electrostatic gripper for flexible objects," in *2017 IEEE/RSJ International Conference on Intelligent Robots and Systems (IROS)*, pp. 1172–1179, Sept 2017.

[36] S. Song, D.-M. Drotlef, C. Majidi, and M. Sitti, "Controllable load sharing for soft adhesive interfaces on three-dimensional surfaces," *Proceedings of the National Academy of Sciences*, p. 201620344, 2017.

[37] A. Parness, N. Abcouwer, C. Fuller, N. Wiltsie, J. Nash, and B. Kennedy, "Lemur 3: A limbed climbing robot for extreme terrain mobility in space," pp. 5467–5473, 2017.

[38] A. Parness, "Testing gecko-like adhesives aboard the international space station," in *AIAA SPACE and Astronautics Forum and Exposition*, p. 5181, 2017.

[39] S. Hirose and Y. Umetani, "The development of soft gripper for the versatile robot hand," *Mechanism and machine theory*, vol. 13, no. 3, pp. 351–359, 1978.

[40] A. Billard and D. Kragic, "Trends and challenges in robot manipulation," *Science*, vol. 364, no. 6446, 2019.

[41] B. B. Reed, R. C. Smith, B. J. Naasz, J. F. Pellegrino, and C. E. Bacon, "The restore-l servicing mission," in *AIAA SPACE 2016*, p. 5478, 2016.

[42] H. Jiang, E. W. Hawkes, C. Fuller, M. A. Estrada, S. A. Suresh, N. Abcouwer, A. K. Han, S. Wang, C. J. Ploch, A. Parness, *et al.*, "A robotic device using gecko-inspired adhesives can grasp and manipulate large objects in microgravity," *Sci. Robot.*, vol. 2, p. eaan4545, 2017.

[43] S. Levine, P. Pastor, A. Krizhevsky, J. Ibarz, and D. Quillen, "Learning hand-eye coordination for robotic grasping with deep learning and large-scale data collection," *The International Journal of Robotics Research*, vol. 37, no. 4-5, pp. 421–436, 2018.

[44] D. Wang, D. Tseng, P. Li, Y. Jiang, M. Guo, M. Danielczuk, J. Mahler, J. Ichnowski, and K. Goldberg, "Adversarial grasp objects,"

[45] D. Ruffatto, P. E. Glick, M. T. Tolley, and A. Parness, "Long-duration surface anchoring with a hybrid electrostatic and gecko-inspired adhesive," *IEEE Robotics and Automation Letters*, vol. 3, pp. 4201–4208, Oct 2018.

[46] E. W. Hawkes, H. Jiang, D. L. Christensen, A. K. Han, and M. R. Cutkosky, "Grasping without squeezing: Design and modeling of shear-activated grippers," *IEEE Transactions on Robotics*, vol. 34, no. 2, pp. 303–316, 2017.

[47] P. Glick, S. Suresh, D. Ruffatto III, M. Cutkosky, M. T. Tolley, and A. Parness, "A soft robotic gripper with gecko-inspired adhesive," *IEEE Robotics and Automation Letters*, 2018.

[48] L. Birglen, T. Laliberté, and C. M. Gosselin, *Underactuated robotic hands*, vol. 40. Springer, 2007.

[49] H. Nakanishi and K. Yoshida, "The tako (target collaborativize) flyer: a new concept for future satellite servicing," in *Smaller Satellites: Bigger Business?*, pp. 397–399, Springer, 2002.

[50] M. G. Catalano, G. Grioli, E. Farnioli, A. Serio, C. Piazza, and A. Bicchi, "Adaptive synergies for the design and control of the pisa/iit softhand," *The International Journal of Robotics Research*, vol. 33, no. 5, pp. 768–782, 2014.

[51] B. Massa, S. Roccella, M. C. Carrozza, and P. Dario, "Design and development of an underactuated prosthetic hand," in *Proceedings 2002 IEEE International Conference on Robotics and Automation (Cat. No. 02CH37292)*, vol. 4, pp. 3374–3379, IEEE, 2002.

[52] L. U. Odhner, L. P. Jentoft, M. R. Claffee, N. Corson, Y. Tenzer, R. R. Ma, M. Buehler, R. Kohout, R. D. Howe, and A. M. Dollar, "A compliant, underactuated hand for robust manipulation," *The International Journal of Robotics Research*, vol. 33, no. 5, pp. 736–752, 2014.

[53] D. M. Aukes, B. Heyneman, J. Ulmen, H. Stuart, M. R. Cutkosky, S. Kim, P. Garcia, and A. Edsinger, "Design and testing of a selectively compliant underactuated hand," *The International Journal of Robotics Research*, vol. 33, no. 5, pp. 721–735, 2014.

[54] J. Hughes, U. Culha, F. Giardina, F. Guenther, A. Rosendo, and F. Iida, "Soft manipulators and grippers: a review," *Frontiers in Robotics and AI*, vol. 3, p. 69, 2016.

[55] J. Shintake, V. Cacucciolo, D. Floreano, and H. Shea, "Soft robotic grippers," *Advanced Materials*, vol. 30, no. 29, p. 1707035, 2018.

[56] S. Song and M. Sitti, "Soft grippers using micro-fibrillar adhesives for transfer printing," *Advanced Materials*, vol. 26, no. 28, pp. 4901–4906, 2014.

[57] J.-P. Roberge, W. Ruotolo, V. Duchaine, and M. Cutkosky, "Improving industrial grippers with adhesion-controlled friction," *IEEE Robotics and Automation Letters*, vol. 3, no. 2, pp. 1041–1048, 2018.

[58] A. Parness, D. Soto, N. Esparza, N. Gravish, M. Wilkinson, K. Autumn, and M. Cutkosky, "A microfabricated wedge-shaped adhesive array displaying gecko-like dynamic adhesion, directionality and long lifetime," *Journal of the Royal Society Interface*, pp. rsif–2009, 2009.

[59] L. Birglen and C. M. Gosselin, "Force analysis of connected differential mechanisms: Application to grasping," *The International Journal of Robotics Research*, vol. 25, no. 10, pp. 1033–1046, 2006.

[60] E. W. Hawkes, L. H. Blumenschein, J. D. Greer, and A. M. Okamura, "A soft robot that navigates its environment through growth," *Science Robotics*, vol. 2, no. 8, p. eaan3028, 2017.

[61] J. Luong, P. Glick, A. Ong, M. S. deVries, S. Sandin, E. W. Hawkes, and M. T. Tolley, "Eversion and retraction of a soft robot towards the exploration of coral reefs," in *2019 2nd IEEE International Conference on Soft Robotics (RoboSoft)*, pp. 801–807, IEEE, 2019.

[62] P. E. Glick, N. Van Crey, M. T. Tolley, and D. Ruffatto, "Robust capture of unknown objects with a highly under-actuated gripper," in *2020 IEEE International Conference on Robotics and Automation (ICRA)*, pp. 3996–4002, IEEE, 2020.

[63] M. L. Reaka-Kudla, "The global biodiversity of coral reefs: a comparison with rain forests," *Biodiversity II: Understanding and protecting our biological resources*, vol. 2, p. 551, 1997.

[64] L. Plaisance, M. J. Caley, R. E. Brainard, and N. Knowlton, "The diversity of coral reefs: what are we missing?," *PLoS One*, vol. 6, no. 10, p. e25026, 2011.

[65] J. M. Pandolfi, S. R. Connolly, D. J. Marshall, and A. L. Cohen, "Projecting coral reef futures under global warming and ocean acidification," *science*, vol. 333, no. 6041, pp. 418–422, 2011.

[66] R. N. Ginsburg, "Geological and biological roles of cavities in coral reefs," *Perspectives on coral reefs. Australian Institute of Marine Science, Townsville*, pp. 148–153, 1983.

[67] M. Depczynski and D. R. Bellwood, "The role of cryptobenthic reef fishes in coral reef trophodynamics," *Marine Ecology Progress Series*, vol. 256, pp. 183–191, 2003.

[68] J. M. de Goeij and F. C. Van Duyl, "Coral cavities are sinks of dissolved organic carbon (doc)," *Limnology and Oceanography*, vol. 52, no. 6, pp. 2608–2617, 2007.

[69] J. M. De Goeij, D. Van Oevelen, M. J. Vermeij, R. Osinga, J. J. Middelburg, A. F. de Goeij, and W. Admiraal, "Surviving in a marine desert: the sponge loop retains resources within coral reefs," *Science*, vol. 342, no. 6154, pp. 108–110, 2013.

[70] I. C. Enochs, L. T. Toth, V. W. Brandtneris, J. C. Afflerbach, and D. P. Manzello, "Environmental determinants of motile cryptofauna on an eastern pacific coral reef," *Marine Ecology Progress Series*, vol. 438, pp. 105–118, 2011.

[71] M. Kramer, D. Bellwood, and O. Bellwood, "Benthic crustacea on coral reefs: a quantitative survey," *Marine Ecology Progress Series*, vol. 511, pp. 105–116, 2014.

[72] S. R. Scheffers, J. de Goeij, F. C. van Duyl, and R. P. Bak, "The cave-profiler: a simple tool to describe the 3-d structure of inaccessible coral reef cavities," *Coral Reefs*, vol. 22, no. 1, pp. 49–53, 2003.

[73] M. Wunsch and C. Richter, "The cavecam—an endoscopic underwater videosystem for the exploration of cryptic habitats," *Marine ecology progress series*, pp. 277–282, 1998.

[74] C. Richter, M. Wunsch, M. Rasheed, I. KoÈtter, and M. I. Badran, "Endoscopic exploration of red sea coral reefs reveals dense populations of cavity-dwelling sponges," *Nature*, vol. 413, no. 6857, p. 726, 2001.

[75] J. M. Friesen, P. Glick, M. Fanton, P. Manovi, A. Xydes, T. Bewley, and V. Sunspiral, "The second generation prototype of a duct climbing tensegrity robot, ducttv2," in *Robotics and Automation (ICRA), 2016 IEEE International Conference on*, pp. 2123–2128, IEEE, 2016.

[76] M. S. Verma, A. Ainla, D. Yang, D. Harburg, and G. M. Whitesides, "A soft tube-climbing robot," *Soft robotics*, vol. 5, no. 2, pp. 133–137, 2018.

[77] J. Yuh, "Design and control of autonomous underwater robots: A survey," *Autonomous Robots*, vol. 8, no. 1, pp. 7–24, 2000.

[78] L. H. Blumenschein, A. M. Okamura, and E. W. Hawkes, "Modeling of bioinspired apical extension in a soft robot," in *Conference on Biomimetic and Biohybrid Systems*, pp. 522–531, Springer, 2017.

[79] Z. M. Hammond, N. S. Usevitch, E. W. Hawkes, and S. Follmer, "Pneumatic reel actuator: Design, modeling, and implementation," in *2017 IEEE International Conference on Robotics and Automation (ICRA)*, pp. 626–633, May 2017.

[80] A. Sadhegi, A. Tonazzini, L. Popova, and B. Mazzolai, "A novel growing device inspired by plant root soil penetration behaviors," in *PLOS ONE*, vol. 9, 2014.

[81] I. W. SCUDAMORE, B. C. DUNPHY, and I. D. COOKE, "Outpatient falloposcopy; intra-luminal imaging of the fallopian tube by trans-uterine fibre-optic endoscopy as an outpatient procedure," *BJOG: An International Journal of Obstetrics & Gynaecology*, vol. 99, no. 10, pp. 829–835, 1992.

[82] T. Rosch, A. Adler, H. Pohl, E. Wettschureck, M. Koch, B. Wiedenmann, and N. Hoepffner, "A motor-driven single-use colonoscope controlled with a hand-held device: A feasibility study in volunteers," vol. 67, pp. 1139–1146, 2008.

[83] P. Polygerinos, N. Correll, S. A. Morin, B. Mosadegh, C. D. Onal, K. Petersen, M. Cianchetti, M. T. Tolley, and R. F. Shepherd, "Soft robotics: Review of fluid-driven intrinsically soft devices; manufacturing, sensing, control, and applications in human-robot interaction," *Advanced Engineering Materials*, 2017.

[84] J. D. Greer, T. K. Morimoto, A. M. Okamura, and E. W. Hawkes, "Series pneumatic artificial muscles (spams) and application to a soft continuum robot," in *Robotics and Automation (ICRA), 2017 IEEE International Conference on*, pp. 5503–5510, IEEE, 2017.

[85] W. Fichter, "A theory for inflated thin-wall cylindrical beams," 1966.

[86] C. Wielgosz and J.-C. Thomas, "An inflatable fabric beam finite element," *International Journal for Numerical Methods in Biomedical Engineering*, vol. 19, no. 4, pp. 307–312, 2003.

[87] Y. He and W. Chen, "Experiment and theoretical analysis study of etfe inflatable tubes," *International Journal of Aerospace Engineering*, vol. 2014, 2014.

[88] R. Comer and S. Levy, "Deflections of an inflated circular-cylindrical cantilever beam," *AIAA journal*, vol. 1, no. 7, pp. 1652–1655, 1963.

[89] V. A. Lubarda, "The mechanics of belt friction revisited," *International Journal of Mechanical Engineering Education*, vol. 42, no. 2, pp. 97–112, 2014.

[90] M. L. Euler, "Remarques sur l'effect du frottement dans l'equilibre," *Mem. Acad. Sci*, vol. 18, pp. 265–278, 1762.

[91] A. Davids, "Urban search and rescue robots: from tragedy to technology," *IEEE Intelligent systems*, vol. 17, no. 2, pp. 81–83, 2002.

[92] K. Ebadi, Y. Chang, M. Palieri, A. Stephens, A. Hatteland, E. Heiden, A. Thakur, N. Funabiki, B. Morrell, S. Wood, *et al.*, "Lamp: Large-scale autonomous mapping and positioning for exploration of perceptually-degraded subterranean environments," in *2020 IEEE International Conference on Robotics and Automation (ICRA)*, pp. 80–86, IEEE, 2020.

[93] C. E. Parcheta, C. A. Pavlov, N. Wiltsie, K. C. Carpenter, J. Nash, A. Parness, and K. L. Mitchell, "A robotic approach to mapping post-eruptive volcanic fissure conduits," *Journal of Volcanology and Geothermal Research*, vol. 320, pp. 19–28, 2016.

[94] R. D. Ballard, L. E. Stager, D. Master, D. Yoerger, D. Mindell, L. L. Whitcomb, H. Singh, and D. Piechota, "Iron age shipwrecks in deep water off ashkelon, israel," *American Journal of Archaeology*, pp. 151–168, 2002.

[95] P. Berthet-Rayne, S. Sadati, G. Petrou, N. Patel, S. Giannarou, D. R. Leff, and C. Bergeles, "Mammobot: A miniature steerable soft growing robot for early breast cancer detection," *IEEE Robotics and Automation Letters*, 2021.

[96] M. Li, R. Obregon, J. J. Heit, A. Norbash, E. W. Hawkes, and T. K. Morimoto, "Vine catheter for endovascular surgery," *IEEE Transactions on Medical Robotics and Bionics*, 2021.

[97] K. Otsu, S. Tepsuporn, R. Thakker, T. S. Vaquero, J. A. Edlund, W. Walsh, G. Miles, T. Heywood, M. T. Wolf, and A.-A. Agha-Mohammadi, "Supervised autonomy for communication-degraded subterranean exploration by a robot team," in *2020 IEEE Aerospace Conference*, pp. 1–9, IEEE, 2020.

[98] E. Krotkov, D. Hackett, L. Jackel, M. Perschbacher, J. Pippine, J. Strauss, G. Pratt, and C. Orlowski, "The darpa robotics challenge finals: Results and perspectives," *Journal of Field Robotics*, vol. 34, no. 2, pp. 229–240, 2017.

[99] S. Sabet, A.-A. Agha-Mohammadi, A. Tagliabue, D. S. Elliott, and P. E. Nikravesh, "Rollocopter: An energy-aware hybrid aerial-ground mobility for extreme terrains," in *2019 IEEE Aerospace Conference*, pp. 1–8, IEEE, 2019.

[100] M. M. Coad, L. H. Blumenschein, S. Cutler, J. A. R. Zepeda, N. D. Naclerio, H. El-Hussieny, U. Mehmood, J.-H. Ryu, E. W. Hawkes, and A. M. Okamura, "Vine robots: Design, teleoperation, and deployment for navigation and exploration," *IEEE Robotics & Automation Magazine*, vol. 27, no. 3, pp. 120–132, 2019.

[101] T. K. Morimoto and A. M. Okamura, "Design of 3-d printed concentric tube robots," *IEEE Transactions on Robotics*, vol. 32, no. 6, pp. 1419–1430, 2016.

[102] A. Sadeghi, A. Mondini, and B. Mazzolai, "Toward self-growing soft robots inspired by plant roots and based on additive manufacturing technologies," *Soft robotics*, vol. 4, no. 3, pp. 211–223, 2017.

[103] L. H. Blumenschein, M. Koehler, N. S. Usevitch, E. W. Hawkes, D. C. Rucker, and A. M. Okamura, "Geometric solutions for general actuator routing on inflated-beam soft growing robots," *arXiv preprint arXiv:2006.06117*, 2020.

[104] S. Wang, R. Zhang, D. A. Haggerty, N. D. Naclerio, and E. W. Hawkes, "A dexterous tip-extending robot with variable-length shape-locking," in *2020 IEEE International Conference on Robotics and Automation (ICRA)*, pp. 9035–9041, IEEE, 2020.

[105] J. D. Greer, L. H. Blumenschein, R. Alterovitz, E. W. Hawkes, and A. M. Okamura, "Robust navigation of a soft growing robot by exploiting contact with the environment," *The International Journal of Robotics Research*, vol. 39, no. 14, pp. 1724–1738, 2020.

[106] D. A. Haggerty, N. D. Naclerio, and E. W. Hawkes, "Characterizing environmental interactions for soft growing robots," in *2019 IEEE/RSJ International Conference on Intelligent Robots and Systems (IROS)*, pp. 3335–3342, IEEE, 2019.

[107] I. Taylor, K. Lehner, E. McCaskey, N. Nirmal, Y. Ozkan-Aydin, M. Murray-Cooper, R. Jain, E. W. Hawkes, P. C. Ronald, D. I. Goldman, *et al.*, "Mechanism and function of root circumnutation," *Proceedings of the National Academy of Sciences*, vol. 118, no. 8, 2021.

[108] J. D. Greer, T. K. Morimoto, A. M. Okamura, and E. W. Hawkes, "A soft, steerable continuum robot that grows via tip extension," *Soft robotics*, vol. 6, no. 1, pp. 95–108, 2019.

[109] Y. Satake, A. Takanishi, and H. Ishii, "Novel growing robot with inflatable structure and heat-welding rotation mechanism," *IEEE/ASME Transactions on Mechatronics*, vol. 25, no. 4, pp. 1869–1877, 2020.

[110] M. Selvaggio, L. Ramirez, N. Naclerio, B. Siciliano, and E. Hawkes, "An obstacle-interaction planning method for navigation of actuated vine robots," in *2020 IEEE International Conference on Robotics and Automation (ICRA)*, pp. 3227–3233, IEEE, 2020.

[111] S.-G. Jeong, M. M. Coad, L. H. Blumenschein, M. Luo, U. Mehmood, J. H. Kim, A. M. Okamura, and J.-H. Ryu, "A tip mount for transporting sensors and tools using soft growing robots,"

[112] A. Ataka, T. Abrar, F. Putzu, H. Godaba, and K. Althoefer, "Model-based pose control of inflatable eversion robot with variable stiffness," *IEEE Robotics and Automation Letters*, vol. 5, no. 2, pp. 3398–3405, 2020.

[113] I. Exarchos, B. H. Do, F. Stroppa, M. M. Coad, A. M. Okamura, and C. K. Liu, "Task-specific design optimization and fabrication for inflated-beam soft robots with growable discrete joints," *arXiv preprint arXiv:2103.04942*, 2021.

[114] R. Jitosho, N. Agharese, A. Okamura, and Z. Manchester, "A dynamics simulator for soft growing robots," *arXiv preprint arXiv:2011.01917*, 2020.

[115] L. H. Blumenschein, L. T. Gan, J. A. Fan, A. M. Okamura, and E. W. Hawkes, "A tip-extending soft robot enables reconfigurable and deployable antennas," *IEEE Robotics and Automation Letters*, vol. 3, no. 2, pp. 949–956, 2018.

[116] P. E. Glick, D. Drotman, D. Ruffatto, and M. T. Tolley, "High strength inflatable pouch anchors," *IEEE Robotics and Automation Letters*, vol. 5, no. 3, pp. 3761–3767, 2020.

[117] S. Panda and N. P. Padhy, "Comparison of particle swarm optimization and genetic algorithm for facts-based controller design," *Applied soft computing*, vol. 8, no. 4, pp. 1418–1427, 2008.

[118] M. Mitchell, *An introduction to genetic algorithms*. MIT press, 1998.

[119] A. A. Amiri Moghadam, S. Alaie, S. Deb Nath, M. Aghasizade Shaarbaf, J. K. Min, S. Dunham, and B. Mosadegh, "Laser cutting as a rapid method for fabricating thin soft pneumatic actuators and robots," *Soft robotics*, vol. 5, no. 4, pp. 443–451, 2018.

[120] J. P. Grotzinger, J. Crisp, A. R. Vasavada, R. C. Anderson, C. J. Baker, R. Barry, D. F. Blake, P. Conrad, K. S. Edgett, B. Ferdowski, *et al.*, "Mars science laboratory mission and science investigation," *Space science reviews*, vol. 170, no. 1-4, pp. 5–56, 2012.

[121] R. A. Holman, K. L. Brodie, and N. J. Spore, "Surf zone characterization using a small quadcopter: Technical issues and procedures," *IEEE Transactions on Geoscience and Remote Sensing*, vol. 55, no. 4, 2017.

[122] T. Smith, J. Barlow, M. Bualat, T. Fong, C. Provencher, H. Sanchez, and E. Smith, "Astrobee: A new platform for free-flying robotics on the international space station," 2016.

[123] S. Karumanchi, K. Edelberg, I. Baldwin, J. Nash, J. Reid, C. Bergh, J. Leichty, K. Carpenter, M. Shekels, M. Gildner, *et al.*, "Team robosimian: Semi-autonomous mobile manipulation at the 2015 darpa robotics challenge finals," *Journal of Field Robotics*, vol. 34, no. 2, pp. 305–332, 2017.

[124] M. Plooij, G. Mathijssen, P. Cherelle, D. Lefeber, and B. Vanderborght, "Lock your robot: A review of locking devices in robotics," *IEEE Robotics & Automation Magazine*, vol. 22, no. 1, pp. 106–117, 2015.

[125] M. Fanton, P. Glick, J. Bruce, K. Caluwaerts, J. Friesen, and V. Sunspiral, "Robust and efficient multistage braking system for cable driven robots,"

[126] A. Parness, N. Abcouwer, C. Fuller, N. Wiltsie, J. Nash, and B. Kennedy, "Lemur 3: A limbed climbing robot for extreme terrain mobility in space," in *Robotics and Automation (ICRA), 2017 IEEE International Conference on*, pp. 5467–5473, IEEE, 2017.

[127] A. Parness, "Anchoring foot mechanisms for sampling and mobility in microgravity," in *Robotics and Automation (ICRA), 2011 IEEE International Conference on*, pp. 6596–6599, IEEE, 2011.

[128] A. Curtis, M. Martone, and A. Parness, "Roving on ice: Field testing an ice screw end effector and sample collection tool," *IEEE Aerospace Conference*, March 2018.

[129] A. Parness, A. Willig, A. Berg, M. Shekels, V. Arutyunov, C. Dandino, and B. Kennedy, "A microspine tool: Grabbing and anchoring to boulders on the asteroid redirect mission," in *Aerospace Conference, 2017 IEEE*, pp. 1–10, IEEE, 2017.

[130] L. Briones, P. Bustamante, and M. A. Serna, "Wall-climbing robot for inspection in nuclear power plants," in *Robotics and Automation, 1994. Proceedings., 1994 IEEE International Conference on*, pp. 1409–1414, IEEE, 1994.

[131] S. Kim, M. Spenko, S. Trujillo, B. Heyneman, D. Santos, and M. R. Cutkosky, "Smooth vertical surface climbing with directional adhesion," *IEEE Transactions on robotics*, vol. 24, no. 1, pp. 65–74, 2008.

[132] D. Ruffatto, A. Parness, and M. Spenko, "Improving controllable adhesion on both rough and smooth surfaces with a hybrid electrostatic/gecko-like adhesive," *Journal of The Royal Society Interface*, vol. 11, no. 93, p. 20131089, 2014.

[133] M. Dadkhah, D. Ruffatto, Z. Zhao, and M. Spenko, "Increasing adhesion via a new electrode design and improved manufacturing in electrostatic/microstructured adhesives," *Journal of Electrostatics*, vol. 91, pp. 48–55, 2018.

[134] A. Yamamoto, T. Nakashima, and T. Higuchi, "Wall climbing mechanisms using electrostatic attraction generated by flexible electrodes," in *Micro-NanoMechatronics and Human Science, 2007. MHS'07. International Symposium on*, pp. 389–394, IEEE, 2007.

[135] J. Shintake, S. Rosset, B. Schubert, D. Floreano, and H. Shea, "Versatile soft grippers with intrinsic electroadhesion based on multifunctional polymer actuators," *Advanced Materials*, vol. 28, no. 2, pp. 231–238, 2016.

[136] M. Graule, P. Chirarattananon, S. Fuller, N. Jafferis, K. Ma, M. Spenko, R. Kornbluh, and R. Wood, "Perching and takeoff of a robotic insect on overhangs using switchable electrostatic adhesion," *Science*, vol. 352, no. 6288, pp. 978–982, 2016.

[137] D. Ruffatto, D. Beganovic, A. Parness, and M. Spenko, "Experimental results of a controllable electrostatic/gecko-like adhesive on space materials," in *Aerospace Conference, 2014 IEEE*, pp. 1–7, IEEE, 2014.

[138] N. Lu, X. Wang, Z. Suo, and J. Vlassak, "Metal films on polymer substrates stretched beyond 50%," *Applied Physics Letters*, vol. 91, no. 22, p. 221909, 2007.

[139] V. Tsouti, C. Boutopoulos, I. Zergioti, and S. Chatzandroulis, "Capacitive microsystems for biological sensing," *Biosensors and Bioelectronics*, vol. 27, no. 1, pp. 1 – 11, 2011.

[140] D. Ruffatto, J. Shah, and M. Spenko, "Increasing the adhesion force of electrostatic adhesives using optimized electrode geometry and a novel manufacturing process," *Journal of Electrostatics*, vol. 72, no. 2, pp. 147 – 155, 2014.

[141] K. Carpenter, N. Wiltsie, and A. Parness, "Rotary microspine rough surface mobility," *IEEE/ASME Transactions on Mechatronics*, vol. 21, no. 5, pp. 2378–2390, 2016.

[142] S. I. Rich, R. J. Wood, and C. Majidi, "Untethered soft robotics," *Nature Electronics*, vol. 1, no. 2, p. 102, 2018.

[143] R. J. Wood, "The first takeoff of a biologically inspired at-scale robotic insect," *IEEE transactions on robotics*, vol. 24, no. 2, pp. 341–347, 2008.

[144] D. Rus and M. T. Tolley, "Design, fabrication and control of origami robots," *Nature Reviews Materials*, vol. 3, no. 6, p. 101, 2018.

[145] F. Zuliani, C. Liu, J. Paik, and S. M. Felton, "Minimally actuated transformation of origami machines," *IEEE Robotics and Automation Letters*, vol. 3, no. 3, pp. 1426–1433, 2018.

[146] S.-J. Kim, D.-Y. Lee, G.-P. Jung, and K.-J. Cho, "An origami-inspired, self-locking robotic arm that can be folded flat," *Science Robotics*, vol. 3, no. 16, p. eaar2915, 2018.

[147] J. Mahler, M. Matl, X. Liu, A. Li, D. Gealy, and K. Goldberg, "Dex-net 3.0: Computing robust vacuum suction grasp targets in point clouds using a new analytic model and deep learning," in *2018 IEEE International Conference on Robotics and Automation (ICRA)*, pp. 1–8, IEEE, 2018.

[148] L. Kelley, S. Ostovari, A. B. Burmeister, K. A. Talke, N. Pezeshkian, A. Rahimi, A. B. Hart, and H. G. Nguyen, "Design and experimental validation of a simple controller for a multi-segment magnetic crawler robot," in *Unmanned Systems Technology XVII*, vol. 9468, p. 94680N, International Society for Optics and Photonics, 2015.

[149] J. A. Sandoval, S. Jadhav, H. Quan, D. D. Deheyn, and M. T. Tolley, "Reversible adhesion to rough surfaces both in and out of water, inspired by the clingfish suction disc," *Bioinspiration & biomimetics*, 2019.

[150] C. Laschi, M. Cianchetti, B. Mazzolai, L. Margheri, M. Follador, and P. Dario, "Soft robot arm inspired by the octopus," *Advanced Robotics*, vol. 26, no. 7, pp. 709–727, 2012.

[151] R. V. Martinez, J. L. Branch, C. R. Fish, L. Jin, R. F. Shepherd, R. M. Nunes, Z. Suo, and G. M. Whitesides, "Robotic tentacles with three-dimensional mobility based on flexible elastomers," *Advanced materials*, vol. 25, no. 2, pp. 205–212, 2013.

[152] M. Nilsson, "Connectors for self-reconfiguring robots," *IEEE/ASME Transactions on mechatronics*, vol. 7, no. 4, pp. 473–474, 2002.

[153] A. T. Asbeck, S. Kim, M. R. Cutkosky, W. R. Provancher, and M. Lanzetta, "Scaling hard vertical surfaces with compliant microspine arrays," *The International Journal of Robotics Research*, vol. 25, no. 12, pp. 1165–1179, 2006.

[154] M. J. Spenko, G. C. Haynes, J. Saunders, M. R. Cutkosky, A. A. Rizzi, R. J. Full, and D. E. Koditschek, "Biologically inspired climbing with a hexapedal robot," *Journal of Field Robotics*, vol. 25, no. 4-5, pp. 223–242, 2008.

[155] S. Sanan, J. B. Moidel, and C. G. Atkeson, "Robots with inflatable links," in *2009 IEEE/RSJ International Conference on Intelligent Robots and Systems*, pp. 4331–4336, Oct 2009.

[156] J. R. Bemfica, C. Melchiorri, L. Moriello, G. Palli, and U. Scarcia, "A three-fingered cable-driven gripper for underwater applications," in *2014 IEEE International Conference on Robotics and Automation (ICRA)*, pp. 2469–2474, May 2014.

[157] R. Niiyama, D. Rus, and S. Kim, "Pouch motors: Printable/inflatable soft actuators for robotics," in *Robotics and Automation (ICRA), 2014 IEEE International Conference on*, pp. 6332–6337, IEEE, 2014.

[158] S. Li, D. M. Vogt, D. Rus, and R. J. Wood, "Fluid-driven origami-inspired artificial muscles," *Proceedings of the National Academy of Sciences*, vol. 114, no. 50, pp. 13132–13137, 2017.

[159] R. S. Schubert and R. P. Donker, "Leveling and positioning system and method," Mar.6 2018. US Patent 9,909,867.

[160] P. Howard, E. Howard, and S. Walker, "Movable inflatable anchor for medical devices," Apr.13 2006. US Patent App. 11/149,433.

[161] C. Liu and S. M. Felton, "A self-folding robot arm for load-bearing operations," in *Intelligent Robots and Systems (IROS), 2017 IEEE/RSJ International Conference on*, pp. 1979–1986, IEEE, 2017.

[162] W. H. Paulsen, "What is the shape of a mylar balloon?," *The American mathematical monthly*, vol. 101, no. 10, pp. 953–958, 1994.

[163] M. Mladenov, "On the geometry of the mylar balloon," *Comptes Rendus de l'Academie Bulgare des Sciences*, vol. 54, no. 9, pp. 9–39, 2001.

[164] M. Wehner, M. T. Tolley, Y. Mengüç, Y.-L. Park, A. Mozeika, Y. Ding, C. Onal, R. F. Shepherd, G. M. Whitesides, and R. J. Wood, "Pneumatic energy sources for autonomous and wearable soft robotics," *Soft Robotics*, vol. 1, no. 4, pp. 263–274, 2014.

[165] B. Mosadegh, A. D. Mazzeo, R. F. Shepherd, S. A. Morin, U. Gupta, I. Z. Sani, D. Lai, S. Takayama, and G. M. Whitesides, "Control of soft machines using actuators operated by a braille display," *Lab on a Chip*, vol. 14, no. 1, pp. 189–199, 2014.

[166] J. A. Rhodin, "The ultrastructure of mammalian arterioles and precapillary sphincters," *Journal of ultrastructure research*, vol. 18, no. 1-2, pp. 181–223, 1967.

[167] A. Sadeghi, L. Beccai, and B. Mazzolai, "Innovative soft robots based on electro-rheological fluids," in *Intelligent Robots and Systems (IROS), 2012 IEEE/RSJ International Conference on*, pp. 4237–4242, IEEE, 2012.

[168] A. D. Marchese, C. D. Onal, and D. Rus, "Soft robot actuators using energy-efficient valves controlled by electropermanent magnets," in *Intelligent Robots and Systems (IROS), 2011 IEEE/RSJ International Conference on*, pp. 756–761, IEEE, 2011.

[169] G. Gerboni, T. Ranzani, A. Diodato, G. Ciuti, M. Cianchetti, and A. Menciassi, "Modular soft mechatronic manipulator for minimally invasive surgery: overall architecture and development of a fully integrated soft module," *Meccanica*, vol. 50, no. 11, pp. 2865–2878, 2015.

[170] J. W. Booth, J. C. Case, E. L. White, D. S. Shah, and R. Kramer-Bottiglio, "An addressable pneumatic regulator for distributed control of soft robots," in *2018 IEEE International Conference on Soft Robotics (RoboSoft)*, pp. 25–30, April 2018.

[171] N. Napp, B. Araki, M. T. Tolley, R. Nagpal, and R. J. Wood, "Simple passive valves for addressable pneumatic actuation," in *Robotics and Automation (ICRA), 2014 IEEE International Conference on*, pp. 1440–1445, IEEE, 2014.

[172] P. Rothemund, A. Ainla, L. Belding, D. J. Preston, S. Kurihara, Z. Suo, and G. M. Whitesides, "A soft, bistable valve for autonomous control of soft actuators," *Science Robotics*, vol. 3, no. 16, p. eaar7986, 2018.

[173] B. Mosadegh, C.-H. Kuo, Y.-C. Tung, Y.-s. Torisawa, T. Bersano-Begey, H. Tavana, and S. Takayama, "Integrated elastomeric components for autonomous regulation of sequential and oscillatory flow switching in microfluidic devices," *Nature physics*, vol. 6, no. 6, p. 433, 2010.

[174] A. Zatopa, S. Walker, and Y. Menguc, "Fully soft 3d-printed electroactive fluidic valve for soft hydraulic robots," *Soft robotics*, 2018.

[175] A. Tonazzini, A. Sadeghi, and B. Mazzolai, "Electrorheological valves for flexible fluidic actuators," *Soft Robotics*, vol. 3, no. 1, pp. 34–41, 2016.

[176] A. H. Helal *et al.*, *Designing devices using electro-active yield stress fluids*. PhD thesis, Massachusetts Institute of Technology, 2016.

[177] M. Yalcintas and H. Dai, "Magnetorheological and electrorheological materials in adaptive structures and their performance comparison," *Smart Materials and Structures*, vol. 8, no. 5, p. 560, 1999.

[178] O. Ashour, C. A. Rogers, and W. Kordonsky, "Magnetorheological fluids: materials, characterization, and devices," *Journal of intelligent material systems and structures*, vol. 7, no. 2, pp. 123–130, 1996.

[179] Y. T. Choi, C. M. Hartzell, T. Leps, and N. M. Wereley, "Gripping characteristics of an electromagnetically activated magnetorheological fluid-based gripper," *AIP Advances*, vol. 8, no. 5, p. 056701, 2018.

[180] N. Wiltsie, M. Lanzetta, and K. Iagnemma, "A controllably adhesive climbing robot using magnetorheological fluid," in *Technologies for Practical Robot Applications (TePRA), 2012 IEEE International Conference on*, pp. 91–96, IEEE, 2012.

[181] I. Chopra and J. Sirohi, *Smart Structures Theory*. Cambridge Aerospace Series, Cambridge University Press, 2013.

[182] I. Zuriguel, A. Garcimartín, D. Maza, L. A. Pugnaloni, and J. M. Pastor, "Jamming during the discharge of granular matter from a silo," *Phys. Rev. E*, vol. 71, p. 051303, May 2005.

[183] F. D. Goncalves and J. D. Carlson, "An alternate operation mode for mr fluids-magnetic gradient pinch," *Journal of Physics: Conference Series*, vol. 149, no. 1, p. 012050, 2009.

[184] K. Gilpin, A. Knaian, and D. Rus, "Robot pebbles: One centimeter modules for programmable matter through self-disassembly," in *Robotics and Automation (ICRA), 2010 IEEE International Conference on*, pp. 2485–2492, IEEE, 2010.

[185] A. N. Knaian, *Electropermanent magnetic connectors and actuators: devices and their application in programmable matter*. PhD thesis, Massachusetts Institute of Technology, 2010.

[186] T. Leps, P. Glick, D. Ruffatto III, A. Parness, M. Tolley, and C. Hartzell, "A low-power, jamming, magnetorheological valve using electropermanent magnets suitable for distributed control in soft robots," *Smart Materials and Structures*, vol. 29, no. 10, p. 105025, 2020.